University of Rome

SAPIENZA

Faculty of Science MM.FF.NN.

Ph.D. in Material Science

Cycle XXIV

Local structural studies of Fe-based superconductors

Candidate:

Antonella Iadecola

Supervisor:

Prof. Naurang Lal Saini

Coordinator:

Prof. Ruggero Caminiti

A.A. 2010/11

Antonella Iadecola

Local structural studies of Fe-based superconductors.

PhD. Thesis. Sapienza- University of Rome

All'uomo che ci sarà sempre.

Abstract

In the framework of high temperature superconductors, the Fe-based systems are the first magnetic materials that exhibit a critical temperature above 50 K. These systems are characterized by strong interplay between electronic, spin and lattice degrees of freedom and the macroscopic functional properties arise from the competitions between them. All the theoretically and experimental results point out on the difficulty to separate the effects of disorder, doping and magnetism on the superconducting properties. The presence of multiple bands crossing the Fermi level makes the electronic structure very sensitive to the structural details, particulary to the changes on the local atomic arrangement in the Fe-Pn/Ch slabs. The aim of this work is to study the local structure and discuss possible implications on the electronic properties in the Fe-based superconductors. This has important implications, both in theoretical and in practical terms: a close relationship between structure and superconductivity, direct or indirect, places constraints on both the theoretical understanding of the pairing interaction and the promise of superconductors with higher T_C values. The proposed sensitivity of electronic structure and/or magnetic interactions to the details of the internal structure of the Fe-As layers is likely relevant to unraveling this puzzle. Among the Fe-based superconductors, we have chosen REFeAsO (1111) and FeSe (11)-type materials for this work. From detailed studies using EXAFS and XANES on different atomic edges, we can conclude that the local structure appears different from the crystallographic structure in the Fe-based superconductors. While the presence of spacer layer in the Fe-based superconductors seems important to the properties of the active Fe-As block through atomic order/disorder, the absence of spacer layer introduces inhomogeneities through breaking the local structural symmetry. The results reported in this thesis provide important feedback for the models describing the correlating superconductivity and magnetism in the Fe-based superconducting materials.

Publications

- Iadecola A., Agrestini S., Filippi M., Simonelli L., Fratini M., Joseph B., Mahajan D. and Saini N.L., *EuroPhys. Lett.* 87, 26005 (2009). "Local structure of REFeAsO (RE=La, Pr, Nd, Sm) oxypnictides studied by Fe K-edge EXAFS"

- Joseph B., Iadecola A., Fratini M., Bianconi A., Marcelli A. and Saini N.L., *J. Phys.: Condens. Matter* 21, 432201 (2009). "RE x-ray absorption study of $REO_{1-x}F_xFeAs$ (RE=La, Pr, Nd, Sm) oxypnictides"

- Xu W., Marcelli A., Joseph B., Iadecola A., Chu W. S., Di Gioacchino D., Bianconi A., Wu Z. Y. and Saini N.L., *J. Phys.: Condens. Matter* 22, 125701 (2010). "Local structural disorder in REFeAsO oxypnictides by RE L_3-edge XANES"

- Xu W., Joseph B., Iadecola A., Marcelli A., Chu W.S., Di Gioacchino D., Bianconi A., Wu Z.Y. and Saini N.L., *EuroPhys. Lett.* 90, 57001 (2010). "Arsenic K-edge XANES study of REFeAsO oxypnictides"

- Joseph B., Iadecola A., Schiavo B., Cognigni A., Olivi L. and Saini N.L., *J. Phys. Chem. Sol.* 71, 1069 (2010). "Large atomic disorder in nanostructured $LaNi_5$ alloys: A La L_3-edge extended X-ray absorption fine structure study"

- Joseph B., Iadecola A., Schiavo B., Cognigni A., Olivi L. and. Saini N.L., *J. Sol. St. Chem.* 183, 1550 (2010). "Local structure of ball-milled $LaNi_5$ hydrogen storage material by Ni K-edge EXAFS"

- Saini N.L., Joseph B., Iadecola A., Mizokawa T., Fujimori A., Ito T. and Oka K., *J. Phys.*

Soc. Jpn. 79, 114718 (2010). "Photoemission study of $La_{8-x}Sr_xCu_8O_{20}$: impact of the charge and spin density waves on the electronic structure"

- Joseph B., Iadecola A., Puri A., Simonelli L., Mizuguchi Y., Takano Y., and Saini N.L., *Phys. Rev. B* 82, 020502 (2010). "Evidence of local structural inhomogeneity in $FeSe_{1-x}Te_x$ from extended x-ray absorption fine structure"

- Iadecola A., Joseph B., Simonelli L., Mizuguchi Y., Takano Y. and Saini N.L., *EuroPhys. Lett.* 90, 67008 (2010). "Determination of the local structure in $FeSe_{0.25}Te_{0.75}$ single crystal by polarized EXAFS"

- Joseph B., Iadecola A., Simonelli L., Mizuguchi Y., Takano Y., Mizokawa T. and Saini N.L., *J. Phys.: Condens. Matter* 22, 485702 (2010). "A study of the electronic structure of chalcogenides $FeSe_{1-x}Te_x$ by Fe and Se K-edge x-ray absorption near edge structure measurements"

- Saini N.L., Masikawa Y.,. Joseph B,. Iadecola A,. Dalela S., Srivastava P., Mangano E., Malvestuto M., Mizuguchi Y., Takano Y., Mizokawa T. and Garg K.B., *Phys. Rev. B* 83, 052502 (2011). "Electronic structure of $FeSe_{1-x}Te_x$ studied by Fe $L_{2,3}$-edge X-ray absorption spectroscopy"

- Joseph B., Iadecola A., Malavasi L., and Saini N.L., *J. Phys.: Condens. Matter* 23, 265701 (2011). "Temperature dependent local structure of $NdFeAsO_{1-x}F_x$ system using arsenic K-edge extended x-ray absorption fine structure"

- Iadecola A., Joseph B., Puri A., Simonelli L., Mizuguchi Y., Testemale D., Proux O., Hazemann J.-L., Takano Y. and Saini N.L., *J. Phys.: Condens. Matter* 23, 425701 (2011). "Random alloy-like local structure of $Fe(Se,S)_{1-x}Te_x$ superconductors revealed by extended X-ray absorption fine structure"

Contents

Introduction **iii**

1 An overwiev of Fe-based systems **1**

1.1 Crystallographic Structure 5

1.2 Transport Properties 9

1.3 Magnetic Properties 13

1.4 Electronic Properties 16

2 X-ray absorption spectroscopy **21**

2.1 General aspects of X-ray Absorption 21

2.2 Extended X-Ray Absorption Fine Structure (EXAFS) 25

2.2.1 Effects of thermal vibrations and gaussian disorder 30

2.2.2 Effects of anisotropy 32

2.3 Fluorescence EXAFS 33

2.4 EXAFS data analysis 34

2.5 X-Ray Absorption Near Edge Structure (XANES) 36

2.6 X-ray Synchrotron Radiation 39

3 Local structure of REFeAsO pnictides **41**

3.1 Effect of rare-earth substitution in REFeAsO 44

3.1.1 Fe K-edge EXAFS study 45

3.1.2 RE L_3 – *edge* x-ray absorption study 50

3.1.2.1 *RE L_3-edge x-ray absorption measurements: results and discussion* 51

3.1.2.2 *Multiple scattering calculations: results and discussion* 56

3.1.3 As K-edge EXAFS study . . . 64
3.1.3.1 *Multiple scattering calculations in the XANES region: results and discussion* . . . 65
3.1.3.2 *As K-edge EXAFS measurements: results and discussion* . . . 70
3.1.4 Summary and conclusions . . . 75
3.2 Effect of charge density and temperature in superconducting $NdFeAsO_{1-x}F_x$ . . . 77
3.2.1 As K-edge EXAFS study . . . 78
3.2.2 Nd L_3-XANES study . . . 88
3.2.3 Summary and conclusions . . . 90

4 Local structure of Fe-based 11 type chalcogenide 91
4.1 Effect of Te substitution on the local structure of FeSe system . . . 94
4.1.1 Evidence of local structural inhomogeneity in $FeSe_{1-x}Te_x$ . . . 95
4.1.2 Determination of the local structure in $FeSe_{0.25}Te_{0.75}$ single crystal by polarized EXAFS . . . 100
4.1.3 Random alloy-like local structure of $Fe(Se,S)_{1-x}Te_x$ superconductors revealed by EXAFS . . . 107
4.1.4 Summary and conclusions . . . 115
4.2 Effect of Te substitution on the electronic structure of FeSe system . . . 118
4.2.1 Fe and Se K-edge XANES measurements . . . 119
4.2.2 Fe $L_{2,3}$-edge x-ray absorption spectroscopy study . . . 123
4.2.3 Summary and conclusions . . . 128

Conclusion 129

Appendix 133

Introduction

Historically, the typical antagonistic relationship between superconductivity and magnetism has led researchers to avoid using magnetic elements - ferromagnetic in particular - as potential building blocks of new superconducting materials. Because elemental iron is strongly magnetic, the discovery in 2008 of superconductivity with the transition temperature about 26 K in fluorine-doped oxyarsenide $LaFeAsO_{1-x}F_x$ [1] was completely unexpected. Moreover, the new superconductor belonged to none of the known classes of high-temperature superconductors (HTSCs) such as HTSC cuprates [2], fullerides [3] or MgB_2 [4], this discovery immediately attracted rapt attention. To date, five unique crystallographic structures have been shown to support superconductivity. All these structures possess tetragonal symmetry at room temperature and range from the simplest α-PbO-type binary element structure, to more complicated quinternary structures composed of elements that span the entire periodic table. The key ingredient is a quasi-2D layer consisting of a square lattice of iron atoms with tetrahedrally coordinated bonds to either phosphorus, arsenic, selenium or tellurium anions that are staggered above and below the iron lattice to form a checkerboard pattern that doubles the unit cell size. These slabs are either simply stacked together, as in FeSe, or are separated by spacer layers using alkali (e.g., Li), alkaline earth (e.g., Ba), rare earth oxide/fluoride (e.g., LaO or SrF) or more complicated perovskite-type combinations (e.g., $Sr_3Sc_2O_5$). These so-called "blocking layers" provide a quasi-2D character to the crystal since they form atomic bonds of more ionic character with the FeAs layer, while the FeAs-type layer itself is held together by a combination of covalent (i.e., Fe-As) and metallic (i.e., Fe-Fe) bonding. It is now widely thought that the interaction that leads to the high-T_C superconductivity originates within these common iron layers, similar in nature to the common copper-oxide building block found in the copper-oxide (cuprate) high-T_C superconductors [5]. As in the cuprates, chemical substitution also plays a key role in inducing

the superconducting phase in iron-pnictides. However three key differences are found: (1) in the arrangement of pnictogen/chalcogen anions above and below the planar iron layer as opposed to the planar copper-oxygen structure of the cuprates; (2) in the ability to substitute or dope directly into the active pairing layer; and (3) in the metallic (rather than insulating) nature. These traits, together with the similar interplay of magnetism and superconductivity, mark the iron-pnictides and cuprates as distinct, but closely related, superconducting families [6].

The generic phase diagram of the FeSC systems can be produced by manipulating the chemical or structural properties, using either chemical doping/substitution or applied external pressure to drive an antiferromagnetic (AFM), non-superconducting parent compound to a superconducting (SC), non-AFM state. The nature of magnetism in the FeSC parent compounds is a hotly debated topic, largely due to its implications for the pairing mechanism: the electronic structure suggests that the same magnetic interactions that drive the AFM ordering also produce the pairing interaction for superconductivity [7]. Regardless of the exact nature of magnetic order, it is clear that magnetostructural coupling is prevalent throughout the FeSC family. A structural phase transition (T_S) - from tetragonal at high temperatures to orthorhombic at low temperatures - is almost always coupled to the magnetic transition at T_N. Theoretically, this magnetostructural coupling is understood to be a consequence of the magnetic interactions [8], and not coupled with the structural transition.

The electronic structure is well known as consisting of two-dimensional (2D) metallic sheets derived from Fe d-states hybridized with Pn/Ch p-orbital derived bands, sitting in a quasi-ionic framework composed of rare earth, oxygen, alkali or alkaline earth "blocking layers". This arrangement produces a metallic material with nominal Fe valence of 2^+, low carrier concentration and high electronic density of states dominated by Fe d-states [9]. The electronic band structure has been calculated using the local density approximation [10], showing that the electronic properties are dominated by five Fe d-states at the Fermi energy.

The connection between structural details of FeSC materials and their seemingly sensitive electronics is an important aspect of superconductivity in the FeSCs. An empirical relation between the tetrahedral bond angle of the As-Fe-As layer and T_C values for different FeSCs was recognized early on, with optimal T_C values suggested to be dependent upon ideal tetrahedral geometry [11]. This has important implications, both theoretically and in practical terms: a close relationship between structure and superconductivity, direct or indirect, places constraints on both the

theoretical understanding of the pairing interaction and the promise of superconductors with higher T_C values. A proposed sensitivity of electronic structure and/or magnetic interactions to details of the internal structure of the Fe-As layers is likely relevant to unraveling this puzzle.

The manner in which electrons behave in a solid is well captured by one of the staples of condensed-matter physics known as band theory. A metal's band structure can convey a simple yet quantitative description of its electronic, optical and structural properties, and is the basis for understanding many exotic phenomena, such as in newly discovered FeSC. The band structures of the iron-based superconducting materials have been calculated using theoretical calculation (local density approximation, first-principle density functional theory), finding good general agreement with experimental measurements. The dominant contribution to the electronic density of states at E_F derives from metallic bonding of the iron d-electron orbitals in the iron pnictogen (or chalcogen) layer. These form several bands that cross E_F, both electron- and hole-like, resulting in a multiband system dominated by iron d character. It is well know that the multiband systems are characterized by a strong interplay between lattice, electronic and magnetic degrees of freedom. Therefore, the knowledge of the average structure is not sufficient to explore the possible correlation between the structure and functional properties of these systems. For this purpose, it is necessary to know the structure at the atomic level, i.e. on the local scale, as it has been already shown previously for the cuprates [12].

The aim of this work is to study the local structure and discuss possible implications on the electronic properties in the Fe-based superconductors, with varying both chemical pressure and temperature. Among the Fe-based superconductors, we have chosen REFeAsO (1111) and FeSe (11)- type materials for this work.

Previous experiments indicated that by fluorine doping at the oxygen site, superconductivity could be realized in the REFeAsO compounds by suppressing the spin-density wave order and further enhanced by the chemical pressure shrinking the crystalline lattice [13]. However the mechanism that correlates the superconducting properties with the crystalline structure is still unclear. The local structural studies of REFeAsO system, as a function of rare-earth size, fluorine doping and temperature are fundamental to provide a feedback between theoretical model and experimental results. Common factors are found in FeAs-based pnictides and FeSe-chalcogenides. In particular, fundamental electronic and magnetic properties in chalcogenides are found to show extreme sensitivity to the atomic positions [14] as in the pnictides. Therefore,

the 11 Fe-chalcogenide system provides a unique opportunity to study the interplay of the structure, magnetism, and superconductivity in the Fe-based families because of the relative chemical simplicity with added advantage of the absence of any spacer layers that may affect the electronic and structural properties within the active Fe-Fe layers. It is clear that the interplay between different degrees of freedom plays a key role in determining the physical properties in these Fe-based systems. Thus it is of great importance to understand how the functional properties are influenced by the temperature and Te substitution.

This thesis is organized in four chapters.

In the first chapter, we provide an overview on the structural and functional properties of the Fe-based superconductors. All the Fe-based systems contain square lattice layers of Fe atoms, where each Fe atom is tetrahedrally coordinated with four Pn/Ch atoms. While this common factor, the transport properties and the magnetic properties exhibit some crucial differences, that are reflected also in superconducting state. We include only the most important experimental and theoretical results that have helped to understand the phenomenology of the Fe-based superconductors.

In the second chapter, we introduce the experimental tecnique that we have used for the local structural studies, the X-ray absorption spectroscopy. X-ray absorption fine structure (XAFS) is a fast ($\sim 10^{-15}s$) and a site selective method, providing information on the local atomic distribution and geometry around a selected absorbing atom, through photoelectron scattering. The Extended X-ray absorption fine structure (EXAFS) allows to determine the distances between the absorbing atom and the nearest-neighbours and the related mean square relative displacements (correlated fluctuations of the bond pair). X-ray absorption near edge structure (XANES) spectroscopy is a specific probe of the distribution of valence electrons and local chemistry, with the final states in the continuum being due to multiple scattering resonances of the photoelectron in a finite cluster. Theoretical principles, experimental details and data analysis method are also explained in this chapter [15].

In the third chapter, we present the results of the local structural studies obtained on the 1111 oxypnictide materials, as a function of rare-earth size, fluorine doping and temperature. Local structure of REFeAsO system has been studied as a function of chemical pressure due to different rare-earth size. Because the FeAs is the active layer, first we have considered the local atomic distribution around the Fe atom. We have found that the Fe-As bond is a

strongly covalent bond, while the Fe-Fe and Fe-Re bond lengths display a systematic changes with the chemical pressure [16]. In addition, the As height on the Fe-Fe plane increases with decreasing rare-earth size, and consequently also the Fe-As-Fe angle decreases, revealing perfect $FeAs_4$ tetrahedron [11, 17] for the SmFeAsO. Since the vertical position of the As atom changes systematically with the rare earth size, this has a direct influence on the local geometry of the REO slabs [18, 19, 20]. In particular, the vertical position of the As atom induces an oxygen disordering in the REO slabs , that is more significant in the SmFeAsO than in the LaFeAsO [21]. Moreover, we have carried out a systematic temperature dependent local structural studies of the $NdFeAsO_{1-x}F_x$ high temperature pnictide superconductor, as a function of fluorine doping. No anomalous changes in the Fe-As bond have been observed as a function of temperature and fluorine content. However, the Einstein frequency for the superconducting sample is higher than that of the parent compound, indicating a hardening of the Fe-As bond in the former compared to the latter. The overall temperature dependence of the MSRDs of the Fe-As bond show a systematic variation of the corresponding force constants [22].

In the fourth chapter, we present the local structural studies on the 11 chalcogenide compounds, as a function of chalcogen substitution and temperature. We have investigate the local structure of $Fe(Se,S)_{1-x}Te_x$ systems, to quantify the local interatomic distances and their mean-square relative displacements as a function of temperature. We find that Fe-(Se,S) and Fe-Te distances in the ternary $Fe(Se,S)_{1-x}Te_x$ are closer to the respective distances in the binary systems, revealing significant divergence of the local structure from the average one. The Se/S and Te atoms do not occupy the same atomic site in the $Fe(Se,S)_{1-x}Te_x$, breaking the average crystal symmetry [23, 24]. The mean square relative displacements (MSRDs) show a systematic change with Te contents, consistent with bond relaxation in the inhomogeneous ternary phases [25]. In order to provide valuable information on the electronic structure of $FeSe_{1-x}Te_x$ compounds, we have combined the experimental XAS spectra, that reproduce the unoccupied electronic states near the Fermi level, with an appropriate theoretical description [26]. We have found that the hybridization of Fe *3d* and chalcogen *p* states decreases with increasing Te concentration, causing the strong chalcogen height sensitivity of the fundamental properties of the Fe-based chalcogenides. In addition, the chalcogen *p* state, involved in admixing with the unoccupied Fe *3d* states near the Fermi level, have a predominant $p_{x,y}$ character [27].

Finally, we discuss the implications of the obtained results in the field of the Fe-based super-

conductivity.

Chapter 1

An overwiev of Fe-based systems

The report of superconductivity at 26 K in LaFeAsO doped with F on the oxygen site in 2008 [1] was not the first discovery of an iron-containing superconductor, nor even the first reported superconducting iron pnictide (LaFePO, $T_C \approx 5K$, [28]). Although iron has been considered deleterious to superconductivity due to its strong local magnetic moment, a number of superconducting compounds containing iron in which the iron is non-magnetic have long been known. In fact, Fe itself under pressure is a superconductor, with $T_C \approx 1.8K$ at 20 GPa [29].

However, the discovery of Kamihara et al. is ground breaking for a number of reasons [30]. One is that – just like the discovery of superconductivity at 35 K in Ba-doped La_2CuO_4 [2] – it led to the almost immediate further discovery of even higher T_C materials, with the current record $\sim 56K$ observed in $Gd_{0.8}Th_{.02}FeAsO$ [31], $Sr_{0.5}Sm_{0.5}FeAsF$ [32] and in $Ca_{0.4}Nd_{0.6}FeAsF$ [33]. The path to this higher transition temperature was also similar to that in the high T_C cuprates, where pressure experiments [34] first increased the T_C in Ba-doped La_2CuO_4 from 35 to 53 K. This was followed by chemical pressure experiments where T_C was raised to 93 K [35] by replacing La with the smaller Y to make a multi-phase sample containing $YBa_2Cu_3O_{7-\delta}$. In the case of F-doped LaFeAsO, Takahashi et al. [36] found that 4 GPa pressure increased the T_C from 26 K 6 to 43 K. This result then inspired researchers to use chemical pressure (replacing the La with the smaller rare earths Gd, Sm, Nd, Pr, Ce), first reaching $T_C = 43K$ in $SmFeAsO_{0.85}F_{0.15}$ [37] and then less than a month later $T_C = 55K$ in the oxygen deficient $SmFeAsO_{0.85}$ prepared by high pressure synthesis [38].

A second reason why the work of Kamihara et al. is so seminal is that it has led to a new class of high temperature superconductors, the so-called iron pnictides ('FePn', where Pn is As or P), which have already been extended to include iron chalcogenides ('FeCh', where Ch includes S, Se and Te). The list of these compounds has expanded rapidly from the original LaFeAsO '1111' structure (of which there are over 150 Rare Earth/Transition Metal/Pnictide/O examples) first explored by Kamihara et al. and successors for superconductivity. The next iron-containing superconductor structure includes members of the MFe_2As_2 ('122') family, where Rotter and coworkers discovered $T_C = 38K$ in K-doped $BaFe_2As_2$, $Ba_{0.6}K_{0.4}Fe_2As_2$[39]. The MFeAs ('111') family ($T_C = 18K$ [40]), the iron chalcogenide FeSe ('11') family ($T_C = 8K$ [41]), the Sr_2MO_3FePn, M=Sc,V,Cr ('21311') family (M=Sc and Pn=P, $T_C = 17K$ [42]; M=V and Pn=As, $T_C = 37K$ [43]) and the defect structure $A_{0.8}Fe_{1.6}Se_2$ ($T_C \approx 32K$, A=K, Rb, Cs, Tl) related to the 122 structure and called '122*' herein round out the established list. The last four families all exhibit superconductivity without doping an additional atom type and as yet have only a few members known, although this is changing. As will be discussed, it is not just the 1111 structure whose initial T_C has been greatly enhanced by further work. For example, T_C of FeSe under 7 GPa pressure increases more than fourfold to 37 K [44] and with Te doping ($FeSe_{1-x}Te_x$) increases almost twofold to $\sim 15K$ [45].

A third, and perhaps the most interesting, aspect of these new iron-containing superconductors from a basic physics point of view is that the superconducting pairing mechanism may be related to the coexistent magnetism in the phase diagram [46]. Current thinking is that the pairing is not primarily phonon mediated, although due to the coupling of the magnitude of the Fe moments to the Fe-Pn/Ch bond length and the presence of an isotope effect, the magnetoelastic coupling is thought to be important for superconductivity [47]. Theoretical alternatives to phonon coupling include various electronic excitations that could mediate the superconducting pairing, e. g. spin fluctuations (as is suggested by inelastic neutron scattering data) or inter-orbital pair hopping. If this is indeed the case, such a pairing mechanism may promise even higher temperature superconductivity since the transition temperature, T_C, would be proportional to a characteristic energy scale potentially significantly larger than the BCS scale dependence on the average phonon frequency, $T_C^{BCS} \propto < \omega >$.

Fourth the properties of the FePn/Ch superconductors are fundamentally different both from those of a conventional electron-phonon coupled superconductor and also from those of the

cuprates. In a clean conventional superconductor, the electronic excitations are exponentially suppressed in the superconducting state by the gap, while in unconventional superconductors like the FePn/Ch there are many examples of compounds with nodal (gap zero) points or lines leading to finite electronic excitations remaining as $T \rightarrow 0$. Although the pairing symmetry in the superconducting state is still under debate, it is apparently not conventional s-wave in many of the FePn/Ch since neutron scattering measurements [48] provide convincing evidence for a sign change in the superconducting energy gap Δ on different parts of the Fermi surface in a number of compounds. In certain samples, neutron scattering data imply a direct coupling between the superconductivity and the magnetism, as seen in, for example, the unconventional heavy Fermion superconductor UPt_3. As a more interesting comparison with conventional - e. g. elemental or A-15 - superconductors, the discontinuity in the specific heat at T_C, ΔC, scales differently in the FePn/Ch superconductors: $\Delta C \propto T_C^3$ vs T_C^2 for conventional superconductors. In comparing to the cuprates, it seems clear that – although the FePn/Ch are unconventional superconductors - they are different in many respects from the cuprates. The cuprates have strong electron correlations, while the FePn/Ch show in general relatively weak correlations [49, 50, 51]. Moreover, the cuprates are much more anisotropic and have d-wave gap symmetry vs primarily s-wave for the FePn/Ch. The cuprates have a much different Fermiology that remains relatively constant (at least for hole-doping) with doping vs the Fermiology in the FePn/Ch. The cuprates exhibit a rapid decrease in T_C upon doping in the CuO planes vs the relative insensitivity of the FePn/Ch layer superconductivity to doping. Thus, doping and its effect on T_C, T_S and T_{SDW} is an important tool for understanding the pairing mechanism in the FePn/Ch. A comparison between the cuprates and the FePn/Ch that is highlighted by the recent discovery of superconductivity in the defect-driven 122* structure $A_{0.8}Fe_{1.6}Se_2$ compounds is that, with the exception of the 122*'s, the FePn/Ch do not appear to have an insulating phase anywhere nearby in the phase diagram to the superconducting compositions, while the cuprates do. Lastly, it is well to remember that the FePn/Ch superconductors mechanically are metals, without the brittleness of the ceramic cuprates, making applications more tractable.

The new iron superconductors have a number of properties in common. These common properties presumably hold the clue to understanding the relatively high temperature of the superconductivity. It is naturally hoped that achieving this understanding will help lead to discovery of even higher T_C's. A representative list of these common properties (together with

the exceptions) would include:

1. All six families of iron-containing superconductors have 2D planes of FePn/Ch tetrahedra, and the angle of the bonds in the tetrahedra as well as the height of the Pn/Ch above the Fe are indicators of T_C.

2. The Fe $3d$ electrons are – in contrast to the earlier superconductors containing Fe – at the Fermi energy, and clearly taking part in the superconductivity.

3. In most FePh/Ch, the Fe $3d$ electrons are magnetic in some part of the phase diagram either close to or even coexistent with superconductivity. It is arguably the case that the 11 superconducting properties of this new class of superconductor are fundamentally influenced by the Fe and its magnetic fluctuations.

4. Both hole and electron doping of the non-superconducting 1111 and 122 parent compounds cause superconductivity, with electron-doping causing in general the higher T_C's in the 1111's while hole-doping causes higher T_C's in the 122's.

5. For the undoped 1111 and the 122 compounds, there are both a spin density wave transition and a structural phase transition (tetragonal to orthorhombic upon cooling). The superconducting FeSe displays a structural transition (tetragonal – orthorhombic) at 90 K [53] but no magnetic transition. $Fe_{1+y}Se_xTe_{1-x}$, which is superconducting for $x \geq 0.05$, has both a structural – tetragonal to monoclinic - and a coincident magnetic transition (at 72 K for x=0)[54]. In the 122* there is a defect ordering temperature which changes the structure from one tetragonal symmetry to another a few tens of Kelvin above the antiferromagnetic transition which, unlike the other FePn/Ch structures, has the moment along the c-axis.

6. The two transitions are at different temperatures in the undoped 1111's but coincide in temperature in the undoped 122's. T_S/T_{SDW} values for the MFe_2As_2 are similar to those in the 1111's and range from 140 to 205 K. This coincidence of the structural and magnetic transitions in the 122's disappears with doping on the Fe and As sites, although the case of isoelectronic Ru doping of the Fe in $BaFe_2As_2$ is under debate .

7. Inelastic neutron scattering (INS) has found (similar to results in the cuprates) a spin fluctuation resonance in the 1111, 122, and 11 structure superconductors below T_C. These

experiments may provide evidence (that is still undergoing refinement) for a causal link between the spin fluctuations (which are directionally in the Fermi surface pocket nesting direction) and the pairing that opens the superconducting gap.

8. Measurements of angular resolved photoemission spectroscopy (ARPES) on the FePn/Ch finds a Fermiology consisting typically of five separate pockets, with varying degrees of interpocket nesting ranging from very strong in the undoped 122 parent compounds to totally absent in overdoped (but still superconducting) $BaFe_{2-x}Co_xAs_2$ and LiFeAs. The importance of the five Fe $3d$ bands at the Fermi energy in these materials is well established, with good agreement between measurements and calculations.

These common factors (with the exception of the five-fold Fermiology) have their analogs in the well-studied high T_C cuprates. All the cuprate derivative structures have Cu-O planes in common, the Cu electrons are involved in the superconductivity, there is magnetism in the undoped, non-superconducting compound phase diagrams, both hole and electron doping cause superconductivity with hole doping being more effective in raising T_C, and pressure is known, as already mentioned, to have a large effect on T_C. There are however important differences between the new iron superconductors and the cuprates, as have already been discussed as one of the main points of interest for studying the FePn/Ch. In the final analysis, although analogy with the huge body of knowledge collected on the cuprates can be of help in choosing which investigations might yield essential insights, the FePn/Ch appear to be – in much of their fundamental behavior – categorically different from the cuprates.

1.1 Crystallographic Structure

As discussed in the introduction, all of the iron pnictide and chalcogenide superconductors have structural and physical properties in common. The present section focuses on the connection between the structural and magnetic phase transition with the superconductivity. First, the structure of these materials is presented. The structure is crucial in any attempt to understand the superconductivity, particularly since there are aspects of the structure in the FePn/Ch which influence T_C where similarities and correlations have been found.

All of the FeAs-based high T_C superconductors contain square lattice layers of Fe atoms where each Fe atom is at the center of a (usually) distorted As tetrahedron to form an equiatomic

FeAs layer. These FeAs layers are separated by spacer/charge donation layers along the c-axis such as Ba layers in body-centered-tetragonal $BaFe_2As_2$ or LaO layers in primitive tetragonal LaFeAsO. The same structures are sometimes formed when P replaces As, and/or when Co, Ni or other transition metals partially and/or completely replace the Fe. As seen in the Fig. 1.1.1 [55], the 11-type $FeSe_{1-x}Te_x$ system has no charge reservoir layer. The high T_Cs in the Fe-based materials are observed for compounds that must be doped or put under pressure to reduce or eliminate the combined structural and magnetic transitions. In all these systems of parent compounds, the high temperature structures are tetragonal and the low-temperature structures are distorted variants.

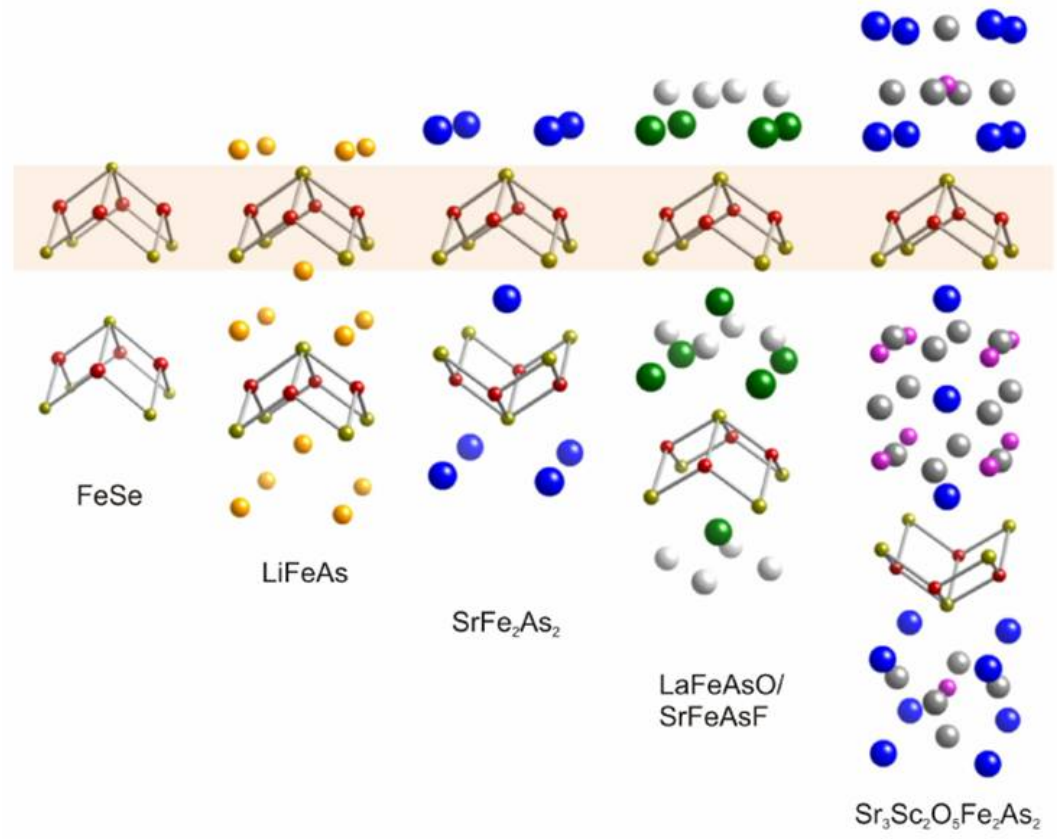

Fig. 1.1.1 *The five tetragonal structures known to support superconductivity. From left to right : FeSe, LiFeAs, $SrFe_2As_2$, LaFeAsO and $Sr_3Sc_2O_5Fe_2As_2$ [6]. Each of these structures contains a square lattice of Fe atoms at high temperatures that can distort at low temperatures.*

The quaternary equiatomic REFeAsO compounds have a rather simple structure of alternating Fe-As and RE-O layers with eight atoms in a tetragonal unit cell (space group: P_4/nmm),

where the Fe-As layer is thought to be responsible for SC, while the RE-O (or F-doped) layer provides charge carriers. The intra-layer and inter-layer chemical bonding is of covalent and ionic character, respectively [38]. For the undoped REFeAsO [56] a structural phase transition (from higher temperature tetragonal to lower temperature orthorhombic phase) occurs, accomplied by a spin density wave (SDW), as confirmed at low temperatures by neutron diffraction studies.

The temperature dependent structure of the AFe_2As_2 parent compounds has been carefully studied for $BaFe_2As_2$ [57], $SrFe_2As_2$ [58], $CaFe_2As_2$ [59] and $EuFe_2As_2$ [60]. In all cases the room temperature tetragonal space group is I_4/mmm and the materials transform to a low temperature orthorhombic $Fmmm$ space group with a 45° rotated cell in the a–b plane. The room temperature I_4/mmm space group is different than the P_4/mmm space group of the 1111 materials in that it contains two FeAs layers per unit cell. In contrast to the 1111 materials, the 122 parent compounds exhibit a structural and magnetic transition at the same temperature.

The structural properties of the 11 family of compounds is complicated by extreme sensitivity to stoichiometry and the presence of excess Fe. Structurally, $Fe_{1+y}Te$ exhibits the PbO crystal structure with a space group of P_4/mmm at room temperature for values of y ranging from 0.068 to 0.14 [61, 62]. At low temperatures, a first-order structural transition is observed (transition temperature $\sim 65K$ [63]) and the low temperature space group is the monoclinic $P2_1/m$ for samples of $Fe_{1.076}Te$ [61]. On the other hand, a small change in x to $Fe_{1.141}Te$ changes the low temperature unit cell to orthorhombic with the $Pmmn$ space group [61] again providing evidence for sensitivity to stoichiometry.

Studies of structure-property relationships of the Fe pnictide-based superconductors have suggested correlations with the superconducting transition temperature T_C. Early on, Zhao and coworkers [17] reported a correlation for a wide range of parent compounds REFeAsO, that the highest T_C occurred for the doped materials in which the respective $FePn_4$ tetrahedra were least distorted (Pn = P, As). More recently, from measurements of the structure versus applied pressure for $BaFe_2As_2$, Kimber et al. concluded that the structure is more important than doping in inducing superconductivity in this compound [64]. Another correlation was found by Mikuda and coworkers among $REFeAsO_{1-\delta}$ compounds, where the T_C was found to increase monotonically with increasing ^{75}As nuclear quadupole resonance frequency ^{75}Q, which in turn reflects the local coordination and bonding of the As atoms [65, 66]. However, a unique corre-

lation between T_C and bond angle is not present. On the other hand, the envelope containing all the data in the Fig. 1.1.2 has an obvious peak near the angle of 109.47° corresponding to an undistorted pnictogen tetrahedron centered by the transition metal M. This suggests that the potential for high T_C is greatest for undistorted MPn_4 tetrahedra, although in that view other factors are clearly also affecting T_C.

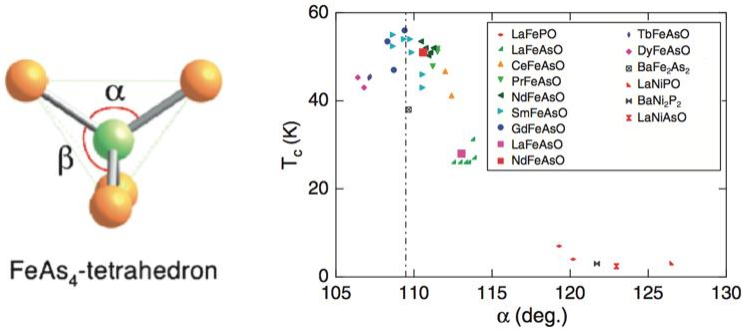

Fig. 1.1.2 *Tc vs As-Fe-As bond angle for various pnictide superconductors. Formulas of parent compositions of superconductors are depicted in the inset. Crystal structure parameters of samples showing almost maximum T_C in each system are selected. The vertical dashed line indicates the bond angle of a regular tetrahedron ($\alpha = 109.47°$)[11]*

Horigane et al. [67] have shown that $FeSe_{1-x}Te_x$ also follow the overall behavior in Fig. 1.1.2, where the T_C is between 6 and 14 K and the bond angle is between 96° and 104.89°. However, it is not obvious that the non-FeAs-based compounds plotted have the same mechanism for T_C as the FeAs-based ones, and thus it is not clear that they should be considered together with the FeAs-based materials with respect to the structure-T_C relationship. When viewed in this light, the only correlation remaining from the plot is that all of the FeAs-based compounds have about the same bond angle, irrespective of T_C, which may simply be a reflection of the specific chemistry of the FeAs-based materials.

Several authors have suggested a related alternative correlation between the T_C and the distance (height h) mentioned above between the Fe layer and either adjacent pnictogen layer for a specific selected subset of Fe-based layered superconductors (Fig. 1.1.3)[68, 69]. The anion height depends on the type of the superconducting Fe-anion layers and it increases in order of FeP, FeAs, FeSe and FeTe. The FeP-based superconductors have low anion heights and show the

lower T_C compared to the FeAs-based superconductors [38, 70]. Focused on the 1111 system, the T_C considerably increases from 7 to 26 K by the replacement of As for P with elevating anion height [70]. For the LaFeAsO system, the T_C dramatically increases up to 55 K when the anion height increases and approaches 1.38Å with the La-site substitution by Nd or Sm, which has a smaller ionic radius than that of La. Also the data point of $FeSe_{0.57}Te_{0.43}$, which is almost optimally doped $FeSe_{1-x}Te_x$, obeyed the curve [44]. Therefore, the unique curve is commonly applicable to 1111-, 122-, 111- and 11-type superconductors.

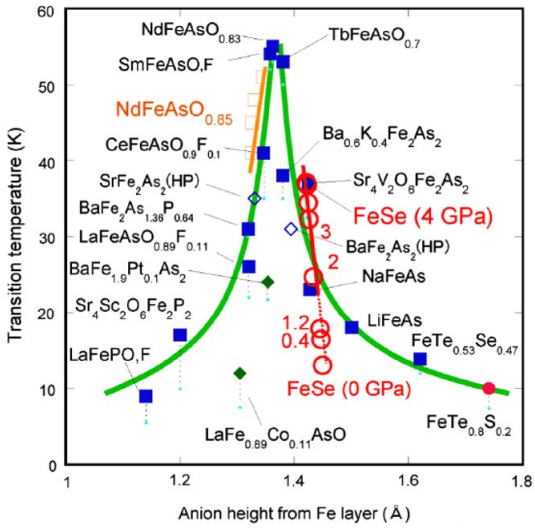

Fig. 1.1.3 *Anion height dependence of T_C for the typical Fe-based superconductors. Large symbols indicate the onset temperature. The zero-resistivity temperatures at ambient pressure are indicated by small light-blue circle. Filled diamonds indicate the data at ambient pressure. Open diamonds are the data of $SrFe_2As_2$ and $BaFe_2As_2$ under the optimal pressure. Open squares indicate the data of $NdFeAsO_{0.85}$ under high pressure (HP). The data of FeSe under HP are indicated by open circles. A filled circle indicates the data of $FeTe_{0.8}S_{0.2}$. Filled green diamonds are the data points for Pt-doped $BaFe_2As_2$ and Co-doped LaFeAsO [68].*

1.2 Transport Properties

The present section focuses on the normal state from which the superconducting state forms, with the magnetic and structural transitions. Measurement of the resistivity and susceptibility,

and to a lesser extent the specific heat, is often used to indicate, via anomalies in these parameters, the progression with doping of the structural and magnetic anomalies. Such measurements allow a more rapid estimate of the part of the phase diagram of particular interest in a given study, which can then be further examined with more microscopic measurement techniques (e. g. x-ray diffraction, neutron diffraction, μSR, Mössbauer). In addition, the residual resistivity ratio (RRR), defined as $\rho(300K)/\rho_0(\rho_0 \equiv \rho(T \to 0))$, where the extrapolation to T=0 is from the normal state above T_C if the sample is superconducting, serves as an important indicator of sample quality since scattering from impurities increases the residual resistivity ρ_0. Another use for these normal state measurements is that their temperature dependence can provide insights useful for understanding the superconductivity. For example, the temperature dependence of the resistivity in the normal state has been used in the study of the FePn/Ch superconductors to determine nearness to quantum criticality in so far as ρ does not follow Fermi liquid behavior. Landau Fermi liquid behavior is $\rho = \rho_0 + AT^2$, with 'A' a constant. Quantum critical behavior can occur [71, 72] at (or near) the point in a phase diagram where a second order phase transition, e. g. antiferromagnetism, has been suppressed to T=0. In the case of the FePn/Ch, T_{SDW} being suppressed to T=0 by doping is an obvious pathway to such quantum critical behavior, with the associated non-Fermi liquid behavior at finite temperatures – including long range magnetic fluctuations potentially important for understanding superconductivity.

The absolute values of resistivity at room temperature for the FePh/Ch are high, $\rho \sim 1m\Omega/cm$ ($\geq 50m\Omega/cm$ for the 122*), where for a good metal (e. g. Cu or Ag) $\rho \sim 1\mu\Omega/cm$. A band structure calculation [10] for FeSe results in small Fermi surface sections, resulting in a semi-metallic classification, although in general the FePn/Ch are called metallic. The x-ray measurements of Yang et al. [73] indicate that the 1111 and 122 FePn/Ch are actually similar to Fe metal, with relatively (compared to the bandwidth) small Coulomb correlation U, an even smaller Hund's coupling (diminishing the tendency to form large local moments), Fe *3d* hybridized bands, and metallic behavior. In general for the FePh/Ch materials, the small carrier density (which gives the high values of ρ), does not imply a small density of states, N(0) (in units of states/eV-atom), at the Fermi energy, which in fact turns out to be relatively high compared to, e. g., the cuprates and this affects the scaling of $\Delta C/T_C$. The magnetic susceptibility, χ, shows a large anomaly at T_{SDW} in the FePn/Ch structures where this transition exists (the 1111's, the 122's, the 122*'s and some of the 11's). Perhaps more importantly, χ data when

taken above T_{SDW} give an idea about the magnetic fluctuations.

In the undoped LaFeAsO [1] the resistivity is approximately temperature independent at $5m\Omega/cm$, with an anomaly at 150 K and an upturn below 100 K. Upon fluorine doping, the upturn in ρ below 100 K decreases and by x=0.11 resistivity falls uniformly from room temperature (metallic behavior) with an RRR of 5. Moreover, the susceptibility of LaFeAsO is about 0.4 memu/mole and roughly temperature independent below room temperature except for the 150 K anomaly and an upturn below $25K$. McGuire et al. [74], with an expanded set of data for χ of LaFeAsO, show that χ increases with increasing temperature above the anomaly up to room temperature by about 30%.

Measurements on polycrystalline $BaFe_2As_2$ [75] gave essentially constant ρ vs T from room temperature down to the T_S/T_{SDW} transition, followed by a monotonic fall off of ρ to lower temperatures with an RRR 5, while $Ba_{0.6}K_{0.4}Fe_2As_2$ is metallic in behavior ($d\rho/dT>0$) down to T_C, with RRR 17. With single crystals, the anisotropy ρ_c/ρ_{ab} at 300 K in the MFe_2As_2 for M=Ba, Sr, Ca, and Eu has been determined to be 150 [77], 80 [78], 50 [79], and 7 [80] respectively.

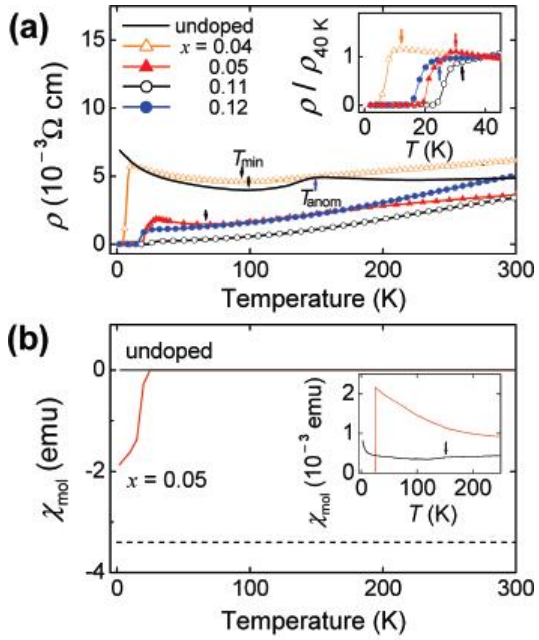

Fig. 1.2.1 *(a) Electrical resistivity (ρ) versus temperature (T) for undoped and $LaO_{1-x}F_xFeAs$ x=0.04, 0.05, 0.11, and 0.12. Inset shows expanded (ρ-T) curves for x=0.04, 0.05, 0.11, and 0.12. Arrows show onset transition temperatures. (b) Molar susceptibility (χ_{mol}) versus T for*

undoped and $LaO_{0.95}F_{0.05}FeAs$. The dotted line denotes perfect diamagnetism for the sample. Inset shows expanded (χ_{mol}-T) curves at 10^3 times magnification of the vertical axis. [36]

The Fig. 1.2.2 shows ρ up to room temperature of polycrystalline samples of $FeSe_{1-x}Te_x$ [81]. With the later advent of single crystals of FeSe the absolute value of ρ decreased by approximately a factor of two [82], but the temperature dependence (metallic, with rounding towards room temperature) remains qualitatively the same. An expanded view of ρ vs T in FeSe showed a linear temperature dependence (i. e. non-Fermi liquid behavior) from $T_C \sim 8K$ up to almost 50 K [83]. Unlike the $\chi \sim T$ behavior reported above T_{SDW} for the 1111's, χ for single crystal FeSe – which has no magnetic transition - increases faster than linearly with temperature by a factor of three above T_C up to $\sim 180K$, at which point c falls by about 20% by room temperature [82]. The magnetic susceptibility in $FeTe_{0.92}$ above $T_{SDW} \sim 70K$ decreases linearly with increasing temperature up to about 240 K [84]. Upon S-doping [85], this $\chi \sim -T$ behavior persists above the depressed T_{SDW} ($\sim 30K$ for $Fe_{1+y}Te_{0.9}S_{0.1}$) up to room temperature. In $FeSe_{0.5}Te_{0.5}$, $T_C \sim 14K$, χ increases linearly with temperature by about 15% between 100 and 250 K (highest temperature of measurement) [86].

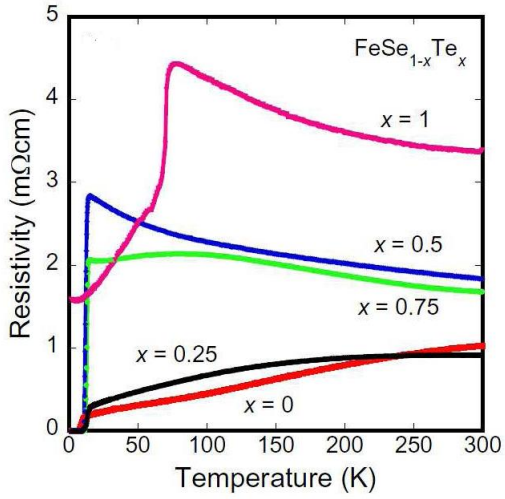

Fig. 1.2.2 *Resistivity vs temperature of polycrystalline $FeSe_{1-x}Te_x$ [81]. Note the anomaly at 72 K in pure FeTe (upper curve) at T_S/T_{SDW}.*

1.3 Magnetic Properties

The parent compounds of both the 1111 and 122 materials are metals which exhibit SDW order. The high temperature ($T > T_N$) paramagnetic state is characterized by magnetic susceptibility with an unusual linear temperature dependence ($\chi \propto T$) [87, 88]. In the following section, we will provide an overview of the magnetic order which evolves out of this unusual paramagnetic state in the 1111, 122, and 11 family of materials. Examination of the magnetic ordering can shed light on the magnetic interactions and the nature (local moment or itinerant) of the magnetism in these materials.

As discussed above, it is well established that the undoped parent of 1111 compounds exhibit some form of antiferromagnetic long range order. This was first observed in LaFeAsO where the magnetic structure was characterized by the ordering wavevector $(\frac{1}{2}\frac{1}{2}\frac{1}{2})_T = (10\frac{1}{2})_O$ (where the subscripts T and O refer to the tetragonal and orthorhombic structures, respectively) and the low temperature ordered magnetic moment was 0.63(1) μB [89]. The magnetic ordering is consistent with stripe-like antiferromagnetic order with ferromagnetically coupled chains along the tetragonal (110) direction coupled antiferromagnetically along the inplane perpendicular direction (see Fig. 1.3.1a). The doubling of the unit cell along the c-axis indicates antiferromagnetic interactions between neighboring planes. The magnetic moment direction could not be uniquely determined in this measurement but the observed intensity is consistent with moments lying in the a–b plane.

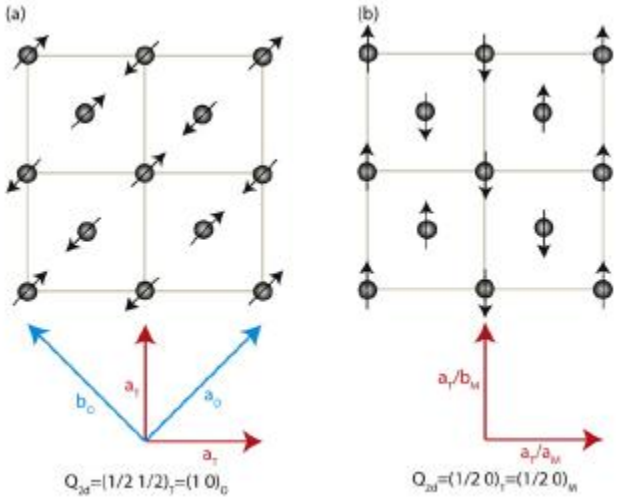

Fig. 1.3.1 *(a) In-plane magnetic structure for the 1111 and 122 parent compounds. For the*

1111 materials, the stacking of neighboring plane along the c-axis is either ferromagnetic or antiferromagnetic depending on the rare earth element. For the 122 materials, the stacking is antiferromagnetic along the c-axis resulting in odd-integer L as the unit cell contains two FeAs layers. (b) Magnetic structure for 11 materials ($Fe_{1+x}Te$) in the limit of smaller x where the low temperature nuclear structure is monoclinic. The ordering wavevector is the same in both the high and low temperature phases [8].

The magnetic moment observed is much smaller than the 2.2 μB moment observed in metallic Fe. The nature of the ordered state in these materials has been a topic of considerable study. The calculated Fermi surface for LaFeAsO consists of electron cylinders near the M point and hole cylinders and a 3D hole pocket around the point Γ [9]. Further investigations indicated good nesting of these components separated by the 2D wavevector $(\frac{1}{2}\frac{1}{2})_T$ consistent with the observed magnetic structure [90, 91]. This led to the suggestion that the observed antiferromagnetic state is a SDW induced by Fermi surface nesting [92, 93]. Futhermore, it has been proposed that near-neighbor and nextnear-neighbor interactions between local Fe moments are both antiferromagnetic and of comparable strength leading to magnetic frustration [93, 94]. In addition to describing the observed magnetic structure, this scenario can also provide an explanation for the structural phase transition as the lattice distortion relieves the magnetic frustration [93, 94], that can explained small ordered moment [93, 95]. Finally, it was recently proposed that both the magnetic and structural transitions are driven by orbital physics and that the structural transition is, in fact, a ferro-orbital ordering transition [96]. This model explains the coupling of the structural and magnetic transitions and is consistent with the rather large ordering temperature [96]. Changes of the ordered magnetic structure with different rare earth elements (REFeAsO) have been extensively studied with neutron diffraction as well as local probe methods. The experiments suggests rather weak interplane coupling which is strongly influenced by the rare earth ion and the associated induced structural changes. The size of the ordered moment as a function of RE has been a topic of considerable interest. Thus, on the basis of these neutron diffraction results, the Fe moment size varies considerably with rare earth element.

Neutron diffraction measurements on $BaFe_2As_2$ [97], $SrFe_2As_2$ [98], and $CaFe_2As_2$ [99] all indicate a magnetic structure characterized by a $(101)_O$ wavevector (where the orthorhombic

cell is defined such that c > a > b) with moments oriented along the a axis arranged antiferromagnetically along a and ferromagnetically along b. Neighboring layers are stacked antiparallel to one another along the c-axis. Note that in tetragonal notation, this wavevector corresponds to $(\frac{1}{2}\frac{1}{2}1)_T$. The odd-integer value of L in the ordering wavevector is a consequence of the antiferromagnetic stacking along the c-axis together with the presence of two layers in a tetragonal unit cell. Neutron diffraction experiments on the 122 materials find larger ordered magnetic moments than in the 1111 materials. This consistency of the ordered moment occurs despite a large variation in transition temperatures ranging from 90 K [100] to 220 K [98]. The phase transition in the AFe_2As_2 compounds is rather abrupt and the continuous or discontinuous nature of the phase transition in these compounds has been a topic of considerable study. An abrupt change in the order parameter in of itself is not evidence of a first-order transition and may simply be the result of a small critical exponent, β, in a continuous transition. Hovewer, the magnitude of the hysteresis is sample dependent making it difficult to extract the true nature of the phase transition. In addition to hysteresis, further evidence for the first-order nature of the transition was shown in the form of phase coexistence over a finite temperature range observed in neutron diffraction experiments on a single crystal sample of $SrFe_2As_2$ [101]. Finally we discuss the evolution of the magnetic structure with doping. Most measurements have focused on $Ba(Fe_{1-x}Co_x)_2As_2$ as the crystals are considered to be homogeneous. NMR measurements [102] and ^{57}Mössbauer measurements [103] were taken as evidence that the SDW order evolves from commensurate for the parent compound to incommensurate in the presence of Co doping. However, an incommensuration significantly smaller than this resolution is certainly possible. Furthermore, the resolution along the orthorhombic k direction (the vertical direction experimentally) is very coarse and an incommensuration along this direction would be difficult to detect in these experiments. High resolution neutron diffraction experiments are needed to resolve this issue.

The data related to 11 systems are consistent with a collinear spin structure [61, 62], as shown in Fig. 1.3.1.1(b). In both the orthorhombic and monoclinic unit cells, there is no cell doubling or cell rotation when compared to the tetragonal cell and, hence, the Miller indices of Bragg reflections are the same for all unit cells [61]. Recent neutron diffraction measurements indicate ordering with the same commensurate $(\frac{1}{2}0\frac{1}{2})$ wavevector in the case of $Fe_{1.075}Te$ [61] and $Fe_{1.068}Te$ [62] where the low temperature structure is monoclinic. The more recent studies

indicated an ordered moment of 2.03 μB for x = 0.075 [61] and 2.25 μB for x = 0.068 [62] with the majority of the moment along the crystallographic b-axis [61, 104]. Interestingly, the samples which exhibit a low temperature orthorhombic structure are found to order magnetically with an incommensurate wavevector of ($\pm\delta$ 0 12) with $\delta \approx 0.38$ [61]. The addition of Se causes the long range magnetically ordered state to evolve into short range order centered at incommensurate wavevectors (0.5$-\delta$ 0 0.5) [104, 61]. The wavevector observed in the 11 materials is different than that observed in the 1111 or 122 materials with an in-plane wavevector of $(\frac{1}{2}0)_T$ as opposed to $(\frac{1}{2}\frac{1}{2})_T$ seen in both the 1111 and 122 compounds. Interestingly, this happens despite calculated Fermi surfaces that are very similar suggesting that the 11 materials should be susceptible to a nesting instability with the same $(\frac{1}{2}\frac{1}{2})_T$ nesting wavevector [105]. Calculations indicate that excess Fe in these materials is magnetic [106], consistent with the conclusions of neutron structure refinements [61]. However, these calculations indicate that the lowest energy ground state is still the $(\frac{1}{2}\frac{1}{2})_T$ state [106] even in the presence of excess Fe. It was further proposed that the excess Fe could cause a mismatch in size between the Γ and M parts of the Fermi surface which could lead to incommensurate magnetism [107]. Experimentally, ARPES measurements confirmed the calculated Fermi surface and further showed that the Γ and M parts of the Fermi surface are closely matched [108]. In addition, despite a weak feature at the X point, these measurements seem to rule out Fermi surface nesting along the observed $(\frac{1}{2}0)_T$ wavevector. As Fermi surface nesting seems very unlikely in this case, theoretical approaches to understand the ordering have focused on local moment models. First-principles calculations have predicted bicollinear order due to the presence of near-neighbor, nextnear-neighbor and next-next-near-neighbor interactions [109]. This model was expanded upon and the phase space of the various exchange constants was explored indicating not only ordering with the commensurate $(\frac{1}{2}0)_T$ wavevector but also incommensurate ordering [110] as observed experimentally with higher amounts of excess Fe [61]. It was also suggested that interaction of the FeTe spins with the magnetic excess Fe moments could modify the superexchange interactions leading to the incommensuration observed experimentally [110].

1.4 Electronic Properties

The basic structural feature connecting the Fe-based superconductors is the presence of square planar sheets of Fe coordinated tetrahedrally by pnictogens or chalcogens and nominal Fe valence

near Fe^{2+}. The structure of FeSe, that is the simplest of the compounds, consists of square planes of Fe with Se atoms arranged above and below the planes in such as way as to tetrahedrally coordinate the iron (Fig. 1.1.1). The other FeSC compounds may be regarded as based on the same square planar sheets with Se replaced by As and counter-ions inserted in such awayas to maintain the nominal Fe valence. Also, we note that the structure places the Fe atoms closer together than in a perovskite, so that direct Fe–Fe interactions are important.

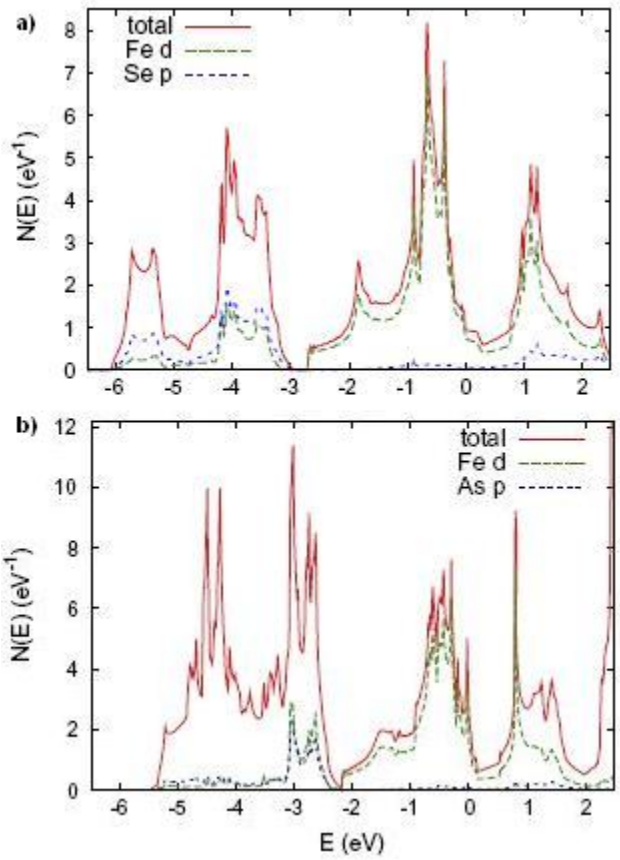

Fig. 1.4.1 *Calculated electronic density of states for (a) FeSe and for (b) LaFeAsO and the relative projections onto atom centered spheres of radius 2.1 Bohr [10].*

The electronic structures of the various compounds as obtained within density functional theory have been reported by a number of authors [9, 92, 93, 111, 112]. While these differ in detail a number of common features are present. The electronic density of states (DOS) of FeSe (Fig. 1.4.1), as obtained in the local density approximation (LDA) [105], show that the main Se p bands are well below the Fermi energy and the DOS from 2.5 eV to 2 eV is dominated by Fe d

states, with only a modest admixture of Se character, similar to the level of covalency in typical oxides. The arsenides are similar as shown in Fig. 1.4.1 for LaFeAsO. In that compound the main As p bands occur between 5.5 and 2 eV with respect to the Fermi energy, E_F, and again the bands near E_F are dominated by Fe d character. This implies that from a crystal chemical point of view the Se and As are anionic, Se^{2-} and As^{3-} and that the electronic structure near E_F should be regarded as derived from metallic square lattice sheets of Fe^{2+} embedded in tetrahedral holes of the anion lattice [10]. This picture has been confirmed by core-level and valence photoemission experiments, which show the bands near E_F to be predominantly Fe in character [113] and the modest d–p hybridization is common to the Fe, Co and Ni.

Theoretical calculations demonstrate that the pnictogen/chalcogen height, h, play a key role in the electronic properties of the Fe-based compounds [114]. The longer h for the 11 family generates more ionic character of the bonding between iron and anion atoms, while the shorter h for the 1111 family leads to more covalent-bonding character, the larger spread of the Wannier orbitals, and more efficient screening by the anion p orbitals [9, 115]. There is also a previous work claiming that the spin and the charge susceptibility are sensitive to h [116].

An examination of the DOS (Fig. 1.4.1) shows that Fe d manifold is split into two main peaks. These are separated by a rather prominent pseudogap, with E_F occurring towards the bottom and magnitude of six electrons for Fe. But a tetrahedral crystal field scheme, such as might arise if the Fe–As (Se) interactions were dominant, would have a gap at four electrons per Fe, since in a tetrahedral ligand field the e_g levels would be below the t_{2g} levels. Instead, the position of the pseudogap shows the importance of direct Fe–Fe interactions in the formation of the band structure. While the family-dependent semimetallic splitting of the bands primarily consists of d_{xz}/d_{yz} and $d_{x^2-y^2}$ orbitals, the size of the pseudogap structure is controlled by the hybridization between these orbitals and $d_{xy}/d_{3z^2-r^2}$.

At this time the mechanism for superconductivity has not yet been established. Detailed calculations have shown that the superconductivity cannot be understood in terms of standard electron–phonon theory [92, 117]. The presence of multiple bands at the Fermi level makes the situation much more complicated and exotic because the Fermi surface consists of disconnected two-dimensional hole and electron pockets centered at Γ and M points, respectively (Fig. 1.4.2) [92]. Because the hole and the electron pockets are similar in both shape and volume, the interband nesting between these pockets may generate spin fluctuations at Q = $(\pi, 0)$ (in a Brillouin

zone defined by the unit cell containing one iron). If such a spin fluctuation is responsible for the electron pairing, a sign reversal of the SC-gap function occurs between the hole and the electron pockets, resulting in $s_{\pm}$-wave symmetry [92, 116, 118].

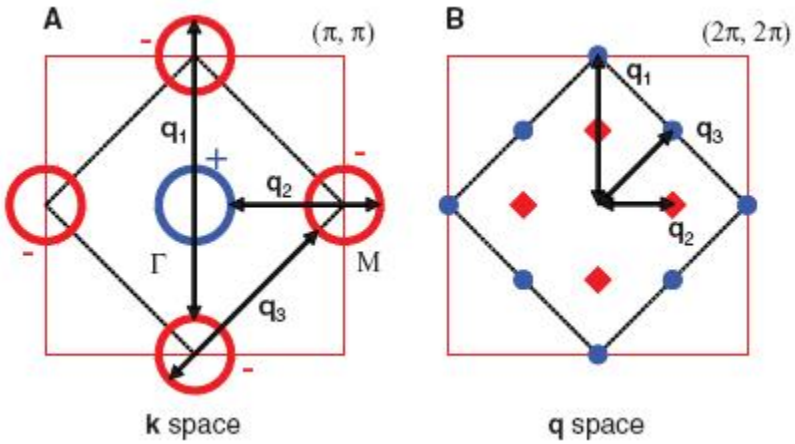

Fig. 1.4.2 *Schematic of reciprocal-space electronic states of an iron-based superconductor. (A) Fermi surface and inter-Fermi-pocket scatterings in k space. According to a band calculation , there are two electron cylinders around* Γ *and M points, respectively. For simplicity, two Fermi cylinders are representes by one circle. The black dotted diamond denotes the crystallographic Brillouin zone, and the red squares indicates the unfolded Brillouin zone defined by the unit cell containing one iron atom. Signs of the SC gap expected for* $s_{\pm}$*-wave symmetry are shown by different colors. The arrows denote inter-Fermi-pocket scatterings.* q_2 *and* q_3 *connect different pockets, whereas* q_1 *is an umklapp process. (B) Expected QPI spots in q space associated with inter-Fermi-pocket scatterings. Blue filled circles and red filled diamonds represent sign-preserving and sign-reversing scatterings, respectively, for the* $s_{\pm}$*-wave SC gap. The former will be enhanced by a magnetic field, whereas the latter may be suppressed [120].*

Also, there is a clear association, e.g. in the phase diagrams, between superconductivity and suppression of the SDW, either by doping or by pressure. Considering the evidence for spin fluctuations in the normal state and the similarity of the normal states above the SDW transition and above the superconducting transition, it is tempting to consider pairing based on spin fluctuations. Therefore the strongest interaction will be at (π, π) similar to the SDW, and will favor opposite sign order parameters on Fermi surface sections separated by this wavevector. Therefore, within the simplest scenario an s symmetry state with opposite sign order parameters

on the electron and hole sections might be expected. This is the $s\pm$ state proposed by Mazin et al. and by Kuroki et al. [92, 116]. The same electrons that drive the spin-fluctuations (i.e. those on the nested Fermi surface) are the electrons that are involved in either the SDW order or the superconductivity [120]. Therefore, both the SDW and superconductivity are Fermi surface instabilities, driven by the same interaction and competing for the same electrons. As mentioned, both the superconducting and SDW orders arise from a normal state that already has strong antiferromagnetic correlations and so perhaps may be regarded as related. In this case, while there is clearly a competition for electrons between the two orders, one may ask whether they can coexist. In general, very soft fluctuations (energy below the gap) are pair breaking in superconductivity since the superconducting state is unstable against condensation of the fluctuations (i.e. magnetic order). In addition, we recall that the orbital character on the electron Fermi surfaces of the FeSC is mixed, with d_{xz}/d_{yz} and other orbitals and that the mixture varies strongly with k. This implies the the nesting related coupling also varies.

The possible scenario about the superconducting mechanism point out on the important role of interplay between electronic, lattice and magnetic degrees of freedom. It is already established that the Fe *3d* states give rise to the superconductivity, however the details about the Fermi Surface (symmetry of gap, geometry of involved orbitals, spectral weight) are different in each Fe-based compound.

Chapter 2

X-ray absorption spectroscopy

2.1 General aspects of X-ray Absorption

The interaction processes between matter and electromagnetic radiation are based on three different phenomena:

- Photoelectric effect;
- Scattering from free electrons (Thompson and Compton);
- Production of electron-positron pairs.

The probability of each event is related to the cross section associated with each process (Fig. 2.1.1).

When the incident x-ray has an energy equal to that of the binding energy of a core-level electron, there is a sharp rise in absorption: an absorption edge corresponding to the promotion of this core level to the continuum. For XAFS, we are concerned with the intensity of μ as a function of energy, near and at energies just above these absorption edges. An XAFS measurement is simply a measure of the energy dependence of μ at and above the binding energy of a known core level of a known atomic species. Since every atom has core-level electrons with well-defined binding energies, we can select the element to probe by tuning the x-ray energy to an appropriate absorption edge. These absorption edge energies are well-known (usually to within a tenth of percent), and tabulated. The edge energies vary with atomic number approximately as Z^2, but both K and L levels can be used in the hard x-ray regime (in addition, M edges can

be for heavy elements in the soft x-ray regime), which allows most elements to be probed by XAFS with x-ray energies between 5 and 35 keV. Because the element of interest is chosen in the experiment, XAFS is element-specific.

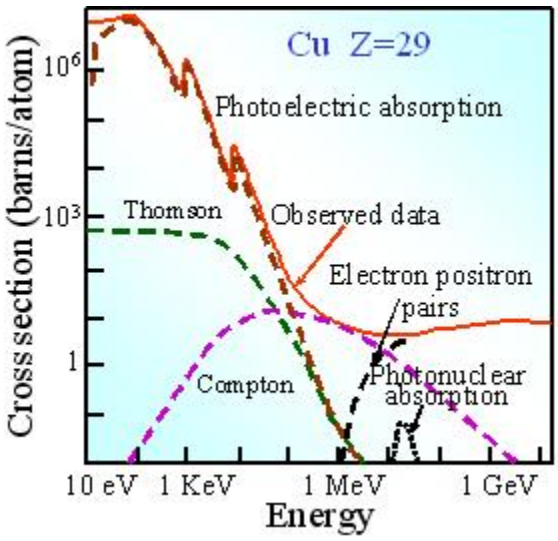

Fig. 2.1.1 *Theoretical and experimental cross section for copper.*

Following an absorption event, the atom is said to be in an excited state, with one of the core electron levels left empty (a so-called core hole), and a photo-electron. The excited state will eventually decay typically within a few femtoseconds of the absorption event. There are two main mechanisms for the decay of the excited atomic state following an x-ray absorption event. The first of these is x-ray fluorescence, in which a higher energy electron core-level electron fills the deeper core hole, ejecting an x-ray of well-defined energy. The fluorescence energies emitted in this way are characteristic of the atom, and can be used to identify the atoms in a system, and to quantify their concentrations. For example, an L shell electron dropping into the K level gives the K fluorescence line. The second process for de-excitation of the core hole is the Auger Effect, in which an electron drops from a higher electron level and a second electron is emitted into the continuum (and possibly even out of the sample). In the hard x-ray regime ($>$ 2 keV), x-ray fluorescence is more likely to occur than Auger emission, but for lower energy x-ray absorption, Auger processes dominate. Either of these processes can be used to measure the absorption coefficient μ, though the use of fluorescence is somewhat more common. In correspondence of an edge, the absorption coeffcient exhibits the X-ray Absorption Fine Structure (XAFS). For isolated atoms (noble gases, metallic vapors)the XAFS is limited to a few eV around the

edge, and respects the transitions of the core electron to Rydberg level. In molecular gases and condensed systems the XAFS, strongly influenced by the presence of the atoms surrounding the absorber one, can extend up to one thousand eV above the edge (Fig. 2.1.2). X-ray absorption can be viewed as low energy electron diffraction where the photo-absorber plays both the roles of the source and of the detector for emitted photoelectrons. XAFS is customarily divided into two regions.

- The structure within 30-50 eV above the edge is called XANES (X-ray Absorption Near Edge Structure) or NEXAFS (Near Edge X-ray Absorption Fine Structure). From XANES, information can be obtained on the local electronic as well as geometric structure. Sometimes, the structure within a few eV around the edge is distinguished as edge structure.
- The fine structure extending from the XANES region up to typically one thousand eV is called EXAFS (Extended X-ray Absorption Fine Structure). EXAFS carries information on the local geometric structure surrounding a given atomic species. The interpretation of EXAFS is nowadays rather well established, and easier than the interpretation of XANES.

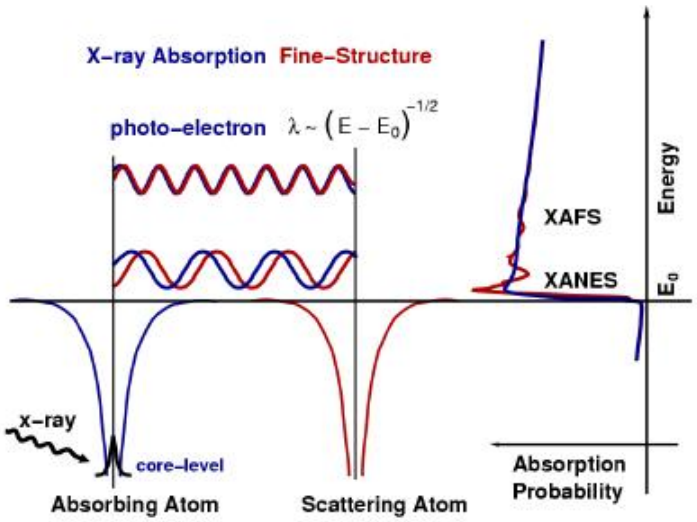

Fig. 2.1.2 *XAFS occurs because the photo-electron can scatter from a neighboring atom. The scattered photo-electron can return to the absorbing atom, modulating the amplitude of the photo-electron wave-function at the absorbing atom. This in turn modulates the absorption coefficient $\mu(E)$, causing the EXAFS.*

The difference between XANES and EXAFS can be explained in a very simply manner by the comparison between the photoelectron wavelength (λ) and the interatomic distance of the photoabsorber-backscatterer pair. The photoelectron kinetic energy E_{Kin} is connected with the wavelength (λ) by the following relation

$$E_{Kin} = \hbar\omega - E_{bin} = \frac{\hbar^2 k^2}{2m} = \frac{\hbar^2 (2\pi)^2}{2m\lambda^2} \tag{2.1.1}$$

where $\hbar\omega$ is the incident photon energy and E_{bin} is the binding energy of the electron with mass m; that means that for high energy the wavelength λ is shorter than interatomic distances and hence the EXAFS region corresponds to a single scattering regime; while for lower E, λ is larger than interatomic distances and the XANES region is associated with a multiple scattering regime (Fig. 2.1.3).

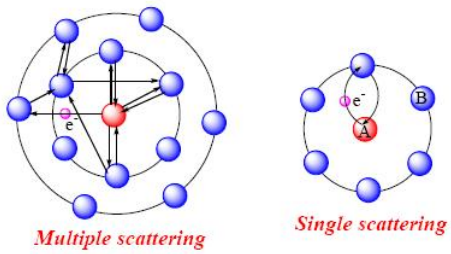

Fig. 2.1.3 *Photoelectron path in case of single scattering (EXAFS) and multiple scattering (XANES)*

Quantitative informations can be extracted by EXAFS analysis.

The phase relationship between outgoing and incoming waves depends on photo-electron wavelength and inter-atomic distance R. The variation of phase relationship as a function of photon energy influences the final state amplitude at the core site, giving rise to an interference phenomenon which modulates the absorption. The frequency of EXAFS oscillations depends on the distance between absorber and back-scatterer atoms. Their amplitude is proportional to the number of back-scatterer atoms. Two main peculiarities characterize EXAFS:

- the selectivity of atomic species, which is achieved by tuning the x-ray energy to the corresponding absorption edge;

- the insensitivity to long-range order, due to the short mean free path of the photoelectron, typically limited to about 10 Å.

These peculiarities make EXAFS a very appealing local structural probe. In many atomic non-crystalline systems, like semiconductor amorphous alloys or oxide glasses, the atomic selectivity allows to separately study the environment of each component atom. EXAFS is an invaluable tool for systems in which the functional properties are due to individual atoms or small clusters embedded in a matrix of different atomic species, like heterogeneous catalysts, active sites in biomolecules, impurities in semiconductors, luminescent rare-earth atoms in crystals and glasses. A brilliant application of EXAFS concerns crystalline solids in which the local structural properties are different from the average properties detected by diffraction.

2.2 Extended X-Ray Absorption Fine Structure (EXAFS)

In this section, a simple physical description of the XAFS process and the origin of the EXAFS Equation will be given. As described above, we start with the photoelectric effect, in which an x-ray is absorbed by a core-level with binding energy, and a photo-electron with wave number k is created and propagates away from the atom. An important point for the discussion here is that the absorption due to a given core-level relies on there being an available state for the photo-electron: a quantum state at exactly the right energy, and also the right angular momentum state. If there is no available state, there will be no absorption from that core level.

When a neighboring atom is included in the picture, the photo-electron can scatter from the electrons of this neighboring atom, and the scattered photo-electron can return to the absorbing atom. Since the absorption coefficient depends on whether there is an available electronic state, the presence of the back-scattered photo-electron from the neighboring atom will alter the absorption coefficient: this is the origin of XAFS.

We'll now develop the XAFS equation using a slightly more formal description of this simple physical picture. Since x-ray absorption is a transition between two quantum states (from an initial state with an x-ray, a core electron, and no photo-electron to a final state with no x-ray, a core hole, and a photo-electron), we describe $\mu(E)$ with Fermi's Golden Rule:

$$\mu(E) \propto |< i|H|f >|^2 \tag{2.2.1}$$

where $< i|$ represents the initial state (an x-ray, a core electron, and no photo-electron), $|f >$ is the final state (no x-ray, a core-hole, and a photo-electron), and H is the interaction term (which we'll come back to shortly). Since the core-level electron is very tightly bound to the absorbing atom, the initial state will not be altered by the presence of the neighboring atom. The final state, on the other hand, will be affected by the neighboring atom because the photo-electron will be able to see it. If we expand $|f >$ into two pieces, one that is the "bare atom" portion ($|f_0 >$) , and one that is the effect of the neighboring atom ($|\Delta f >$) , as

$$|f >= |f_0 > + |\Delta f > \tag{2.2.2}$$

we can expand Eq. 2.2.1 to

$$\mu(E) \propto |< i|H|f_0 >|^2 \left[1 + < i|H|\Delta f > \frac{<f_0|H|i>*}{|< i|H|f_0 >|^2} + C.C.\right] \tag{2.2.3}$$

where C.C. means complex conjugate. We've arranged the terms here so that this expression resembles the relationship between $\mu(E)$and $\chi(E)$,

$$\mu(E) = \mu_0(E)\left[1 + \chi(E)\right] \tag{2.2.4}$$

We can now assign $\mu_0(E) = |< i|H|f_0 >|^2$ as the "bare atom absorption", which depends only on the absorbing atom – as if the neighboring atom wasn't even there. We can also see that fine-structure can be written as

$$\chi(E) \propto < i|H|\Delta f > \tag{2.2.5}$$

We can work this out (at least roughly) as an integral equation fairly easily. The interaction term H is probably the most mysterious part – it represents the process of changing between two energy, momentum states. If you're familiar with quantum radiation theory, the interaction term needed is the $p \cdot A$ term, where A is the quantized vector potential (the $A \cdot A$ term, but

this does not contribute to absorption). For the purposes here, this reduces to a term that is proportional to e^{ikr}. The initial state is a tightly bound core-level, which we can approximate by delta function (a 1s level for atomic number Z extends to around a_0/Z, where a_0 is the Bohr radius of ~ 0.529Å). The change in final state is just the wave-function of the scattered photo-electron, $\psi_{scatt}(r)$. Putting all these terms together, we get a simple expression for the EXAFS:

$$\chi(E) \propto \int dr\delta(r)\psi_{scatt}(r)e^{ikr} = \psi_{scatt}(0) \tag{2.2.6}$$

We can further evaluate the amplitude of the scattered photo-electron at the absorbing atom, to get the EXAFS equation. Describing the outgoing photo-electron wave-function (k, r) traveling as a spherical wave,

$$\psi(k,r) = \frac{e^{ikr}}{kr} \tag{2.2.7}$$

traveling a distance R to the neighboring atom, then scattering from a neighbor atom, and traveling as a spherical wave a distance R back to the absorbing atom. We simply multiply all these factors together to get

$$\chi(E) \propto \psi_{scatt}(k, r=0) = \frac{e^{ikr}}{kR}\left[2kf(k)e^{i\delta(k)}\right]\frac{e^{ikr}}{kR} + C.C. \tag{2.2.8}$$

where $f(k)$ and $\delta(k)$ are scattering properties of the neighboring atom. As mentioned before, these scattering factors depend on the Z of the neighboring atom, as shown in Fig 2.2.1. These scattering factors make EXAFS sensitive to the atomic species of the neighboring atom. Combining these terms in and including the complex conjugate to make sure we end up with a real function, we get

$$\chi(k) = \frac{f(k)}{kR^2}sin\left[2kR + \delta(k)\right] \tag{2.2.9}$$

which starts to look much like the EXAFS equation.

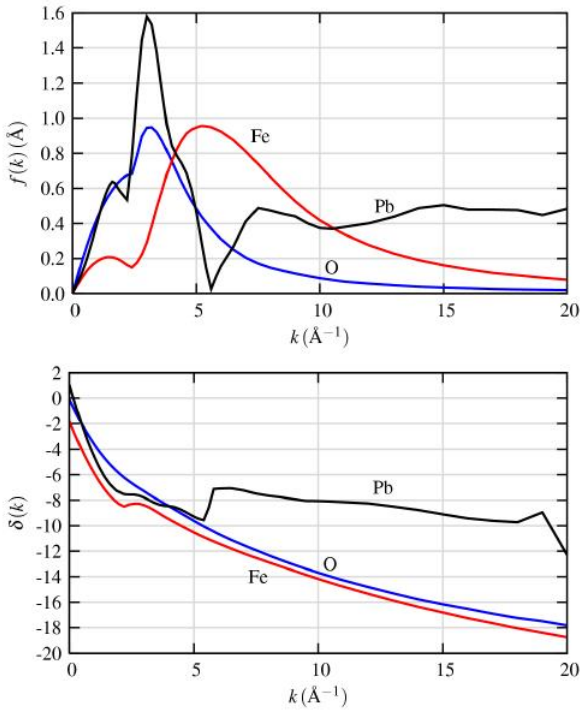

Fig. 2.2.1 *Functional forms for f(k) (top) and delta(k) (bottom) for O, Fe, and Pb showing the dependence of these terms on atomic number Z.*

The treatment here was for one pair of absorbing atom and scattering atom, but for a real measurement we'll average over millions of atom pairs. Even for neighboring atoms of the same type, the thermal and static disorder in the bond distances will give a range of distances that will affect the XAFS. As a first approximation, this disorder will change the XAFS equation to

$$\chi(k) = \frac{Ne^{-2k^2\sigma^2} f(k)}{kR^2} sin\left[2kR + \delta(k)\right] \tag{2.2.10}$$

where N is the coordination number and σ^2 is the mean-square-displacement in the bond distance R. Of course, real systems usually have more that one type of neighboring atom around a particular absorbing atom. This is easily accommodated in the XAFS formalism, as the measured XAFS will simply be a sum of the contributions from each scattering atom type (or coordination shell, as it is often called - the terms coordination sphere and scattering path are also used),

$$\chi(k) = \sum_i \frac{N_i e^{-2k^2\sigma_i^2} f_i(k)}{kR_i^2} sin\left[2kR_i + \delta_i(k)\right] \tag{2.2.11}$$

where i represents the individual coordination shell of identical atoms at approximately the same distance from the central atom. In principle there could be many such shells, but as shells of similar Z become close enough (i.e., within a 0.05Åof each other), they become difficult to distinguish from one another.

The simple treatment leading to Eq. (2.2.11) does not take into account anelastic effects. Two types of anelastic effects are generally distinguished: *intrinsic* and *extrinsic*, referring to many-body interactions within and outside the absorber atom, respectively.

Intrinsic anelastic effects are the multiple excitations within the absorber atom giving rise to the anelastic part μ_{anel} of the absorption coeffcient. Multiple excitations modify the photo-electron energy and thence the interference conditions between outgoing and incoming waves. The net effect is a reduction of the coherent EXAFS signal with respect to that expected for purely elastic excitations. The fraction of total absorption giving rise to elastic excitations is measured by the superposition factor S_0^2. Intrinsic anelastic effects are thus taken into account in Eq. (2.2.11) by a factor S_0^2, which typically amounts to $0.7 \div 0.9$.

Extrinsic anelastic effects are taken into account as a mean free path λ, to which two distinct phenomena contribute:

a) the core-hole lifetime τ_h, depending on the atomic number Z, which establishes the distance $\lambda_h = v\tau_h$ the photo-electron can travel before the absorber atom de-excitation;

b) the energy-dependent photo-electron mean-free path λ_e, determined by the anelastic interactions with other electrons outside the absorber atom. The smaller of the two contributions determines the actual value of λ:

$$1/\lambda = 1/\lambda_h + 1/\lambda_e \tag{2.2.12}$$

At low energies, in the XANES region, the mean free path is determined by λ_h, while in the EXAFS region the contribution of λ_e is predominant. The extrinsic anelastic effects are generally taken into account in the EXAFS formula by a phenomenological factor $e^{(-2R_i\lambda)}$, with $\lambda \approx 5 \div 15$Å. The mean free path factor progressively reduces the amplitude of EXAFS

oscillations when R_i increases, contributing to making EXAFS insensitive to long range order. To summarize, the EXAFS equation taking into account anelastic effects is:

$$\chi(k) = S_0^2 \sum_i \frac{N_i e^{-2r/\lambda(k)} e^{-2k^2\sigma_i^2} f_i(k)}{kR_i^2} sin\left[2kR_i + \delta_i(k)\right] \tag{2.2.13}$$

From this equation, we can draw a few physical conclusions about XAFS. First, because of the $\lambda(k)$ term and the R^{-2} term, XAFS is seen to be an inherently *local probe*, not able to see much further than 5 or so Angstroms from the absorbing atom. Second, the XAFS oscilations will consist of different frequencies that correspond to the different distances for each coordination shell. This will lead us to use Fourier transforms in the analysis. Finally, in order to extract the distances and coordination numbers, we need to have accurate values for the scattering amplitude and phase-shifts *f(k)* and $\delta(k)$.

2.2.1 Effects of thermal vibrations and gaussian disorder

Every real physical system is affected by thermal disorder, due to the thermal motion of atoms, whose amplitude increases with temperature but is not negligible even near zero kelvin. The period of atomic vibrations ($\approx 10^{-12}s$) is much larger than the photo-electron time of flight ($10^{-16} \div 10^{-15}s$). An EXAFS spectrum, resulting from the contributions of a large number of photo-electrons, samples a *distribution* of instantaneous interatomic distances r for each coordination shell. The distribution of interatomic distances can be further enlarged and modified by the presence of structural disorder. For example, distorted coordination shells are characterized by the presence of two or more slightly different interatomic distances. Another example are systems in which the absorber atom has at least two structurally different sites, which cannot be discriminated as different coordination shells. A different kind of disorder is compositional disorder, consisting in the presence of atoms of different species in the same coordination shell.

To highlight the effects of thermal vibrations and gaussian disorder, let us to show a different form of EXAFS equation:

$$\chi(k) = Im \sum_i A_i(k) G(R_i) e^{i[2kr_i + \delta_i(k)]} \tag{2.2.14}$$

where $A_i(k)$ and $G(R_i)$ represent the factor form for the i-atom and the mean free-path term,

respectively.

To taking in account the effect of the thermal vibrations and gaussian disorder, we can define the probability that the i-atom in the j-shell occupy the position $r_i, r_i + dr_i$, centred at the mean value R_i. Considering a Gaussian distribution form of this probability

$$P_i^j(r_i) = \frac{e^{-\frac{r_i - R_j}{2\sigma_i^2}}}{\sqrt{2\pi\sigma_i^2}} \tag{2.2.15}$$

and the integrating over all possible dr_i around the mean value, we obtained a Debye-Waller factor

$$Q_i(k) = e^{-2k^2\sigma_i^2} \tag{2.2.16}$$

where σ_i^2 is the mean square relative deviation arond the mean value R_i. It should be recalled that the EXAFS Debye-Waller (DW) factor is not the same as the one observed by diffraction experiment. While diffraction takes into account the mean-square deviation of a given atom from its average site in the crystal, EXAFS Debye-Waller factor measures the broadening of the distance between two atomic sites, i.e. represents the distance broadening between the absorber and the scatterer.

An expression for σ as a function of temperature can be found considering the Debye approximation for lattice vibration, in harmonic regime. However, the temperature dependence of σ is described by Einstein model for the lattice vibrations, assuming a monochromatic spectrum. The phonon modes that contribute at the first shell have a like-δ weight, thus the Einstein model predicts

$$u_i^2 = \frac{\hbar}{M_i\omega_i}\frac{1}{e^{\hbar\omega/k_BT} - 1} \tag{2.2.17}$$

where M_i and ω_i are the atomic mass and the vibrational frequency, respectively. If the motion of nearest neighbors is completly uncorrelated and σ_{ij}^2 between the i-atom and the j-atom is given by $u_i^2 + u_j^2$, we obtained the following expression:

$$\sigma_{ij}^2 = \frac{\hbar}{M_r\omega}\frac{1}{e^{\hbar\omega/k_BT} - 1} \tag{2.2.18}$$

where M_r is the reduced mass of the absorber-scattered atomic pair; the vibrational frequency ω can be obtained by fitting process, plotting the data as a function of temperature.

Concluding, the Debye approximation better reproduces the lattice vibrations for primitive lattices and from second atomic shell, on the other hand the Einstein model can be applied for the first atomic shell and more complex structure, as molecules and amorfous solids.

2.2.2 Effects of anisotropy

In the EXAFS expression (2.2.13) we assume implicitly that the sample is not oriented. If the sample is anisotropic, the EXAFS too is anisotropic and allows to extract information on the angular dependence of the structure around the absorber atom.
The EXAFS anisotropic theory is deriveted by Maxwell equations. An electromagnetic plane wave, with wavevector q and ωfrequency that si propagated along x direction is given by:

$$E(q,x) = E_0 e^{iqx} \tag{2.2.19}$$

where E_0 is the wave amplitude. From Maxwell equation:

$$q^2 = \frac{n^2\omega^2}{c^2} \tag{2.2.20}$$

where the index rifraction n is related to permeability ε_r by $\varepsilon_r = n^2$ and c is the light speed in vacuum. Assuming that ε_r is equal to the permeability in vacuum, then we can write in the X-ray region:

$$\varepsilon_r \approx 1 + \varepsilon_2 \tag{2.2.21}$$

where ε_2 is real and less than unit. Substituting the previous expression in the eq. (2.2.20) :

$$q \approx \frac{\omega}{c}(1 + \frac{i\varepsilon}{2}) \tag{2.2.22}$$

The Lambert-Beer law can be re-writed as:

$$I = I_0 e^{-\frac{\omega \varepsilon_2 x}{c}} \tag{2.2.23}$$

We can finally obtain the relation for the absorption coefficient:

$$\mu = \frac{\omega \varepsilon_2}{c} \tag{2.2.24}$$

beacuse ε_2 is a 2D tensor in the X-ray region. The dependence of orientation in ε_2, that is the angle between the polarization vector of electromagnetic field and the cristallographic axis is well know. If the rotation axis has a symmetry equal to more than three, then ε_2 e μ are angle indipendent and remain constant during the rotation.
In case of edge K and L_1, the EXAFS related to oriented sample assumes the form:

$$\chi(k) = \frac{m}{4\pi\hbar^2 k} \sum_i \frac{3cos^2\theta_i}{R_i^2} N_i t_i(2k) e^{-2R_i/\lambda} Q_j(k) e^{-2k^2\sigma_i^2} sen[2kR_i + \delta_i(k)] \tag{2.2.25}$$

where θ_i is the angle between the polarization vector of electromagnetic field and the direction idientified by absorber-scattered atomic pair.

The term $3cos^2\theta_i$ includes directional effect. In the case of powder sample or polycrystalline sample with no preferred orientation, or an amorphous solid, the $\chi(k)$ must be averaged over θ_i, and therefore $\langle 3cos^2\theta_i \rangle = 1$.

2.3 Fluorescence EXAFS

Fluorescence EXAFS has several advantages over the conventional transmission mode specially to study complex systems such as high T_C superconductors as the case of the present work. Also the thickness effects are unimportant while they strongly affect transmission signal. The fluorescent EXAFS mode is based on the detection of the X-rays emitted as a result of the process which fills the core hole created by optical absorption. The process is illustrated in Fig. 2.3.1.
The absorption of a photon, by excitation of a core electron, leaves the atom in a very unstable state. The hole, left in the core level tends to be occupied by an electron which decays from

an upper occupied level, emitting X-ray photons. The energy of this radiation is characteristic of the absorbing element and is smaller than the original exciting radiation. The background consists of radiation of elastic and Compton scattering.

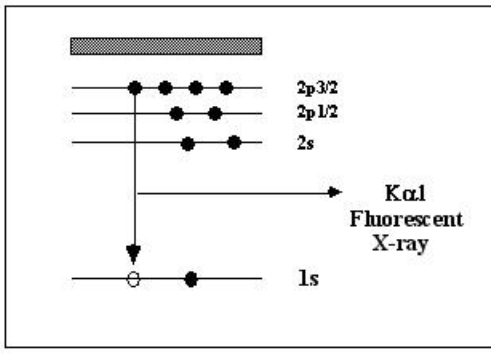

Fig. 2.3.1 *Decay process of a 1s hole in the fluorescence mode of X-rays.*

In the fluorescence EXAFS , the yield due to characteristic fluorescence is collected as a function of photon energy. The ratio of the total collected fluorescence photons with respect to the incident photons, provides the absorption signal due to partial cross-section of the selected initial state core level. The fluorescence detection is an attractive technique, because of its extreme sensitivity to specific atomic species. On the contrary in the transmission EXAFS measurements, one measures the total absorption coefficient that is the sum of the contributions from the core levels of all different atomic species of the system that have binding energies lower than the photon energy $h\nu$. The contribution from other initial states has to be subtracted from the total absorption in the data analysis.

In the fluorescence mode the total detected photon flux is the sum of the fluorescence signal, if of interest, and a background signal, due to elastic scattering, Compton scattering and other fluorescence of the sample. In general, a correction (the so called fluorescence correction) has to be made to the measured signal in the fluorescence EXAFS. This correction should be made also keep in consideration the geometry of the system.

2.4 EXAFS data analysis

There are two main steps in the EXAFS data analysis. First, a preliminary data processing is required, as pre-edge subtraction, data normalisation and transformation to the k-space etc.

Secondly, the data are analyzed to extract the parameters of interest.

The removal of the pre-edge background generally involves a fitting of the data before the edge to some functional form and extrapolation of this function into the data region. For the fluorescence data a linear polynomial is sufficient. After the pre-edge background subtraction, the oscillatory part of the X-ray absorption coefficient is normalized by the smooth monotonically decreasing atomic cross-section of the edge of interest $\mu_0(E)$, according to the equation that defines the EXAFS function $\chi(k) = \frac{\mu(E)-\mu_0(E)}{\mu_0(E)}$. The determination of the atomic absorption coefficient is done empirically by fitting the smooth part of $\mu_0(E)$ with a polynomial function. The E could be transformed into the k scale. Once is determined, the next step is the Fourier analysis. The Fourier transform provides general view of the atomic distribution, around the absorbing site. The Fourier transform peaks corresponds to the interatomic positions (Fig. 2.4.1). However, the peak position in the modulus of the Fourier transform do not provide directly the atomic distances as it needs to be corrected for the phase shifts δ_i.

The second step in the data analysis is to simulate the experimental EXAFS spectrum. The best approach is to start with the parameters provided by diffraction studies. The fitting algorithm used in this work, is based on a standard non linear least-squares technique, which minimize the statistical χ^2, determined by the squares of the difference between the experimental EXAFS signal and the theoretical curve. The number of independent parameters, N, which may be determined by EXAFS, are limited by the number of independent data points: $Nind \sim (2\Delta k \Delta R)/\pi$, where Δk and ΔR [15] are respectively the ranges in k and R space over which the data are fitted. This explains why it is necessary to acquire high k-range data in an EXAFS experiment. The EXAFS signal depends on the following parameters which can be either fixed or allowed to vary: ΔE, shift of the energy origin, S_0^2(reduction factor due to passive electrons contribution), the interatomic distances R_i, Debye Waller factor σ_i^2 and phase shifts. The phase shifts could be either theoretically calculated or taken from experimental standards. For the present analysis, calculated phase shifts have been used.

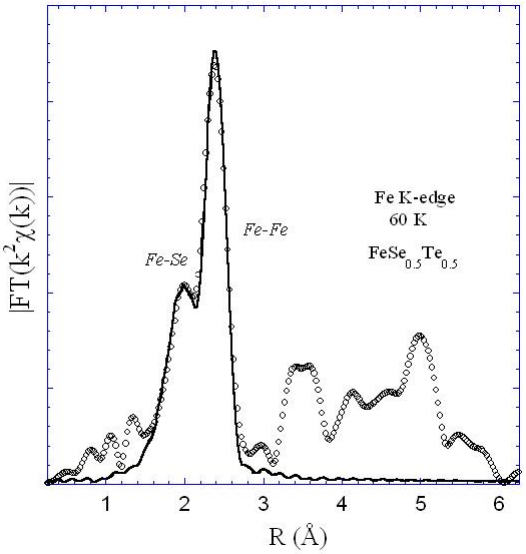

Fig. 2.4.1 *Example of FT analysis on $FeSe_{0.5}Te_{0.5}$ sample [23].*

It should be noted that there is a strong correlation between parameters to be extracted. In particular, correlations between coordination number and Debye-Waller factor on the one hand and those between the distances and phase shifts on the other hand, limit the result accuracy that can be achieved. One the software used for the determination of the parameters, the EXCURVE code, can provide a contour map, showing the correlation between two parameters and the fitting index, and also calculate the correlation matrix involving as many parameters as required.

2.5 X-Ray Absorption Near Edge Structure (XANES)

Finally, we return to the XANES portion of the spectrum. Since XANES is a much larger signal than EXAFS, XANES can be done at lower concentrations, and at less than perfect sample conditions. The interpretation of XANES is complicated by the fact that there is not a simple analytic (or even physical) description of XANES. The main difficulty is that the EXAFS equation breaks down at low-k, due to the k^{-1} term and the increase in the mean-free-path at very low-k. Still, there is much chemical information from the XANES region, notably formal valence (very difficult to experimentally determine in a non-destructive way) and coordination environment. The edge position and shape is sensitive to formal valence state, ligand type,

and coordination environment. If nothing else, XANES can be used as a fingerprint to identify phases.

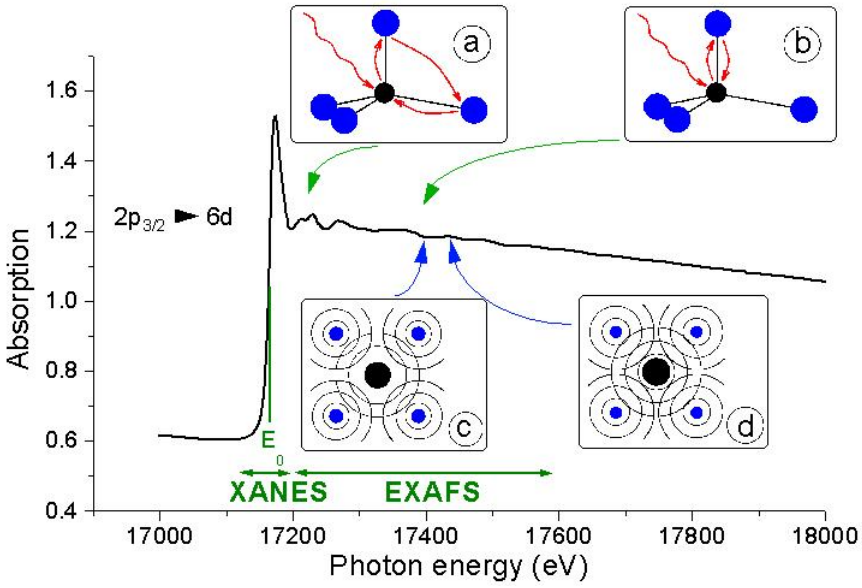

Fig. 2.5.1 *XAS spectrum of U L_3-edge in $CaUO_4$*

For K shell absorption, where the core-level is a *1s* state, the photo-electron has to end up in a *p* state (in general, the photo-electric effect changes the orbital quantum number l to $l \pm 1$). Thus, even if there are available states with the right energy, there might be no *1s* absorption if there are no available *p* states. For EXAFS, where the energies are well-above the threshold energy, this is rarely an important concern. For XANES, on the other hand, this can play a very important role. Transition metal oxides, for example, usually have many unfilled *3d* electrons near the Fermi level, and a filled *3p* band. There are empty *2p* electron states from the oxygen, but these are too far away to appreciably over-lap with the metal *1s* band. Therefore, the metal *3d* electrons do not normally participate in the absorption process unless there is a strong hybridization of the O *2p* and metal *3d* levels. The XANES spectra are then especially sensitive to such hybridization. For ions with unfilled *d*-electrons bands, the *p*-*d* hybridization is dramatically altered depending on the coordination environment, which much stronger hybridization for tetrahedral coordination than for octahedral coordination. Since the photo-electron created due to a *1s* core level (a K-shell) must have *p*-like symmetry, the amount of overlap with the *d*-electron orbitals near the Fermi level can dramatically alter the number of available states to the *p*-electron, causing significant changes in the XANES spectrum.

Though the lack of a simple analytic expression complicates XANES interpretation, XANES can be described qualitatively (and nearly quantitatively) in terms of

- Coordination chemistry: regular, distorted octahedral, tetrahedral coordination.
- Molecular orbitals: $p - d$ orbital hybridization, crystal-field theory, and so on.
- Band-structure: the density of available electronic states.
- Multiple-scattering: multiple bounces of the photo-electron.

The main physical process, determining the XANES of condensed systems, is the photoelectron full multiple scattering. Therefore, the XANES peaks have the same physical origin as "shape resonance" in the scattering of electrons by molecules or neutrons by nuclei, where a particle is trapped for a finite time in a potential well with finite potential barrier in molecules. The general simplified formula, that describes the strong dependence of a "shape resonance" on the interatomic distance, is $k \bullet R\ const$ where k is the wave vector of the photoelectron at the "shape resonance", and R is the interatomic distance. This formula is valid for a relative distance variation less than 10-20% and for a coordination geometry kept constant. Under these limits the formula which relates the variation ΔR in the bond distance to the variation ΔE in the energy of the "shape resonances", is

$$\Delta E/E = -\Delta R/R \tag{2.5.1}$$

where E is the energy difference between the "shape resonance" and the edge energy and ΔR is the variation of distance. For having satisfactory structural information from XANES, the data need to be taken with high resolution, to resolve the "shape resonance" or multiple scattering resonances. Using high quality data with high energy resolution, a useful information on the local geometry can be obtained in complex systems such as high T_c compounds. Being a probe of higher order pair correlation function, the XANES is very sensitive to small atomic displacements.

XANES is considerably harder to fully interpret than EXAFS. Precise and accurate calculations of all spectral features are still difficult, time-consuming, and not always reliable. This situation is improving, but quantitative analyses of XANES using ab initio calculations are very rare.

Still, such calculations can help explain which bonding orbitals and/or structural characteristics give rise to certain spectral features.

2.6 X-ray Synchrotron Radiation

When high-energy particles are in rapid motion, including electrons forced to travel in a curved path by a magnetic field, synchrotron radiation is produced, similar to a radio antenna, but with the difference that, in theory, the relativistic speed will change the observed frequency due to the Doppler effect by the Lorentz factor, γ. Relativistic time contraction then bumps the frequency observed in the lab by another factor of γ, thus multiplying the GHz frequency of the resonant cavity that accelerates the electrons into the X-ray range. The radiated power is given by the relativistic Larmor formula while the force on the emitting electron is given by the Abraham-Lorentz-Dirac force. The radiation pattern can be distorted from an isotropic dipole pattern into an extremely forward-pointing cone of radiation. Synchrotron radiation is the brightest artificial source of X-rays. The planar acceleration geometry appears to make the radiation linearly polarized when observed in the orbital plane, and circularly polarized when observed at a small angle to that plane. Amplitude and frequency are however focussed to the polar ecliptic.

The interesting properties of synchtron radation make it a powerful tool to investigate the condensed matter:

1. Broad Spectrum which covers from microwaves to hard X-rays: the users can select the wavelength required for their experiment.

2. High Flux: high intensity photon beam allows rapid experiments or use of weakly scattering crystals.

3. High Brilliance: highly colliminated photon beam generated by a small divergence and small size source (spatial coherence) .

4. High Stability: submicron source stability .

5. Polarizaton: both linear and circular .

6. Pulsed Time Structure: pulsed length down to tens of picoseconds allows the resolution of process on the same time scale.

The small divergence and the high intensity allow the use of optical systems to manipulate further the radiated photon beam and obtain even more stunning properties: *Mirrors and*

capillaries enable for example focal spots in the micrometer range. *Monochromators* select very fine energy (resp. wavelength) bands and provide thus a selectivity to elements and even to the chemical state of a element. The radiation spectrum is continuous and the energy can be freely chosen according to the system under investigation (*tunability*). X-rays penetrate easily into and even through matter and therefore non-destructive investigations have become of special interest. With the availability of hard X-ray radiation even large pieces (several cm^3) can be investigated. By tuning the energy of the X-rays one can further adjust the penetration depth. Like this, surface or bulk sensitivity is achieved. Variation of the angle of incidence of the X-ray beam changes the penetration depth from surface to bulk, too. The very small divergence allows like this the investigation of thin layers or coatings. Due to the high intensity recording of a spectrum is very fast. Measurements can therefore be carried out during processing the material under investigation. These in-situ experiments provide information about the processes which take place during the transformation of the sample. X-rays again facilitate the use of different sample environments for the sample like furnaces, cryostats, pressure or chemical cells.

Fig. 2.5.1 *Scheme of synchrotron radiation facility*

Chapter 3

Local structure of REFeAsO pnictides

The recent discovery of high-T_C superconductivity in the LaOFeAs [1] has triggered intensive research activities on REFeAsO (RE=rare earth) oxypnictides, producing a large number of publications focusing on different aspects of these materials [121, 122, 123].

The rare earth (RE) oxypnictides (REFeAsO) have a layered structure, with electronically active $(FeAs)^{\delta-}$ layers separated by $(REO)^{\delta+}$ reservoirs. Both the charge transfer and the lattice misfit between the two sub-layers [21, 149] are important for the superconducting function of these materials.

One of the interesting aspects of these materials is the competing spin density wave (SDW) and the superconductivity [46, 17, 124]. Indeed, the undoped compound REFeAsO is antiferromagnetically ordered (albeit a poor metal), and shows a structural phase transition [44, 56, 17, 124, 11]. With doping, the system gets superconducting and the structural transition as well as the SDW transition disappears [38, 121, 122, 123]. In addition, while the maximum T_C of the doped system increases with reducing the rare-earth ion size [121, 122, 123], the structural transition temperature decreases for the undoped system [44, 56, 17, 98]. These observations show interesting interplay between structure, magnetism and superconductivity with the chemical pressure and structural topology being important parameters. It is known that a mere knowledge of the long-range ordered structure is generally insufficient to describe electronic functions of a system with interplaying electronic degrees of freedom. Indeed, this has

been shown for transition metal oxides in which the electronic functions like superconductivity, colossal magneto-resistance and metal insulator transitions are related with interplaying charge, spin and lattice degrees of freedom [125]. Therefore, a detailed knowledge of the atomic structure for the REOFeAs oxypnictides could be a timely feedback to the theoretical models for correlating structure, magnetism and superconductivity in these materials.

In this chapter we present the local structural studies on the REFeAsO compounds as a function of rare-earth size, charge density and temperature by X-ray spectroscopy.
X-ray absorption is a fast ($\sim 10^{-15}s$) and site selective method, that investigate the short/medium range order and electronic structure of materials [139]. Extended X-ray absorption fine structure (EXAFS) provides informations on the local atomic distribution around a selected absorbing atom through photoelectron scattering [15]; on the other hand, X-ray absorption near-edge structure (XANES) spectroscopy probes the distribution of the valence electrons in the final states and the local geometry around the selected atom.

In the first section, the local structure of REFeAsO (RE = La, Pr, Nd and Sm) system has been studied as a function of rare-earth size. We have performed our measurements on polycristalline samples at low temperature, in fluorescence and trasmission mode. We have adressed our attention to the FeAs slabs, identified as the electronically active layer, because the knowledge of the local atomic distribution around the Fe atom is fundamental to provide informations on the atomic correlations. Fe K-edge EXAFS measurements has permitted to compare systematically the inter-atomic distances and their mean square relative displacements (MSRD) [16]. We find that the Fe-As bond length and the corresponding MSRD hardly show any change, suggesting the strongly covalent nature of this bond, while the Fe-Fe and Fe-Re bond lengths decrease with decreasing rare-earth size. As K-edge X-ray absorption near-edge structure (XANES) spectroscopy has been used to investigate the local geometry around the pnictogen site in the REFeAsO oxypnictides, combined with full multiple-scattering calculations to understand different XANES features [20]. The As K-edge XANES spectrum for the LaFeAsO is found to be significantly different from the other oxypnictides. The disordering seems significant in the SmFeAsO system due to a higher vertical position of the As atoms and a smaller misfit strain [21]. Since the vertical position of the As atom changes systematically with the rare earth size, this have a direct influence on the local geometry of the REO slabs. Therefore, we have studied the changes in the local geometry of the REO slabs due to different rare-earth size [18]. RE L_3-

XANES is an ideal tool to study the local geometry around the RE and has often been applied to study rare earth containing materials [131, 132]. While the L_3 white lines, corresponding to the $2p_{3/2} \rightarrow 5d$ direct transition, hardly show any change across the tetragonal to orthorhombic structural phase transition temperature, above the WL a systematic changes are observed, due to the varying local geometry with the rare earth size. The XANES spectra have been also simulated by full multiple scattering calculations to describe the different experimental features and their evolution with the RE size [19]. The near edge feature just above the L_3 WL is found to be sensitive to the ordering/disordering of oxygen atoms in the REO layers. In addition, shape resonance peaks due to As and O scattering change systematically, indicating local structural changes in the FeAs slabs and the REO spacers due to RE size.

In the second section, the local structure of $NdFeAsO_{1-x}F_x$ (x = 0.0, 0.05, 0.06, 0.15 and 0.18) system has been studied as a function of fluorine doping and temperature [22]. We have performed our measurements on polycristalline samples in trasmission mode. Arsenic K-edge EXAFS as a function of temperature has been used to retrieve direct information on the Fe-As bond lengths in superconducting (x=0.15 and 0.18) and non-superconducting (x=0.0 and 0.05) samples. These results indicate that there exist distinct lattice dynamics in the superconducting and non-superconducting systems, albeit the differences are smaller [22], compared with cuprates. The Nd L_3-XANES spectra at low temperature for superconducting (x=0.06) and non-superconducting (x=0) samples show small differences. It is possible that the F-substitution in the NdFeAsO causes reduced hybridization between the Nd *5d* and admixed *4f* orbitals, similar to the *4f*-superconductors [168], in which the superconductivity gets suppressed with increased hybridization.

The chapter is organized as follow: for each section we report first the experimental details, then we present the obtained results and finally we them discuss.

3.1 Effect of rare-earth substitution in REFeAsO

In this section we explore the local structure of REFeAsO with varying rare-earth size (RE =La (1.16Å), Pr (1.13Å), Nd (1.11Å), Sm(1.08Å)).

X-ray absorption measurements were performed on powder samples of REFeAsO (RE =La, Pr, Nd, Sm) prepared using solid-state reaction method [13]. Prior to the absorption measurements, the samples were characterized for the phase purity and the average structure by X-ray diffraction measurements [21]. The X-ray absorption measurements were made at different beamlines:

- *Fe K-edge EXAFS measurements*: **BM29** beamline of the European Synchrotron Radiation Facility (ESRF), Grenoble, where the synchrotron radiation emitted by a bending magnet source at the 6 GeV ESRF storage ring was monochromatized using a double crystal Si(311) monochromator. The Fe Kα fluorescence yield was collected using a multi-element Ge detector array. Simultaneous transmission signal was measured to make sure the observed signal to represent true X-ray absorption, however, it was not possible to obtain absorption signal in transmission mode without a contribution of the rare-earth L_1-edge (6.267 KeV, 6.835 KeV, 7.126 KeV and 7.737 KeV, respectively for the La, Pr, Nd and Sm with respect to the Fe K-edge at 7.112 KeV) and hence the choice was to opt for the partial absorption signal measured by fluorescence detection for a systematic comparison. The samples were mounted in a continuous flow He cryostat to perform the measurements at low temperature (40 K). The sample temperature was controlled and monitored within an accuracy of ±1K. Standard procedure was used to extract the EXAFS signal from the absorption spectrum, followed by the X-ray fluorescence self-absorption correction before the analysis.

- *RE L_3-edge XANES measurements*: **XAFS** beamline of the Elettra Synchrotron Radiation Facility, Trieste, where the synchrotron radiation emitted by a bending magnet source was monochromatized using a double crystal Si(111) monochromator. The L_3-XANES measurements were made at two temperatures (room temperature and 80 K) in the transmission mode using three ionization chambers mounted in series for simultaneous measurements on the sample and a reference. For the low temperature measurements, the samples were mounted on a liquid nitrogen cryostat cold finger enclosed in an Al shroud

with a Be window. The sample temperature was measured to be 80±1 K for the low temperature measurements.

- *Arsenic K-edge XAFS measurements*: **XAFS** beamline of the Elettra Synchrotron Radiation Facility, Trieste, where the synchrotron radiation emitted by a bending magnet source was monochromatized using a double-crystal Si(111) monochromator. The transmission mode (at 80 K) was used for the measurements using three ionization chambers mounted in series for the simultaneous measurements on the sample and a reference.

As a routine experimental approach, several absorption scans were collected to ensure the reproducibility of the spectra, in addition to the high signal to noise ratio [131, 132].

3.1.1 Fe K-edge EXAFS study

The Fe K-edge Extended X-ray Absorption Spectroscopy Fine Structure (EXAFS) measurements are made on different REFeAsO powder samples at low temperature (40 K). The results provide important informations about the local atomic distribution around the Fe atom and the correlation between the Fe atom and nearest neighboring [16].

Figure 3.1.1.1 shows Fe K-edge EXAFS oscillations of REFeAsO samples extracted from the X-ray absorption spectra measured on the powder samples. The EXAFS oscillations are weighted by k^2, to highlight the higher k-region due to scattering with heavier atom. There are evident differences between the EXAFS oscillations due to differing local structure of REOFeAs with different RE atom (see, e.g., the oscillation around k = 6–8Å^{-1}and in the k range above 10–14Å^{-1}).

The differences in the local structure could be better appreciated in the Fourier transforms of the EXAFS oscillations providing real space information. Figure 3.1.1.2 shows magnitude of the Fourier transforms, $|FT(k^2\chi(k))|$. The Fourier transforms are not corrected for the phase shifts due to the photoelectron back-scattering and represent raw data. The main peak at $\sim$ 2.4Å is due to Fe-As (4 As atoms at a distance $\sim$ 2.4Å) and Fe-Fe (4 Fe atoms at a distance $\sim$ 2.8Å) bond lengths, while the peak at $\sim$ 3.6Å corresponds to the Fe-RE bond length (4 RE atoms at a distance $\sim$ 3.72Å).While the main Fourier transform peak at $\sim$ 2.4Å appears to shift towards higher R-values, the Fe-RE peak seems to appear with a decreased amplitude with decreasing rare-earth size. The evident shift of the main peak is due to the increased amplitude of the Fe-

Fe scattering derived by the decreased Fe-Fe bond length and corresponding MSRD (discussed later).

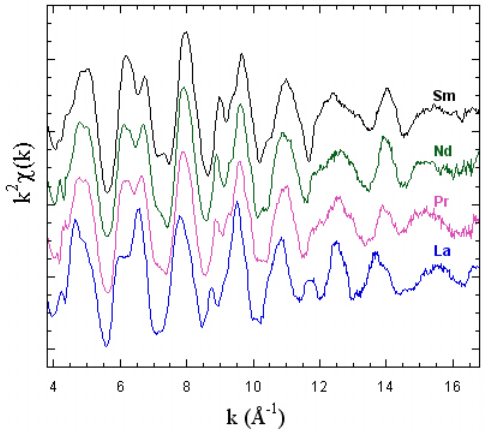

Fig. 3.1.1.1 *EXAFS oscillations (multiplied by k^2) extracted from the Fe K-edge absorption spectra measured on REOFeAs system (RE=La, Pr, Nd, Sm) at low temperature (40 K) and corrected for the fluorescence self-absorption effect [16].*

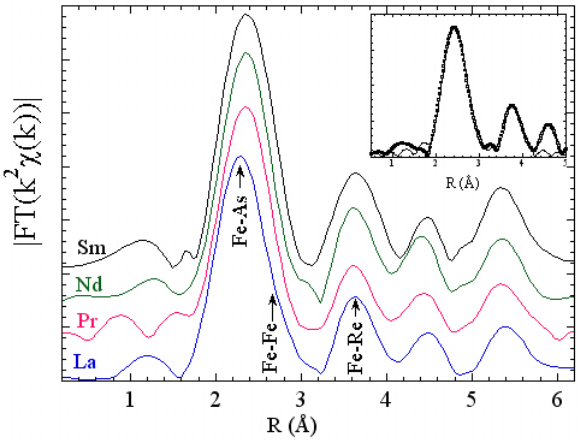

Fig. 3.1.1.2 *Fourier transforms of the Fe K-edge EXAFS oscillations showing partial atomic distribution around the Fe in the REOFeAs system. The Fourier transforms are performed between $k_{min} = 3\AA^{-1}$ and $k_{max} = 14\AA^{-1}$ using a gaussian window. The peak positions do not represent the real distances shows a phase corrected Fourier transform (symbols) (for the LaO-FeAs) with a fit over three shells, i.e., Fe-As, Fe-Fe and Fe-RE [16].*

We have used conventional procedure to analyze the EXAFS signal [15] due to three shells, i.e., Fe-As, Fe-Fe and Fe-RE scatterings. Except the radial distances R_i and the corresponding DW factors σ_i^2 , all other parameters were kept fixed in the least squares fit (intrinsic anelastic effects contribution $S_0^2 = 1$). The EXCURVE9.275 code was used for the model fit with calculated backscattering amplitudes and phase shift functions [126]. The number of independent data points, $N_{ind} \sim (2\Delta k \Delta R)/\pi$ [15] was 16 for the present analysis ($\Delta k = 11\text{Å}^{-1}(k = 3\text{–}14\text{Å}^{-1})$ and $\Delta R = 2.5\text{Å}$). Starting parameters were taken from the diffraction studies [44, 56, 98, 124, 21, 127]. A representative three shell model fit is shown with experimental Fourier transform as inset to Fig. 3.1.1.2.

The average radial distances as a function of rare-earth atom are shown in Fig. 3.1.1.3. There is a gradual decrease of the average Fe-Fe and Fe-RE distances (two upper panels) with decreasing rare-earth size, consistent with the diffraction studies showing decreasing lattice parameters (the a-axis and c-axis as a function of the rare-earth atom are shown as insets) [127]. On the other hand, the Fe-As distance (lower middle panel) does not show any appreciable change with the rare-earth atom size, revealing strongly covalent nature of this bond.
Within experimental uncertainties this appears to be consistent with the diffraction results [11, 44, 56, 17, 98, 124]. Using the bond lengths measured by EXAFS, we can determine directly the opening angle at the top of the $FeAs_4$ tetrahedron (Fe-As-Fe angle ϑ_3), considered to be the key to the superconductivity in these materials [17]. The Fe-As-Fe angle ϑ_3 has been calculated using the formula $\vartheta_3 = \pi/2cos^{-1}(d_{Fe-Fe}/\sqrt{2}d_{Fe-As})$. The Fe-As-Fe angle ϑ_3 is shown in Fig. 3.1.1.3. The Fe-As-Fe angle ϑ_3 is consistent with the earlier studies, revealing perfect $FeAs_4$ tetrahedron [11, 17] for the SmOFeAs.

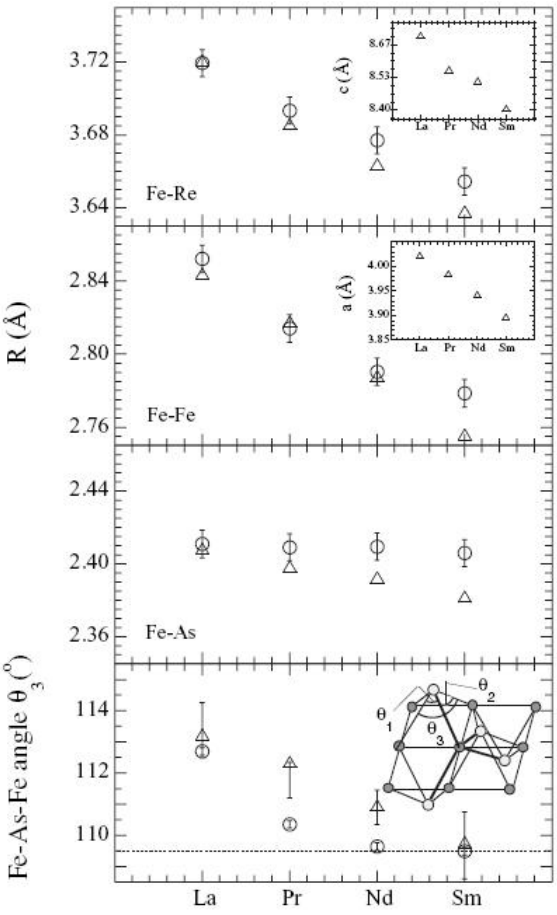

Fig. 3.1.1.3 *Fe-As (lower middle panel), Fe-Fe (upper middle panel) and Fe-RE (upper panel) distances at 40K as a function of rare-earth atom. While the Fe-As bond lengths hardly show any change, the Fe-Fe and Fe-RE bonds change with rareearth size. The insets (two upper panels) show shrinkage of the lattice parameters with the decreasing rare-earth size [21,127]. The bond lengths derived from the diffraction are included in the three panels for the comparison. Error bars represent the average uncertainties estimated by creating correlation maps. The Fe-As-Fe angle θ_3 determined using the EXAFS data (circles) is also shown (lower panel) with the dotted line at $\theta_3 = 109.5°$ corresponding to a perfect tetrahedron. The θ_3 determined from the diffraction data is shown for comparison (triangles). The vertical bars in the lower panel represent the span of the θ_3 measured by diffraction experiments on the REOFeAs [11,17,21,127]. The inset shows the cartoon picture of Fe-As-Fe angle θ_3, between the two non-adiacent Fe atoms and the As anion [11,17].*

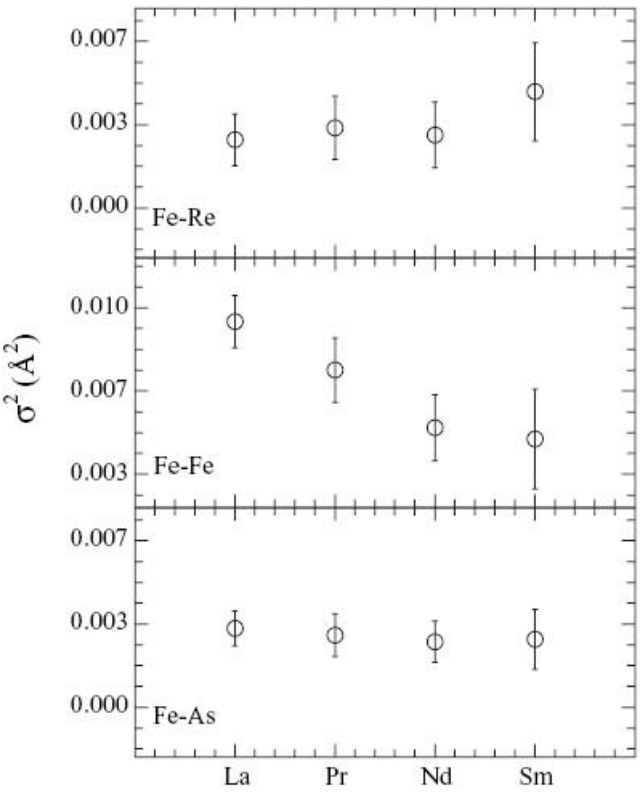

Fig. 3.1.1.4 *Mean square relative displacements (MSRD) of the Fe-As (lower panel), Fe-Fe (middle panel) and Fe-RE (upper panel) pairs at 40K as a function of rare-earth size. As the bond length (Fig. 3.1.1.3), the MSRD of Fe-As hardly shows any change indicating strongly covalent nature of this bond. On the other hand, the MSRD of Fe-Fe shows a decrease while that of the Fe-RE tending to increase from LaOFeAs to SmOFeAs.*

Figure 3.1.1.4 shows the correlated DW factors as a function of rare-earth atoms measuring the MSRD of different bond lengths. The MSRD of the Fe-Fe (middle panel) and Fe-RE pairs (upper panel) appear to depend on the rare-earth size, while we could hardly see any change in that of the Fe-As pairs indicating again the stiffness of the latter. The MSRD of the Fe-Fe shows a clear decrease with decreasing rare-earth size, as the Fe-Fe bond length (Fig. 3.1.1.3). Incidentally, the MSRD of the Fe-RE appears to show a small increase with decreasing rare-earth size, albeit the change is smaller than that of the Fe-Fe bond length (upper panel). Recently Tyson et al. [128] have reported temperature dependence of Fe-As MSRD for the doped and the undoped LaOFeAs, showing that, while the Einstein frequency of the Fe-As mode does

not change with doping, there is a small decrease of static contribution to the MSRD. The results of Tyson et al. [128] are consistent with strongly covalent nature of the Fe-As bond. On the other hand, the same authors have shown increased Einstein frequency with doping for the Fe-Fe pair, indicating enhanced Fe-Fe correlations. In summary, we have measured the local structure of REOFeAs with variable rare-earth ion (RE) revealing highly covalent nature of the Fe-As bond. In addition, the Fe-Fe and Fe-RE local atomic correlations show a systematic change with the rare-earth ion size, evidenced by MSRD of the respective bond lengths. Considering the conventional superconductivity mechanism in the strong coupling limit [129, 130], the electron-phonon interaction parameter is inversely proportional to the phonon frequency, i.e., proportional to the MSRD (the zero-point motion dominates at low temperature and hence $\sigma^2 \approx \hbar/2\omega_E m_r$, where m_r is the reduced mass and ω_E is the Einstein frequency of the pair). Since the T_C of the REOFeAs (if doped) increases with decreasing rare-earth size, it is reasonable to think that the Fe-Fe phonon modes may not have a direct role in the superconductivity (Fe-Fe MSRD decrease with decreasing rare-earth size). In contrast, the Fe-RE MSRD tends to show a small increase (or remains constant) with decreasing rare-earth size, and may be somehow contributing to the superconductivity, however, more experiments are needed to address this issue. Although, it is difficult to quantify the role of the local electron-phonon coupling in the correlating magnetism and superconductivity, the presented results certainly provide timely experimental information on the local atomic fluctuations, that could be important feedback for new models to describe fundamental properties of the REOFeAs with doping and chemical pressure.

3.1.2 RE $L_3 - edge$ x-ray absorption study

RE L_3-edge XANES spectroscopy is a direct probe of the local structure around the RE atom and the distribution of the valence electrons with the final states in the continuum being due to multiple scattering resonances of the photoelectron in a finite cluster [15], is an ideal tool to study local geometry around the RE and has often been applied to study RE containing materials [131, 132, 133].

Our results about RE L_3-edge XANES spectroscopy provide direct information on the local structure around the RE atom and clarify the role of the REO layer and its interaction with the FeAs layers in the REFeAsO (RE = La, Pr, Nd and Sm) oxypnictides [18, 19]. The multiple

scattering theory has been employed to identify the nature of the different features and their evolution as a function of RE size [18].

3.1.2.1 *RE L_3-edge x-ray absorption measurements: results and discussion*

Figure 3.1.2.1 shows normalized RE-L_3 spectra of REFeAsO (RE= La, Pr, Nd and Sm) measured at room temperature showing an intense peak, the characteristic white line (WL) of RE^{3+}. Here, the zero of the energy scale is fixed to the WL peak position for a proper comparison between the different spectra. It is worth recalling that the L_3 absorption process is a $2p_{3/2} \rightarrow 5d\, or\, 2p_{3/2} \rightarrow 6s$) transition governed by the dipole selection rules ($l = \pm 1$) and hence empty states with d or s symmetries (and admixed states) can be reached in the final state. Since the probability for a $2p_{3/2} \rightarrow 6s$ transition is about two orders of magnitude lower than for a $2p_{3/2} \rightarrow 5d$ transition, the earlier can be ignored for describing the L_3 WL.

The one-electron picture (i.e., all the orbitals not directly involved in the absorption process are passive in the final state) works well for the L_3 WL unless the materials of interest are mixed valent systems. In the present case, the WL appears to be a typical of RE^{3+} and hence the one-electron picture could be fairly used to describe the spectra. In addition to the intense WL, we can see different near-edge features, a weak structure around 15 eV above the WL (feature A), and the continuum resonances appearing as a two peak structure (the broad features denoted by B1 and B2 appearing respectively around 35 and around 50 eV) due to the photoelectron scattering with the nearest neighbors. The RE atoms have 4 near neighbors O sitting at a distance $\approx$ 2.3Å and 4 As atoms occupying a site at $\approx$ 3.3Å , and hence the two peak structure of the continuum resonance is expected with the low and high energy peaks due to As and O scattering respectively. The energy separation between the two is consistent with the $E \propto d^{-2}$ relation for a continuum resonance [134]. Here it is worth referring to Ignatov et al [135] reporting the La L_3-XANES on LaFeAsO with a typical La^{3+} WL and the continuum peak, however, with a limited discussion they have incorrectly assigned the continuum resonance peak B1 to the La-O distance. The feature A is very weak or absent for the La and Pr L_3-XANES while clearly visible for the Nd and Sm L_3 cases (see e.g., the inset). The feature A has been frequently observed in the L_3-XANES of the rare earths and discussed as being due to a particular local structural geometry of the RE [136]. Here the feature A is found to be absent (or very weak) in the La and Pr L_3 spectra while clearly seen in the Nd and Sm L_3 edges. The

feature A is found to appear at the same energy. Indeed, the observation is consistent with the earlier results [136, 137], albeit with a dubious interpretation relating it to the local structure. The continuum resonance peaks B1 and B2 show a systematic change with the rare earth ion size (see e.g. the inset) indicating a clear evolution of the local geometry around the RE. Peaks B1 and B2 shift towards higher energy due to decreasing RE-As and RE-O distances with decreased rare earth size, consistent with the $E \propto d^{-2}$ empirical rule [134]. It is interesting to note that neither the WL nor the XANES features show any appreciable change across the tetragonal to orthorhombic structural transition temperature (dotted and solid lines in Fig. 3.1.2.1).

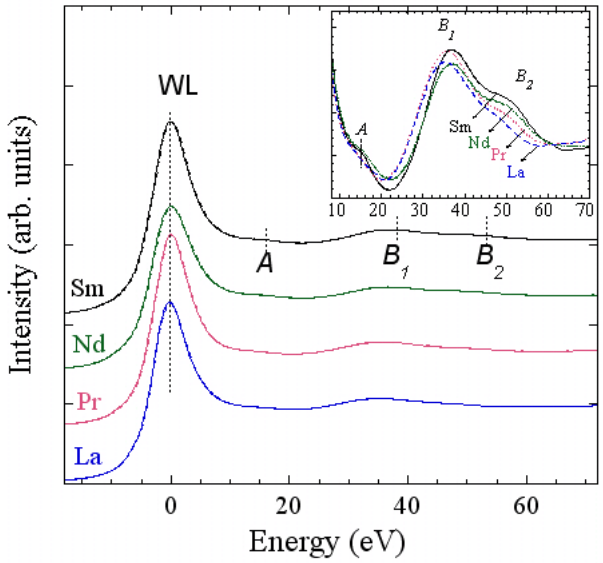

Fig. 3.1.2.1 *The near-edge regions of the normalized RE L_3-edge absorption spectra of the REFeAsO at 80 K and room temperature (solid and dotted lines, respectively). The zero of the energy scale is fixed to the characteristic WL representing $2p_{3/2} \rightarrow 5d$ transitions. Other near-edge features are assigned as A, B1 and B2, showing a change of local geometry with changing rare earth. The inset shows a zoom over the near-edge features A, B1 and B2 (room temperature).*

It is interesting to note that neither the WL nor the XANES features show any appreciable change across the tetragonal to orthorhombic structural transition temperature (dotted and solid lines in Fig. 3.1.2.1). Therefore, while the average symmetry measured by diffraction (long range ordered structure) changes, the local atomic structure measured by the XANES hardly show any change except a thermal shrinkage of the lattice (Fig. 3.1.2.2). On the other hand, the negligible change in the WL intensity suggests that the electronic structure of the unoccupied

RE d-states (and admixed electronic states) remains the same in the two structural phases. This observation is consistent with the Fe K-edge XANES [138] study revealing hardly any change in the local structure across the structural phase transition in these materials. However, the Fe K-edge study has revealed a clear change in the $1s \rightarrow 3d$ quadrupole transition (albeit small) across the structural phase transition. Thus, it is possible that the tetragonal-to-orthorhombic structure phase transition is being induced by the electronic part, due to the fact that the electronic sates near the Fermi surface are mainly of Fe *3d* nature. However, more work is necessary to discuss the structural phase transition versus local structure by XANES, enhanced by polarized data.

Figure 3.1.2.2 shows energy positions of the peak B1 with respect to the WL at two temperatures, showing a continuous increase with decreasing rare earth size due to the decreased RE-As distance. The ΔE at low temperature is slightly higher by almost the same amount, suggesting an average but similar unit cell shrinkage for all the samples on lowering the temperature. We have also plotted the crystallographic RE-As distance at room temperature for comparison (lower panel). The inset displays the ΔE as a function d^{-2}, showing the expected linear behavior [134]. To get further information from the L_3-XANES, we have extracted the line shape parameters for the WL as well as the peaks B1 and B2. In the one-electron approximation the L_3-XANES WL could be deconvoluted by a Lorentzian (core hole life time), convoluted by the experimental broadening providing the *5d* (and admixed) density of empty states weighted by the matrix element and the arctan curve to take into account the transition into the continuum. The energy positions are similar to those which have been obtained from the second derivative of the spectra (Fig. 3.1.2.2).

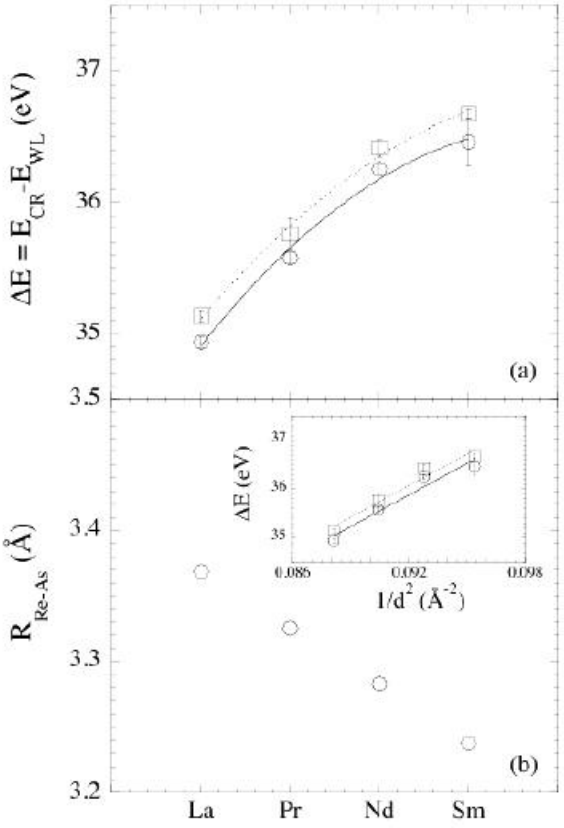

Fig. 3.1.2.2 *Energy separation $\Delta(E)$ between the white line and the continuum resonance peak B1 at room temperature (open circles) and at 80 K (open squares), showing a continuous increase with decreasing rare earth size due to decreased RE-As distance (a). The energy positions are determined from the second derivative of the L_3 XANES. The crystallographic RE-As distance at room temperature is also shown for comparison (b). As expected, a linear relation is observed between the ΔE and d^{-2} (see the inset in (b)). The error bars represent the standard deviation estimated using different experimental scans.*

All efforts were made to take care of experimental aspects influencing the L_3-line shapes (thickness and homogeneity of the samples), however, it is not correct to consider equal transition matrix elements for all the rare earths, therefore the absolute intensities can not be compared quantitatively as a function of the RE. Moreover, the absolute intensity of the WL does not show any appreciable or systematic change with the rare earth. On the other hand, the intensities of the continuum resonance peaks B1 and B2, probing the local geometry around the rare earth atom, change systematically. The relative change in the intensity of peaks B1 and B2,

defined as $I = [I(B1) - I(B2)]/[I(B1) + I(B2)]$, is displayed in Fig. 3.1.2.3 as a function of rare earth, showing a decrease with decreasing rare earth size, revealing a systematic change of local geometry around the RE involving the As and O atoms (peak B1 is due to the RE-As distance while peak B2 is due to the RE-O distance).

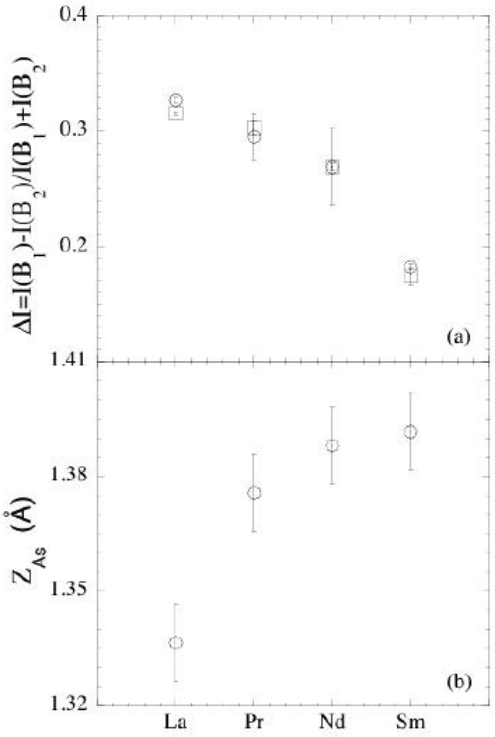

Fig. 3.1.2.3 *Difference of relative intensities of the continuum resonances B1 and B2 as a function of rare earth (a). The vertical position of the As atom with respect to the Fe-Fe plane, measured by the Fe K-edge EXAFS [16], is also shown (b).*

Since the RE-As represents out-of-plane atomic correlation while the RE-O describes in-plane correlation, the decreasing I should reflect the increased correlation between the RE-O layer and the Fe-As layer (i.e., increased interlayer coupling) with decreasing rare earth size. Although it is difficult to quantify the atomic displacement pattern around the RE, the results seems to be consistent with the higher perpendicular position of the As atom with respect to the Fe-Fe plane (Fig. 3.1.2.3(b)) and the decreased RE-As distance (Fig. 3.1.2.2(b)) with decreasing rare earth size.In summary, we have studied the RE L_3-XANES of the oxypnictides REFeAsO with variable rare earth ions to explore the valence electronic structure as well as the local geometry of the RE-O slab. While the L_3 white lines hardly show any change across the tetragonal to

orthorhombic structural phase transition temperature, a clear change is observed in the spectral weight with the electron doping. In addition, the XANES features above the WL show a systematic change due to the varying local geometry with the rare earth size. The energy separation between the WL and the continuum resonances change consistently with a change of RE-As and RE-O distance, due to changing misfit between the FeAs and REO sub-layers. A systematic change of the relative intensities of the continuum resonance features is also observed. Since the vertical position of the As atom changes systematically with the rare earth size (the As atom moves away from the Fe–Fe plane due to the decreased Fe-As-Fe angle with decreasing rare earth size [16]), this has a direct influence on the local geometry of the REO slabs, as demonstrated by the XANES spectra. The results suggest that the interlayer coupling between the Fe-As and the spacer (REO) layer may also play a role in the superconductivity mechanism of the REO-FeAs. Thus, the outcome of this experiment recalls the recent debate on the misfit strain [139] and out-of-plane disorder controlled superconductivity in copper oxide high T_c superconductors [133], bringing the two families onto the same platform for discussion. Although it is difficult to argue on the cause or consequence of the local structural changes and the quantitative role of intra and interlayer coupling in the correlating itinerant magnetism and superconductivity, the present results certainly add a new experimental feedback to understand the role of the structure and local chemistry in the fundamental properties of REFeAsO oxypnictides [18].

3.1.2.2 *Multiple scattering calculations: results and discussion*

In order to better understand the electronic structure of the system, we have performed systematic simulations over the rare-earth L_3 edges, using self-consistent real-space multiple scattering by the FEFF8.2 code [140, 141] within the muffin-tin approximation. The atomic potential is calculated self-consistently using a cluster of up to 127 atoms within a radius of 8.0Å. The multiple scattering calculation converges when a cluster of 13 shells (59 atoms up to 6.15Å) is considered. For the calculations, the energy and position dependent Hedin-Lundqvist optical potential [142] has been selected as the exchange–correlation potential. The total electronic potential was constructed by spherically averaging the muffin-tin potentials on each atom and keeping constant the potential in the interstitial region between the muffin-tin spheres. The f states for all the rare-earth metals were kept in a frozen state to achieve convergence of the self-consistent potentials ($l_{max} = 3$). Once f states were allowed to be involved, the calculations

showed a shift of 1 eV towards lower energy.

Figure 3.1.2.4 shows experimental rare-earth L_3-edge XANES spectra measured at room temperature on a series of REFeAsO (RE = La, Pr, Nd and Sm) samples. In the figure one can identify four distinct features; the white line feature A reflects directly the transition from core p electrons to partial empty d states, while features C and D originate from multiple scattering contributions, the so called shape resonances. Feature B has different intensity for different RE systems and appears to be related to the electronic structure. The white line intensities hardly show any systematic change with the RE size, while features C and D change systematically due to changing bond lengths [18]. It should be mentioned that a direct comparison of the white line intensities is impossible unless complete information on the transition matrix element is available in addition to the experimental artifacts. On the other hand, the relative variation of peaks C and D appears to follow the vertical position of the As atoms with respect to the Fe-Fe plane [16, 18], controlling the superconductivity (while the system is doped) and magnetic moment (undoped) of these materials. In addition, the weak feature B also appears to show a systematic change with varying rare-earth size. It should be recalled that a similar feature B has been seen in the L_3-edge XANES measured on cuprates, however, discussed in the past with a dubious interpretation based on two types of structural symmetries [136, 137]. Since the average structural symmetry of the REFeAsO does not change with the RE, it is possible that feature B is due to the electronic structure and/or due to a local disorder in the REO layers. Moreover, the intensity of this feature appears to scale with the superconducting transition temperature (while the system is doped), and hence it should be interesting to address feature B in detail.

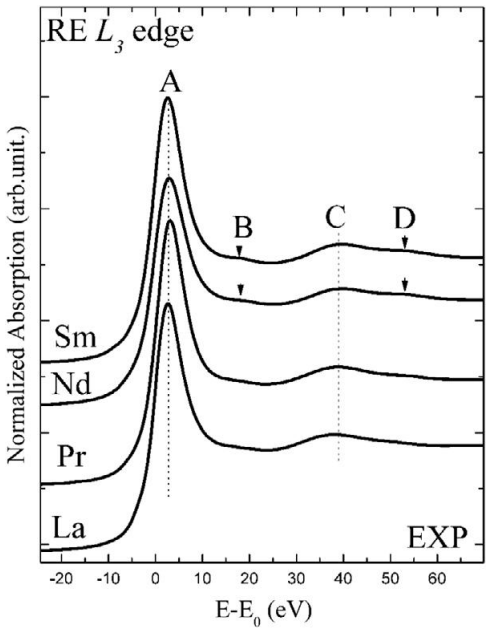

Fig. 3.1.2.4 *RE L_3-edge X-Ray absorption aear adge spectra of REFeAsO (RE=La, Pr, Nd, Sm)[18]. In the near edge region, up to ∼60 eV above the edge, all spectra shows four features. As the ionic radii increases, feature B gets more pronounced. The zero of the energy scale is fixed to the first derivative of the L_3-edge, as standard method to identify the absorption edge energy.*

Let us first discuss the electronic structure. The electronic configuration of La ($[Xe]5d^16s^2$) does not have any f electrons in the ground state, while the number of f electrons increases up to six in that of samarium, with the electronic configurations being $[Xe]4f^36s^2$, $[Xe]4f^46s^2$ and $[Xe]4f^66s^2$ for Pr, Nd and Sm, respectively. This suggests a non-negligible role for the *4f* electrons in the L_3-edge XANES spectra. Indeed, the ground state atomic configuration effect is negligible in most of the K edges, but can be significantly important in the L_3-edge of rare-earth metals, well recognized in the Ce L_3-edge of CeO_2 [143]. As a matter of fact, the one electron approach with muffin-tin approximation could reproduce reasonably well the RE L_3-edge XANES for all the rare-earth atoms in the REFeAsO, albeit with a clear disagreement for feature B. Indeed, the one electron calculations reveal a distinct feature B unlike the experimental spectra in which the feature appears damped (Fig. 3.1.2.5). Differences between the experimental and theoretical spectra could be due to the convolution function accounting for the intrinsic core-hole lifetime, and the extrinsic experimental resolution can be ruled out since

the L_3-edge energies for all the RE lies within an energy interval of about 1500 eV.

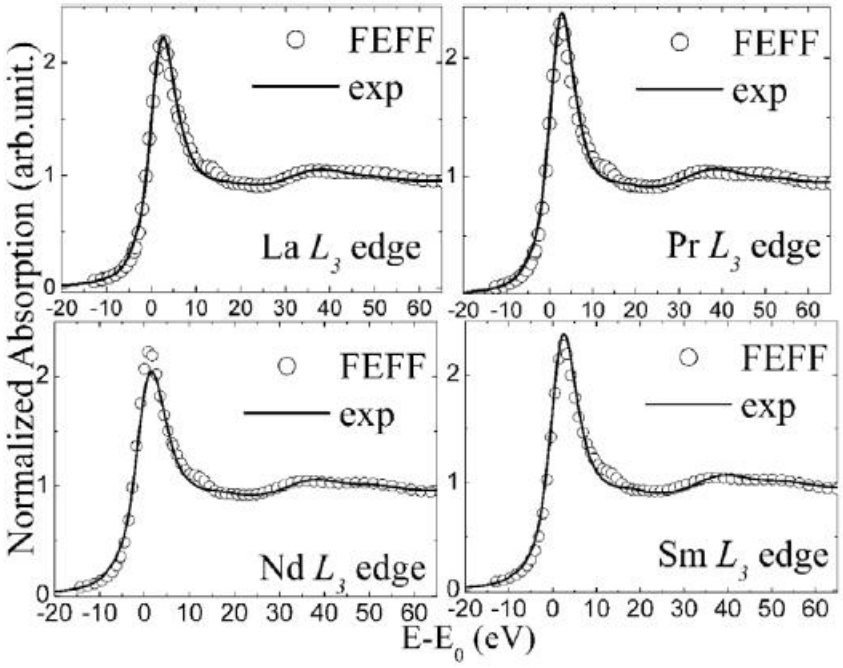

Fig. 3.1.2.5 *FEFF calculations (open circles) of the L_3-edge for the REFeAsO (RE=La, Pr, Nd, Sm) system compared with the experimental spectra (solid lines).*

In addition, there appears a small discrepancy in the peak position of feature B. The fact that we have used average crystallographic ordered structural parameters for the calculations makes it difficult to expect a perfect match of the energy position, since local structure disorder and defects can easily change the energy position. To have further insight, it is useful to compare the density of states (DOS) calculations illustrating the electronic structure of the system.

Figure 3.1.2.6 shows the DOS projected on the rare-earth atoms. We have used the ground state configuration for the calculations (no core hole), consistently with the one electron RE L_3-edge XANES (Fig. 3.1.2.5). The DOS shows that the near edge absorption intensity in the RE L_3-edge XANES spectra is mainly given by the transition from the *2p* to *5d* states. Near the Fermi level, most of the *4f* DOS of lanthanum are empty, while the *4f* DOS becomes increasingly occupied as the atomic number of the RE increases. Feature B in the L_3-edge XANES could probe the empty *4f* electron states, however, a direct transition from *2p* states to *4f* final states is not allowed. On the other hand, from the projected DOS on other atoms (e.g. Fe, As or O), shown in Figure 3.1.2.7, it appears that the iron empty p states mainly contribute to feature B.

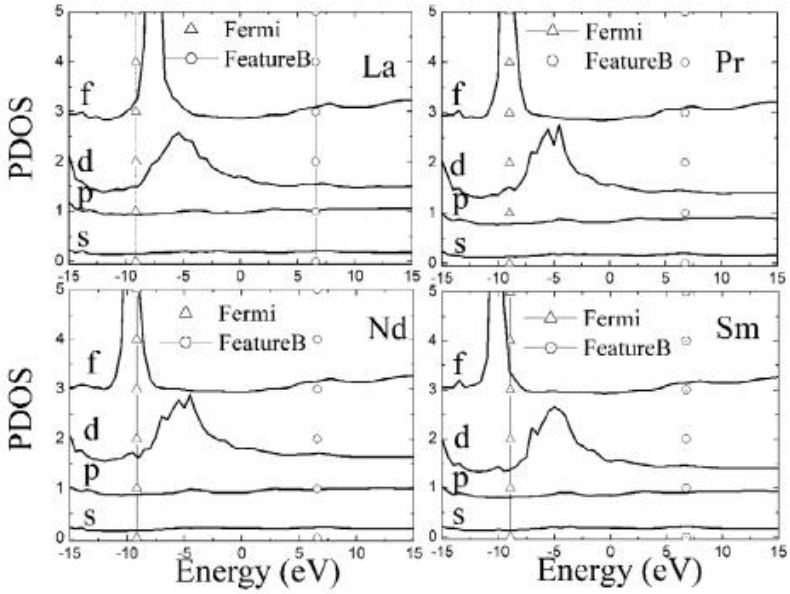

Fig. 3.1.2.6 *Projected electronic density of states on the central absorber RE metal atoms in the REFeAsO (RE=La, Pr, Nd and Sm) system. The triangles and circles are to guide energy positions of the Fermi level and the feature B, respectively.*

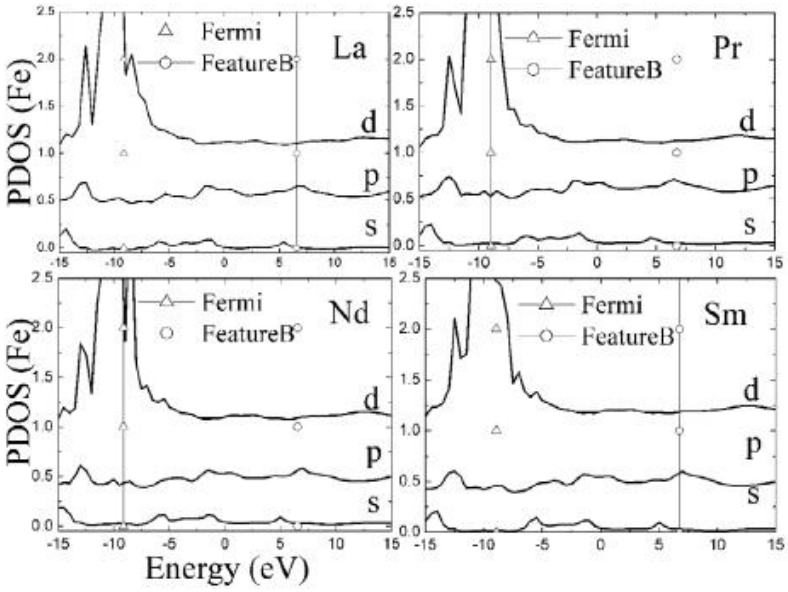

Fig. 3.1.2.7 *Projected electronic density of states on the iron atom in the REFeAsO (RE=La, Pr, Nd and Sm) system. The triangles and circles are to guide energy positions of the Fermi level and the feature B, respectively.*

Therefore feature B probes the hybridization of RE *4f* states and Fe *4p* states. Nevertheless, we should mention that the RE *4f* states and the Fe *4p* states do not vary significantly with changing RE with experimental observation, suggesting that the electronic structure alone may not be able to explain feature B, and that multiple scattering contributions should be taken into account.

Figure 3.1.2.8 shows RE L_3-edge XANES multiple scattering calculations for two representative REFeAsO (RE = La, Sm) systems with an increasing number of atomic shells around the absorbing atom. The atomic potential is calculated over a large cluster (∼8 Å) of atoms and fixed self-consistently. Details on different shells around the absorbing RE (La, Sm) atoms are provided in Table I with corresponding inter-atomic distances and coordination numbers. From multiple scattering calculations of the La and Sm L_3-edge, we can notice that feature B emerges and evolves in similar way for both La and Sm. The results of the calculations can be summarized as follows:

1. feature B emerges due to the constructive interference between multiple scattering waves when the cluster increases up to five shells with the addition of four RE (La or Sm) atoms in the same plane as the absorber;

2. intensity of feature B increases with the addition of two As atoms on the top and the bottom, with the feature getting sharper when eight oxygen atoms at a distance ~ 4.6Å are added in the REO slab. This suggests a significant role for the oxygen shell on feature B;

3. feature B disappears as the plane of eight iron atoms (see the 8th shell, at ~ 5.4Å) is included in the calculation. These iron and oxygen atoms of the 7th shell have the same x and y coordinates but are located on the lower side of the absorber. Since feature B disappears, the electron waves scattered by the iron plane (8th shell) and the oxygen plane (7th shell) should interfere destructively;

4. feature B reappears if more atomic shells are included, suggesting that it is associated to the layered structure. The fact that the peak intensities for La and Pr are much smaller, the oxygen layer with respect to the Fe plane should be less disordered in the LaFeAsO and PrFeAsO systems. However, multiple scattering contributions from atoms up to 6Å actively contribute to feature B.

In the high temperature cuprate superconductors, a similar feature appearing in the L_3-edges was intensively investigated [136, 137] and found to be related to the eightfold hexahedron-type coordination surrounding the absorber. The only difference between cuprates and the iron pnictides is that there is no CuO_2 like plane in the latter. Both the REO and FeAs layers are slabs (Fe and As are not in the same plane) rather than planes. Moreover, the calculated spectra show a strong intensity of feature B, for a significantly large cluster of atoms, regardless of type of the rare-earth absorber. However, in the experimental spectra, the intensity of feature B increases with increasing atomic number. On the basis of the electronic structure and the multiple scattering calculations, we argue that feature B should be due to; (a) the hybridization between the RE *4f* and Fe *4p* states, which increases with an increase in the number of *f* electrons, and; (b) the multiple scattering of iron and oxygen layers sandwiching the layer of rare-earth metals. The latter suggests that oxygen disorder may significantly affect the intensity of feature B, as observed in the experimental spectra. It is worth recalling that any change in the local symmetry could create a structure in the XANES, as shown in the Ni K edge of $PrNiO_3$ system [144].

Since relative disorder between the FeAs and REO blocks indicates changing local symmetry, the findings are not inconsistent. It is worth recalling that multiple electron excitations (MEE) could also produce a structure in the XANES spectrum. For example, a double excitation is identified in the Cu K edge x-ray absorption of cuprates [145], appearing around 85 eV above the 1s threshold, characterized by a simultaneous excitation of the *1s* and *3p* electrons into unoccupied states leaving two holes on the Cu site. Considering that feature B in the RE L_3-edge XANES appears around 15 eV above the threshold, in principle a double electron excitation could be associated to $O_2(5p_{1/2})$ and $O_3(5p_{3/2})$ transitions, since for the light RE (such as Ce, Pr, Nd, Sm etc) these transitions fall in the range of 15–22 eV [146]. However, as discussed in [146], the main contribution of double excitation in the RE L_3 edges comes from the $L_3N_{4,5}$ excitations, and other potential contributions are very weak. Therefore, we can rule out feature B being due to an MEE.

L_3 edge	La ($Z = 57$)	Pr ($Z = 59$)	Nd ($Z = 60$)	Sm ($Z = 62$)
T_c (K)[a]	25.9	43.2	50.9	52.8
Energy (eV)	5483	5964	6208	6716
1st shell	4O (2.35 Å)	4O (2.34 Å)	4O (2.29 Å)	4O (2.28 Å)
2nd shell	4As (3.37 Å)	4As (3.36 Å)	4As (3.28 Å)	4As (3.28 Å)
3rd shell	4Fe (3.72 Å)	4Pr (3.72 Å)	4Nd (3.64 Å)	4Sm (3.61 Å)
4th shell	4La (3.75 Å)	4Fe (3.74 Å)	4Fe (3.66 Å)	4Fe (3.68 Å)
5th shell	4La (4.02 Å)	4Pr (4.02 Å)	4Nd (3.94 Å)	4Sm (3.94 Å)
6th shell	As (4.25 Å, 4.45 Å)	As (4.20 Å, 4.50 Å)	As (4.08 Å, 4.44 Å)	As (4.02 Å, 4.50 Å)
7th shell	8O (4.66 Å)	8O (4.65 Å)	8O (4.56 Å)	8O (4.56 Å)
8th shell	8Fe (5.48 Å)	8Fe (5.49 Å)	8Fe (5.38 Å)	8Fe (5.40 Å)
9th shell	4La (5.69 Å)	4Pr (5.69 Å)	4Nd (5.58 Å)	4Sm (5.58 Å)
10th shell	4As (5.85 Å)	4As (5.81 Å)	4As (5.67 Å)	4As (5.63 Å)
11th shell	4Fe (5.93 Å)	4Fe (5.90Å)	4Fe (5.78 Å)	4Fe (5.75 Å)
12th shell	4As (6.0 Å)	4As (6.04 Å)	4As (5.94 Å)	4As (5.98 Å)
13th shell	4O (6.16 Å)	4O (6.15 Å)	4O (6.03 Å)	4O (6.03 Å)

Table I *The model cluster used for the simulations at the RE L_3-edgen in the REFeAsO (RE = La, Pr, Nd and Sm) system.* [a] *The maximum T_C while the system is doped.*

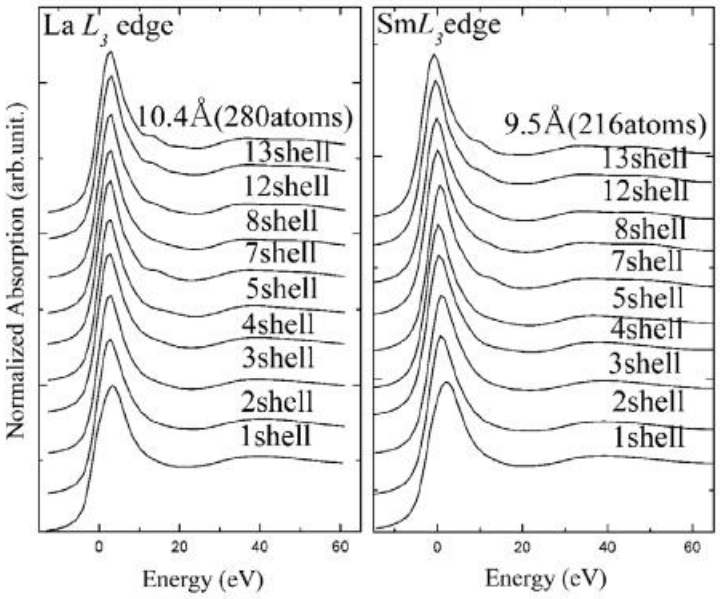

Fig. 4.1.2.8 *Multiple scattering calculations of the L_3-edge with varying shell size.*

Here, we should also underline that the misfit strain between the REO and the FeAs slabs could easily control the order/disorder of the oxygen, of which the mobility depends on the misfit strain. In SmFeAsO, the FeAs slabs are less strained, while the vertical position of the

As atoms is higher [16], with a high interlayer coupling and hence more disordered positions of O atoms. On the other hand, the vertical position of the As atoms is lower in the case of LaFeAsO and the intensity of feature B may be lowered due to a destructive multiple scattering interference derived from higher order in the REO slabs, unlike the case of SmFeAsO, in which is the disorder could increase the multiple scattering contributions. The results are consistent with the fact that feature B is sensitive to the doping, being more intense for F substitution (in place of O) [18], and hence increased (chemical) disorder in the REO slabs. It is interesting to compare the results with the crystallographic structural phase transition in the REFeAsO system. The structural phase transition from the tetragonal to the orthorhombic phase appears at 165 K, 155 K, 135 K and 130 K respectively for RE = La, Pr, Nd and Sm. This implies that a larger relative interlayer disorder reduces the structural phase transition temperature. This seems reasonable since local disorder can easily destroy the average symmetry. In summary, we have investigated RE L_3-edge XANES of the REFeAsO system. The L_3-edge shows a feature B (see Fig. 3.1.2.4) evolving from weak, for the lower Z lanthanide (La and Pr), to intense, for the higher Z lanthanides metal (e.g., Nd and Sm). From detailed DOS and multiple scattering calculations, we claim that this feature is not only related to the electronic configuration of the rare-earth metals, but also to multiple scattering contributions originating from the geometrically symmetric oxygen and iron positions. This suggests that the oxygen should be less disordered with respect to the Fe layer in LaFeAsO, while there is a significant oxygen disordering due to a higher interlayer coupling (higher vertical position of the As atoms) and a smaller misfit strain [147, 148, 149] in the SmFeAsO system. Since, once suitably doped, the superconducting transition temperature of SmFeAsO is higher than LaFeAsO, the present results suggest an intimate relation or an interplay between the superconductivity and disorder in the spacer layers, similar to the out-of-plane disorder controlled superconductivity addressed in the cuprate superconductors [133].

3.1.3 As K-edge EXAFS study

The As atom represent the link between the Fe plane and the REO slab, so As K-edge XAFS measurements are fundamental to clarify the role of disorder in the quaternary oxypnictide systems. The arsenic atom has only four Fe atoms as nearest neighbors, and their contributions to the arsenic K-edge EXAFS are well separated from all other shell contributions. This makes

the arsenic K-edge EXAFS data highly suitable for extracting quantitative information on the Fe-As bond lengths and the related MSRDs [150]. Moreover, the combination of As K-edge XANES spectra with the multiple scattering theory has been employed to identify the nature of the different features and their evolution as a function of RE size [18].The results confirm the highly covalent nature of the Fe-As bond and suggest that the oxygen order/disorder in the spacers should have an important role to play in the properties of oxypnictides [20].

3.1.3.1 *Multiple scattering calculations in the XANES region: results and discussion*

The electronic structure of the REFeAsO system has been reconstructed by systematic simulations over the As K-edges, using the self-consistent real-space multiple-scattering FEFF8.2 code [140, 141] within the muffin-tin approximation. The atomic potential is calculated self consistently using a cluster of up to 127 atoms within a radius of 8.0Å. The multiple-scattering calculation converges for a cluster of 180 atoms within the radius of 8.8Å. For the calculations, the energy and position dependent Hedin-Lundqvist optical potential [142] has been selected as the exchange-correlation potential. In order to account for the experimental resolution for the As K-edge, the real part of the Hedin-Lundqvist is shifted by 2 eV.

Figure 3.1.3.1 shows As K-edge XANES spectra measured at 80K on a series of REOFeAs (RE =La, Pr, Nd and Sm) samples. Apart from the one for the LaFeAsO, As K-edge of all the other REFeAsO (Pr, Nd and Sm) appear quite similar in spectral shape and peak positions. The shoulder structure A in all the REFeAsO is well aligned and the relative peak positions for feature B and C agree well, with a small change in that of feature D and E. Unlike the other REFeAsO, the LaFeAsO shows an additional distinct feature B', appearing between the shoulder feature A and the most intense feature B. Moreover, the intensity of the shoulder feature A in LaFeAsO shows an evident suppression. To understand the origin of spectral features and their evolution with RE in the REFeAsO (RE =La, Pr, Nd and Sm), we have performed one electron multiple-scattering calculations at the As K-edge.

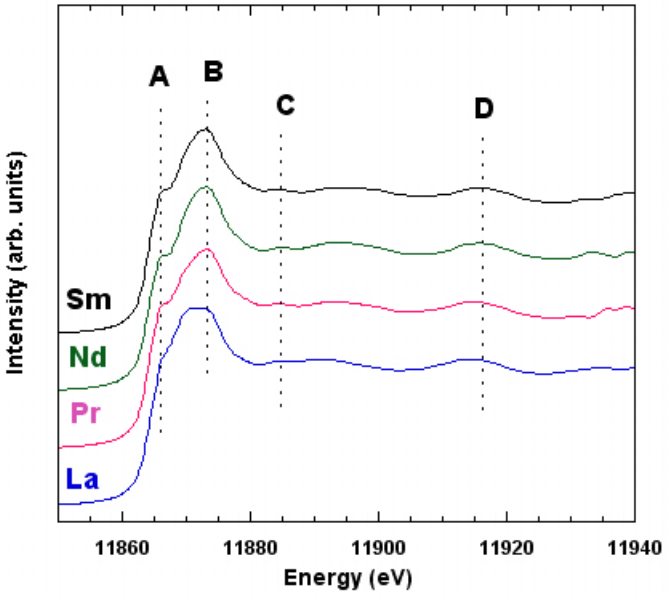

Fig. 3.1.3.1 *Arsenic K-edge X-ray absorption near-edge structure (XANES) of REFeAsO (RE=La, Pr, Nd and Sm), measured at 80 K. The XANES spectra show five different features (A, B, C, D, E) in the range of 60 eV above the edge except a new feature B', distinctly evident only for the LaFeAsO.*

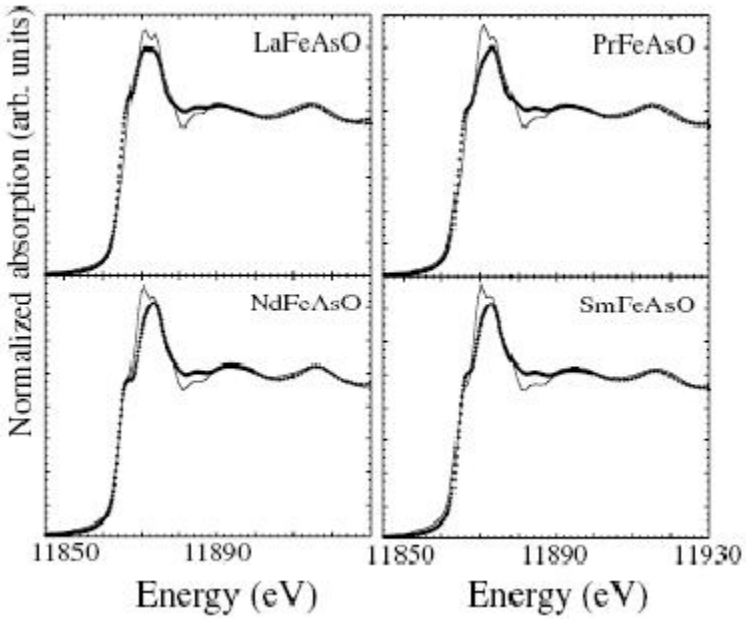

Fig. 3.1.3.2 *Theoretical calculation of the As K-edge spectra of REFeAsO (RE=La, Pr, Nd, Sm) using the FEFF8.2 code (solid curves) compared with the experimental data (symbols)[20].*

Figure 3.1.3.2 shows the calculated As K-edge XANES for the REFeAsO, campared with the corresponding experimental spectra. The calculations could reproduce most of the spectral features in the experimental data of LaFeAsO, with a clear disagreement with the spectra for the other REFeAsO, relative to the B'. The feature B' (Fig. 3.1.3.1) which appears in the theoretical spectra, is distinctly seen only in the LaFeAsO. Unlike the experimental spectra, the feature B in the calculated XANES seems to have similar relative intensity (with respect to feature A) for the REFeAsO except in the LaFeAsO in which the relative intensity appears lower. For a further understanding, we have calculated the As K-edge XANES for the REFeAsO system with increasing number of atomic shells around the As atom, clarifying the effect of local geometry on the spectral features. The atomic potential was kept constant to the one calculated self-consistently within a cluster of 8Å.

Figure 3.1.3.3 shows the multiple-scattering calculations for the representative LaFeAsO system with an increasing number of atomic shells around the absorbing Arsenic atom. The feature A emerges in the calculations for the first shell (4 Fe at 2.3Å) while the features B and C appear only with an increased cluster size up to 5.7Å (including 47 atoms). Interestingly, distant atoms from the absorber (greater than 7Å) has significant contribution to the feature B'. With increasing cluster size from 7Å (91 atoms) to 7.03Å (99 atoms) (by adding eight oxygen atoms in the La-O layer (5.5Å) above the As-Fe layer), the intensity of feature B increases significantly. This points out that feature B' should be directly correlated with the local geometry of the REO spacers. Therefore, an evident absence of this feature B' in the experimental spectra of REFeAsO (RE =Nd, Pr and Sm) could be due to local disordering of the oxygen with respect to the As site. This observation is consistent with the conclusion of our recent study on the rare-earth L_3-edge XANES of the REFeAsO system suggesting order/disorder in the spacer layer being important for the superconductivity of the REFeAsO system [18, 19]. We will come back to discuss this later.

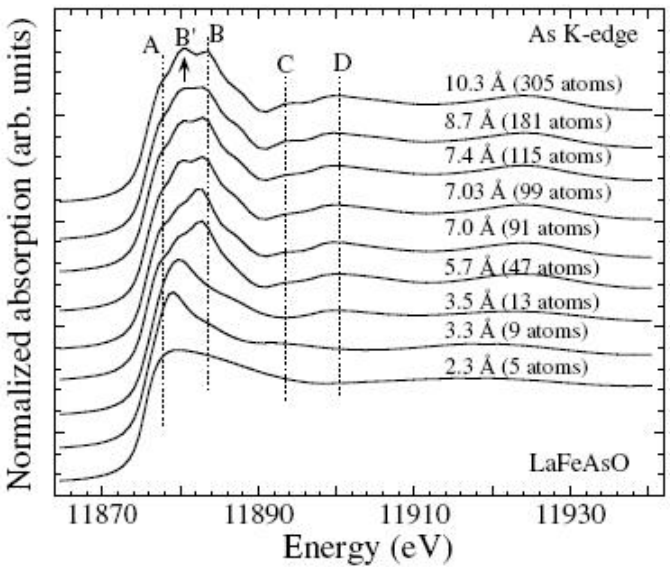

Fig. 3.1.3.3 *The multiple-scattering calculations of As K-edge XANES of the LaFeAsO with increasing cluster size.*

Let us now look at the electronic structure. For this purpose we have calculated site projected density of states (DOS) for the REFeAsO. Incidentally the gross features in the projected DOS are similar for all REFeAsO. Figure 3.1.3.4 shows the projected DOS along with the calculated As K edge-XANES for the representative LaFeAsO system. The ground state electronic configuration of Arsenic atom is $[Ar]3d^{10}4s^24p^3$ and the As K-edge spectra probes the transition of core *1s* electrons to the empty p states. Indeed, the shape of As *4p* DOS correspond well to the XANES features (Fig. 3.1.3.4), suggesting that the As K-edge XANES is well described by transition from the *1s* to *4p* states. With a brief look, it can be concluded that the absorption jump feature A has predominant As *4p* character with admixed La *d* and O *p* states. The feature B is due to As *4p* admixed with Fe *p* states. Also, the distant features C' and C appear to have predominantly As *4p* character. On the other hand, the feature B' is more likely to be due to the *4p* states of Arsenic atoms highly admixed with the Lanthanum *d* states. Furthermore, this feature should also have some admixing of O p and Fe *p* states. From the DOS calculations it can be further concluded that the B' has a direct correlation with the local geometry of the LaO spacer layers with important implication on the electronic states derived by the constituents (i.e. La and O).

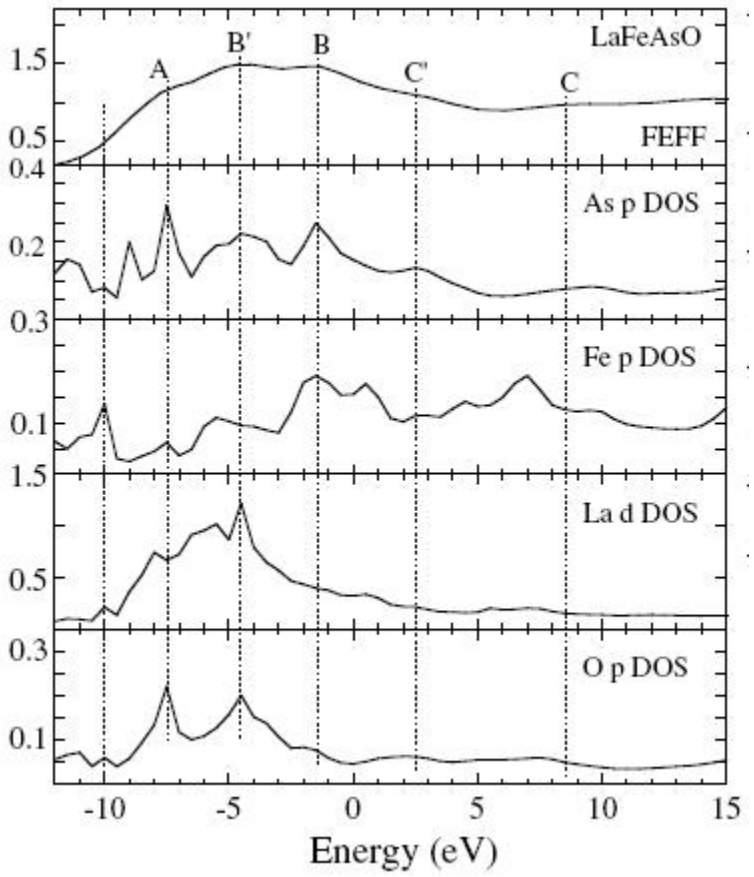

Fig. 3.1.3.4 *The theoretical spectrum of LaFeAsO at the As K-edge and site-projected density of states. The Fermi energy (E_F) is indicated by the vertical dotted line at about $-10eV$.*

Recently, we have investigated the rare-earth L_3-edge XANES of the REFeAsO system [18, 19], suggesting that the oxygen order/disorder should have significant role in the properties of the oxypnictides. It was found that interlayer disorder is relatively lower in the case of LaFeAsO in comparison to the SmFeAsO in which it appears significant due to higher interlayer coupling (higher vertical position of the As atoms). We should also underline that the misfit strain between the REO and the FeAs slabs could easily control the interlayer order/disorder. In the SmFeAsO, FeAs slabs are less strained while the vertical position of As atoms is higher [16], with a high interlayer coupling and hence more interlayer disorder. On the other hand, the vertical position of As atoms is lower in the case of LaFeAsO, leading a higher interlayer order. Incidentally higher interlayer disorder appears to induce higher order within the REO block layers, shown by shape resonance peaks in the rare-earthL_3-edge spectra of REFeAsO [18].

3.1.3.2 *As K-edge EXAFS measurements: results and discussion*

Figure 3.1.3.5 shows As K-edge EXAFS oscillations of REFeAsO samples at low temperature (80 K) extracted from the X-ray absorption spectra measured on powder samples [150]. The EXAFS oscillations are weighted by k^2 to highlight the higher k-region. There are evident differences between the EXAFS oscillations due to differing local structure of REFeAsO with different RE atom (see e.g. the oscillation around k=6-8 $\AA^{-1}$ and in the k range above 10-14 $\AA^{-1}$). The differences in the local structure could be better appreciated in the Fourier transforms of the EXAFS oscillations providing real space information.

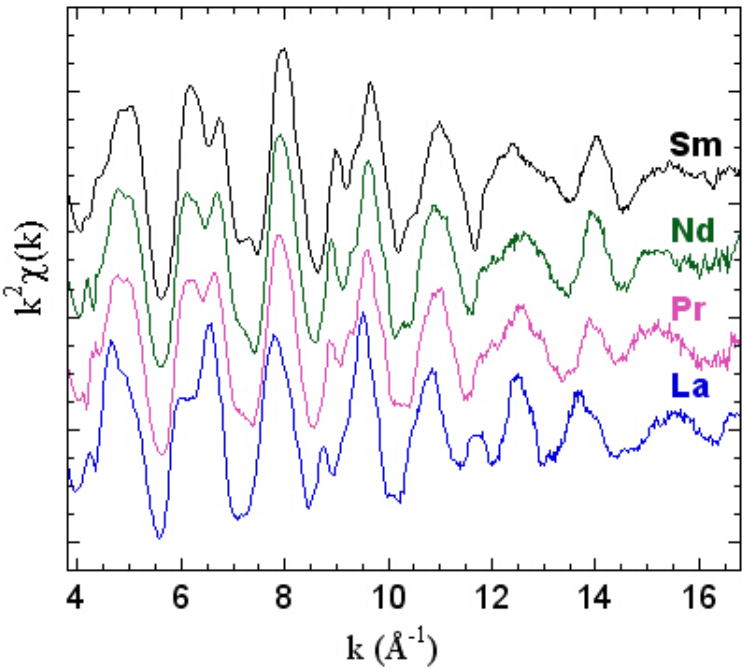

Fig. 3.1.3.5 *EXAFS oscillations (multiplied by k^2) extracted from the As K-edge absorption spectra measured on REFeAsO system (RE =La, Pr, Nd and Sm) at low temperature (80 K) [150].*

Figure 3.1.3.6 shows magnitude of the Fourier transforms $|FT\chi(k)k^2|$. The Fourier transforms are not corrected for the phase shifts due to the photoelectron backscattering and represent raw experimental data. The main peak at ~2.4 Å is due to As-Fe (4 Fe atoms at a distance ~2.4 Å) bond length and the peak at ~3.5 Å corresponds to the As-RE (4 RE atoms at a distance ~3.3 Å), As-O (4 O atoms at a distance ~3.6 Å) and As-As (4 As atoms at a distance

~3.8 Å and 4 As atoms at a distance ~4.0 Å) bond length. From the first look one can see local structural differences with variable rare-earth atoms. While the main Fourier transform peak at ~2.4 Å remains almost the same, the other peak seems to appear with a decreased amplitude with decreasing rare-earth size. Figure 3.1.3.7 shows the selected region of the Fourier transform between 2.8 and 4.7 Å. We can observe a systematic shift at lower distance of the peak position at 3.2 A, that you can ascribe at As-RE bond, and simultaneously the splitting of this peak in two distinct peaks with decreasing the rare-earth size.

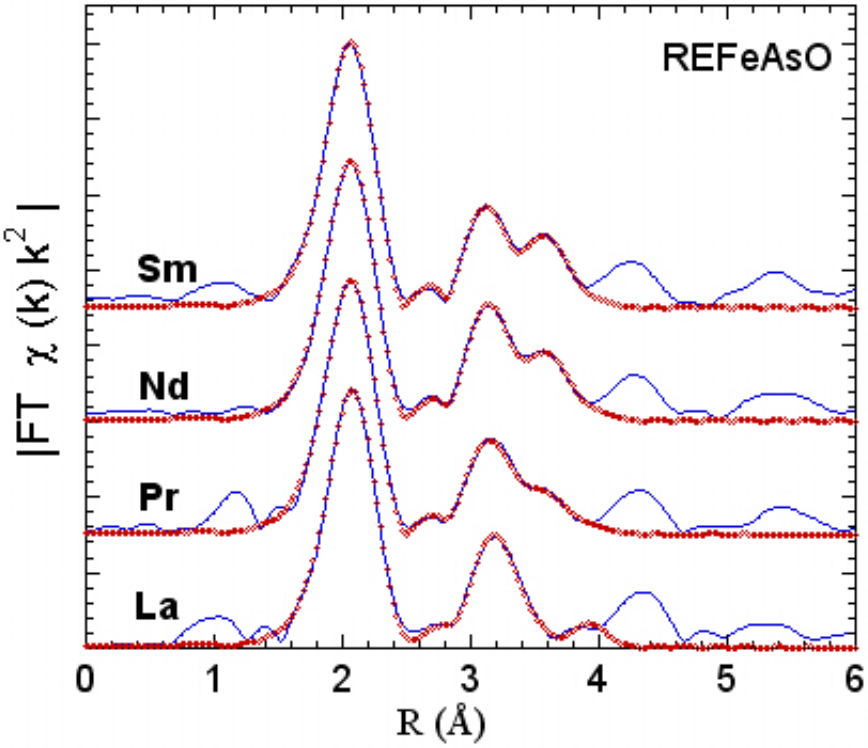

Fig. 3.1.3.6 *Fourier transforms of the As K-edge EXAFS oscillations showing partial atomic distribution around the As in the ReOFeAs system. The Fourier transforms are performed between* $k_{min} = 3.8\AA^{-1}$ *and* $k_{max} = 16.8\AA^{-1}$ *using a Gaussian window. The main peak at 2.4Å is due to Fe-As bond while the peak structure at 3.3Å represents the As-RE, As-O and As-As bonds. The phase corrected Fourier transform (blue square) represents a fit over five shells, i.e., Fe-As, As-RE, As-O and As-As. Note that varying the rare-earth size the first peak remains almost the same while the second peak shows an evident change.*

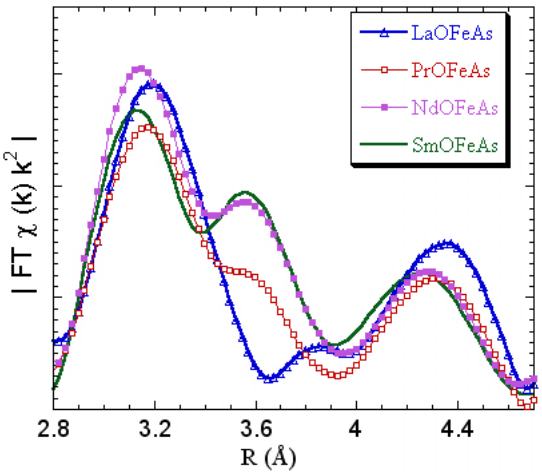

Fig. 3.1.3.7 *Zoom over the second and third peaks of the Fig 3.1.3.6, showing the difference between the near neighbour distribution around the As atom in REFeAsO systems.*

The WINXAS code was used for the model fit with calculated backscattering amplitudes and phase shift functions. The number of independent data points, $Nind = (2\Delta k \Delta R)/\pi$ [15] was 16 for the present analysis (Δk=13 $\AA^{-1}$ (k=3.8-16.8 $\AA^{-1}$) and ΔR=4 Å), but we have used only ten independent parameters to fitting. Starting parameters were taken from the diffraction studies [17, 56]. A representative five shell model fit is shown with experimental Fourier transform in the Fig. 3.1.3.6.

The average radial distances as a function of rare earth atom are shown in Fig. 3.1.3.8. The Fe-As distance (open square) does not show any appreciable change with the rare-earth atom size, revealing strongly covalent nature of this bond. This is inconsistent with some diffraction experiments revealing substantial change of this bond with the rare-earth size [11], while consistent with others showing stiffness of this bond [17, 56]. On the other hand, there is a gradual decrease of the average As-RE distance (full turbot) with decreasing rare earth size, consistent with the chemical pressure effect.

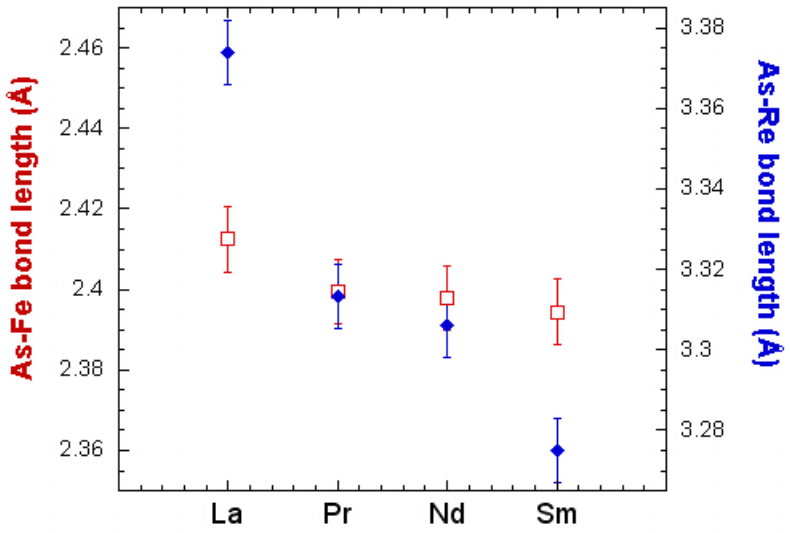

Fig. 3.1.3.8 *As-Fe (open square) and As-RE (full turbot) distances at 80 K as a function of rare-earth atom. The As-Fe bond length hardly shows any change, in agreement with the data diffraction. On the other hand, the As-RE bond length decreases with rare earth size, as a chemical pressure effect. The similar results were previously obtained with the measurements at Fe K-edge.*

Figure 3.1.3.9 shows the correlated DWF as a function of rare earth atoms measuring the MSRD of different bond lengths. The As-Fe is not influenced by rare-earth ion size, indicating the stiffness of the bond. In agreement with the results of Tyson et al [128], we can confirm the strongly covalent nature of the Fe-As bond [16]. The As-RE MSRD seems remain constant or show a trend of increase. In summary, we have measured the local structure of REFeAsO with variable rare-earth ion revealing highly covalent nature of the As-Fe bond. The As-RE bond length decreases with rare-earth size. A similar trend it was observed for the Fe-RE distance using Fe K-edge measurements. On the other hand the corresponding MSRD in both cases are found to be remaining almost constant or show a trend of increase.

Considering the conventional superconducting mechanism in the strong coupling limit [129, 130], the electron-phonon interaction parameter is inversely proportional to the phonon frequency, i.e., proportional to the MSRD. Since the T_C of the REFeAsO (if doped) increases with decreasing rare-earth size, it is reasonable to think that the As-RE MSRD tend to increase with increasing T_C, and hence it is more plausible to think that the As-RE mode is somehow parti-

cipating in the electron-phonon interaction for the superconductivity. The fact that MSRD of the As-RE represents out of the plane motion, the result is an indication for inter-layer coupling to be important in the superconductivity of the REFeAsO.

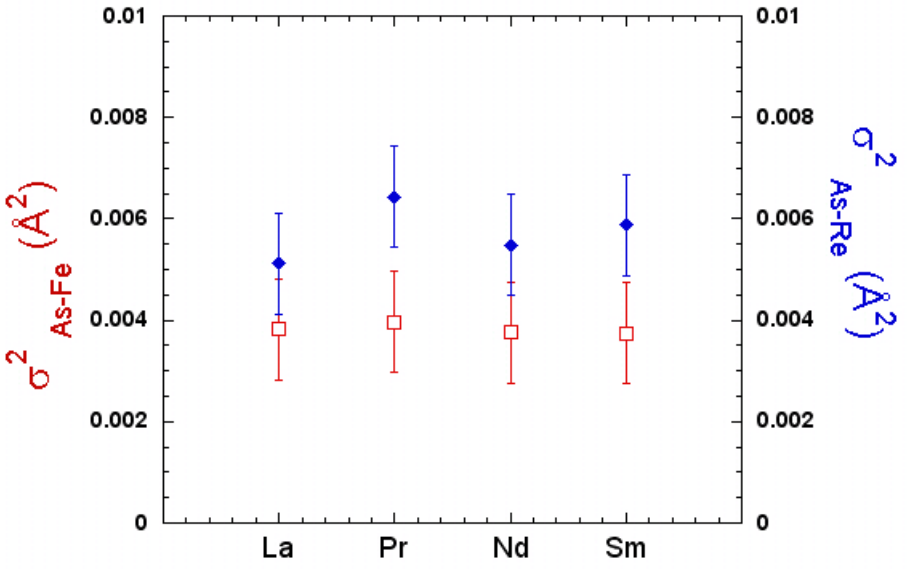

Fig. 3.1.3.9 *Mean square relative displacements (MSRD) of the As-Fe (open square) and As-RE (full turbot) pairs at 80 K as a function of rare-earth size. As the bond length (Fig. 3.1.3.8), the MSRD of As-Fe hardly shows any change indicating strongly covalent opposite trend.*

3.1.4 Summary and conclusions

Local structure of REFeAsO (RE = La, Pr, Nd and Sm) system has been studied as a function of chemical pressure varied due to different rare-earth size.

First, we have adress our attention to the FeAs slabs. Indeed, the FeAs slabs is identified as the electronically active layer, so the knowledge of the local atomic distribution around the Fe atom is fundamental to provide informations on the atomic correlations. Fe K-edge EXAFS measurements in the fluorescence mode has permitted to compare systematically the interatomic distances and their mean square relative displacements (MSRD). We find that the Fe-As bond length and the corresponding MSRD hardly show any change, suggesting the strongly covalent nature of this bond, while the Fe-Fe and Fe-RE bond lengths decrease with decreasing rare-earth size. Moreover, the As height on the Fe-Fe plane increases with decreasing rare-earth size, and consequently also the Fe-As-Fe angle ϑ_3 decreases, revealing perfect Fe_4As tetrahedron [11, 17] for the SmFeAsO. Our results underline that there is a relationship between the anion heigth and the superconducting properties in Fe-based quaternary systems. Therefore, we have decided to explore the arrangements of the local structure around the As atom.

Second, As K-edge X-ray absorption near-edge structure (XANES) spectroscopy has been used to investigate the local geometry around the pnictogen site in the REFeAsO oxypnictides, combined with full multiple-scattering calculations to understand different XANES features. The As K-edge XANES spectrum for the LaFeAsO is found to be significantly different from the other oxypnictides, because a reduced interlayer disorder in the LaFeAsO in comparison to the other oxypnictides. The disordering seems significant in the SmFeAsO system due to a higher interlayer coupling (higher vertical position of the As atoms) and a smaller misfit strain [21]. Once doped by substitution in the REO layer, the SmFeAsO with higher interlayer disorder shows higher T_C. The present results suggest an intimate relation or an interplay between the superconductivity and the order/disorder in the spacer layers, recalling the out-of-plane disorder-controlled superconductivity already addressed in the cuprate superconductors [133]. Since the vertical position of the As atom changes systematically with the rare earth size, this have a direct influence on the local geometry of the REO slabs.

Third, we have study the changes in the local geometry of the REO slabs due to different rare-earth size. RE L_3-XANES is an ideal tool to study the local geometry around the RE and has often been applied to study rare earth containing materials [131, 132]. While the

L_3 white lines (WL) hardly show any change across the tetragonal to orthorhombic structural phase transition temperature, above the WL a systematic changes are observed, due to the varying local geometry with the rare earth size. The energy separation between the WL and the continuum resonances change consistently with a change of RE-As and RE-O distance, due to changing misfit between the FeAs and REO sub-layers. A systematic change of the relative intensities of the continuum resonance features is also observed. The results suggest that the interlayer coupling between the Fe-As and the spacer (REO) layer may also play a role in the superconductivity mechanism of the REFeAsO. The XANES spectra have been also simulated by full multiple scattering calculations to describe the different experimental features and their evolution with the RE size. The near edge feature just above the L_3 WL is found to be sensitive to the ordering/disordering of oxygen atoms in the REO layers. In addition, shape resonance peaks due to As and O scattering change systematically, indicating local structural changes in the FeAs slabs and the REO spacers due to RE size. The results confirm that the interlayer coupling and oxygen order/disorder in the REO spacers have an important role in the superconductivity and itinerant magnetism of the oxypnictides.

We have found that the local structure of REFeAsO (RE = La, Pr, Nd and Sm) system is strongly influenced by chemical pressure, induced by changing the rare-earth size. In particular, the differences in the local structure can be ascribed to the different interlayer coupling between the REO spacer layers and the FeAs active layers, as a function of RE size. Moreover, the order/disorder in the REO spacer layers, due to oxygen arrangements, is an additional parameter that we have take in account to describe the functionale properties in the quaternary Fe-based systems.

3.2 Effect of charge density and temperature in superconducting $NdFeAsO_{1-x}F_x$

In this section we explore the local structure of $NdFeAsO_{1-x}F_x$ as a function of charge density and temperature. Temperature-dependent x-ray absorption measurements were performed in transmission mode on powder samples of $NdFeAsO_{1-x}F_x$ (x = 0.0, 0.05, 0.06, 0.15 and 0.18; the x values given correspond to the nominal composition, the actual values are lower than the nominal values for higher x [151]). Prior to the absorption measurements, the samples were characterized for the phase purity and the average structure by X-ray diffraction measurements [21, 151]. The X-ray absorption measurements were made at different beamlines:

- *As K-edge EXAFS measurements:* **BM26A** beamline of the European synchrotron radiation facility, Grenoble (France). The synchrotron light emitted by a bending magnetic source was monochromatized by a double crystal Si(111) monochromator. While the samples x=0.0 and 0.05 are non-superconducting, showing tetragonal to orthorhombic structural phase transition, the samples with x=0.15 and 0.18 are superconducting with $Tc \approx 20K$ and $\approx 40K$ respectively, without any evidence of the structural phase transition [151]. For the temperature dependent measurements (15-300 K), a continuous flow He cryostat with a temperature control within an accuracy of ±1 K was used.

- *Nd L_3-edge XANES measurements*: **XAFS** beamline of the Elettra Synchrotron Radiation Facility, Trieste, where the synchrotron radiation emitted by a bending magnet source was monochromatized using a double crystal Si(111) monochromator. The superconducting transition temperature for the F-doped $NdO_{0.94}F_{0.06}FeAs$ was found to be 49 K [151]. The L_3-XANES measurements were made at two temperatures (room temperature and 80 K) in the transmission mode using three ionization chambers mounted in series for simultaneous measurements on the sample and a reference. For the low temperature measurements, the samples were mounted on a liquid nitrogen cryostat cold finger enclosed in an Al shroud with a Be window. The sample temperature was measured to be 80±1 K for the low temperature measurements.

A minimum of two scans (with high signal to noise ratio) were measured at each temperature to make sure the reproducibility. Standard procedure was used to extract the EXAFS oscillations from the absorption spectrum [131, 132].

3.2.1 As K-edge EXAFS study

Arsenic K-edge EXAFS has been used to retrieve direct information on the Fe-As bond lengths in superconducting (x= 0.15 and 0.18) and non-superconducting (x = 0.0 and 0.05) samples. These results indicate that there exist distinct lattice dynamics in the superconducting and non-superconducting systems, albeit the differences are smaller [22].

Figure 3.2.1.1 shows Fourier transform (FT) magnitudes of the arsenic K-edge EXAFS oscillations (the insets show the EXAFS oscillations), measured on $NdFeAsO_{1-x}F_x$ (for x= 0.0, 0.05, 0.15 and 0.18) samples, providing partial atomic distribution around the arsenic atoms. At room temperature, all the samples studied have tetragonal structure (space group P4/nmm) [151]. The x=0.0 and 0.05 samples show structural phase transition from the tetragonal-to-orthorhombic phase below $\sim 130K$ [151]. There are four Fe atoms as the near neighbors of arsenic at a distance ~ 2.39Å (main peak at ~ 2Å). The next-nearest neighbors are four Nd atoms at a distance ~ 3.28Å and four oxygen atoms at a distance ~ 3.51Å, followed by eight As atoms at ~ 3.9Å. Contributions of these distant shells appear mixed, giving a multiple structured peak at $\sim 2.5 - 4.5$Å (Fig. 3.2.1.1). Apparently, the atomic distribution around the arsenic is similar in all the samples, as evident from the FT as well as the EXAFS oscillations. In the $NdFeAsO_{1-x}F_x$ system, the arsenic atoms have the nearest neighbors as Fe atoms, and their contributions to the arsenic K-edge EXAFS are well separated from all other shell contributions. This makes the arsenic K-edge EXAFS data highly suitable for extracting quantitative information on the Fe-As bond lengths and the related MSRDs. Here we have exploited this possibility and performed single-shell model fits to the EXAFS oscillations due to the Fe-As bond lengths. In the present case, we have used a single-shell EXAFS modeling [15] to extract the Fe-As bond correlations. For such a single-shell analysis, we have used the WINXAS package [153], with backscattering amplitudes and phase shifts calculated using the FEFF code [154] with the crystal structure data from diffraction [151] as input. In the single-shell least-squares fit, the number of independent data points, $Nind \sim (2\Delta k \Delta R)/\pi$ [15] were about 13 ($k = 14$Å^{-1}($k = 3$–17Å^{-1}) and $R = 1.5$Å), but we used only two parameters, the radial distance R_i and the corresponding MSRD σ_i^2 , as the refinable variables, fixing all other parameters to obtain reliable information on the Fe-As bond correlations.

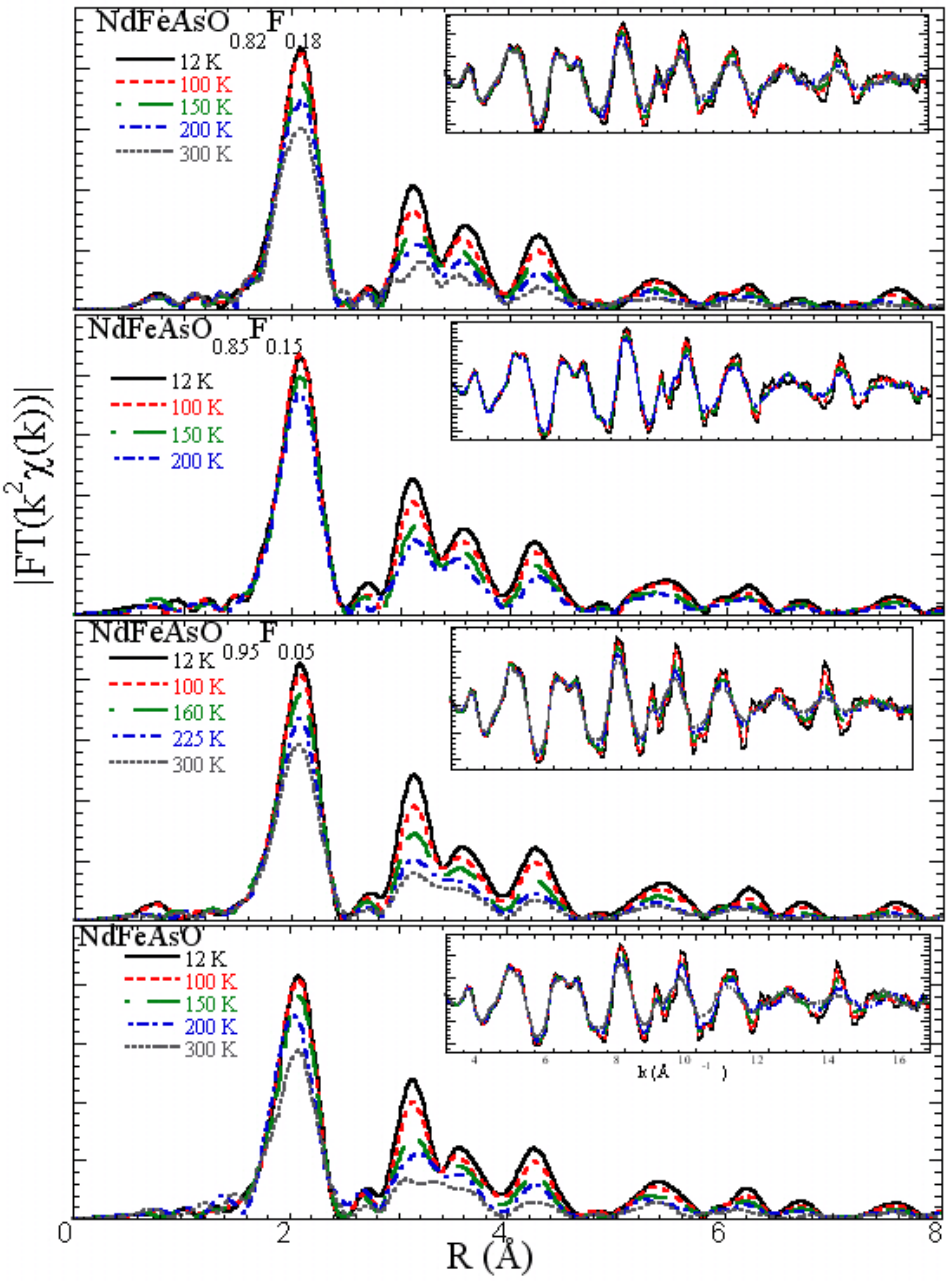

Fig. 3.2.1.1 *Fourier transform (FT) magnitudes of the arsenic K-edge EXAFS oscillations for the $NdFeAsO_{1-x}F_x$ (x = 0.0, 0.05, 0.15 and 0.18). Corresponding EXAFS oscillations are shown in the insets. The FTs are not corrected for the phase shifts, thus representing raw experimental data. A systematic temperature dependence is evident from the gradual change in the FT intensities.*

The uncertainties in the derived two parameters, R and σ^2, were estimated by the standard EXAFS method [15]. The canonical approach to error estimation is to determine the region around the best fit that contains the true value with a certain probability β. The projection of that volume onto an axis corresponding to a parameter gives the parameter errors, for a chosen value of β. In general these uncertainties are dependent on the experimental as well as EXAFS data extraction procedures, in addition to the uncertainties coming from the statistical χ^2-procedure. In the present case, due to the adoption of identical experimental conditions and EXAFS data extraction procedures, the first kind of uncertainties are minimal. However, we have set the error bars on derived parameters, R and σ^2, to two times the highest uncertainty estimated. This is to underline the fact that we are interested in discussing the relative changes rather than the absolute values of these parameters.

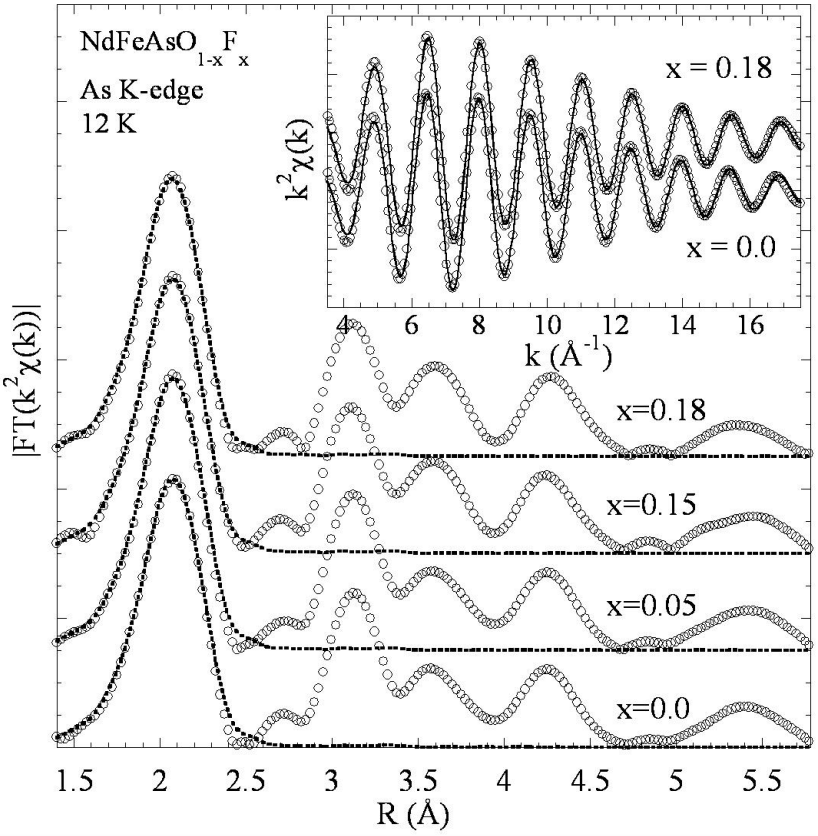

Fig. 3.2.1.2 *FTs of the arsenic K-edge EXAFS oscillations measured on $NdFeAsO_{1-x}F_x$ (x = 0.0, 0.05, 0.15 and 0.18) at low temperature (12 K)(symbols), together with a single shell fit (solid line). The filtered EXAFS oscillations corresponding to the first shell (As-Fe pairs) together with the model fits (solid lines) for x=0.0 and 0.18 samples at 12 K are shown in the inset.*

Figure 3.2.1.2 shows the single-shell model fit in the real and k-space at 12 K for samples with different x. Here it should be mentioned that the samples used in the present study are phase pure with the amount of impurities below the sensitivity of the x-ray diffraction. The main impurity phase present in the doped samples is the NdOF phase, which showed an F-doping dependence [151]. However, in the present case, this impurity phase has no influence on the arsenic K-edge EXAFS data. The impurities which can possibly interfere with the present EXAFS results, like the FeAs phases and NdAs phases, were less than 1% [151], thus ruling out any contribution from such impurity phases in the data presented here.

Figure 3.2.1.3 shows temperature dependence of the Fe-As bond distances determined from the single-shell analysis of the arsenic K-edge EXAFS data. The Fe-As distances in all the samples are very similar, around 2.39Å . The overall temperature dependence of the distance also looks very similar. However, one can notice a small change in the superconducting samples somewhat close to the transition temperature, with no such changes evident in the parent compound. An earlier temperature-dependent x-ray diffraction study on the $NdFeAsO_{0.85}$ superconductor has shown an abrupt change in the Fe-As distance around T_C [155].

Present results also show that the Fe-As distance tend to change near T_C for the superconducting (x= 0.15, 0.18) samples (Fig. 3.2.1.3 upper panels). But we do not see significant changes in the Fe-As bond lengths or corresponding MSRD across the structural phase transition for the parent compound, which is consistent with earlier EXAFS studies on LaFeAsO [128], SmFeAsO [156] and $BaFe_2As_2$ [157], showing no change in the Fe-As bond length and corresponding MSRD across the structural phase transition. As shown in a recent diffraction study of the REFeAsO (RE stands for rare-earth) system, data from single crystals are important for a better understanding of structural phase transition properties [158]. For example, a recent study on the NdFeAsO single crystal revealed two low temperature phase transitions in addition to the tetragonal-to-orthorhombic transition at $T_S \sim 142K$ [159], indicating the importance of single crystals in revealing the intricate properties of FeSCs. Naturally EXAFS studies using single crystals are also going to be important, in addition to the angular-dependent local information provided by the polarization-dependent EXAFS measurements [12].

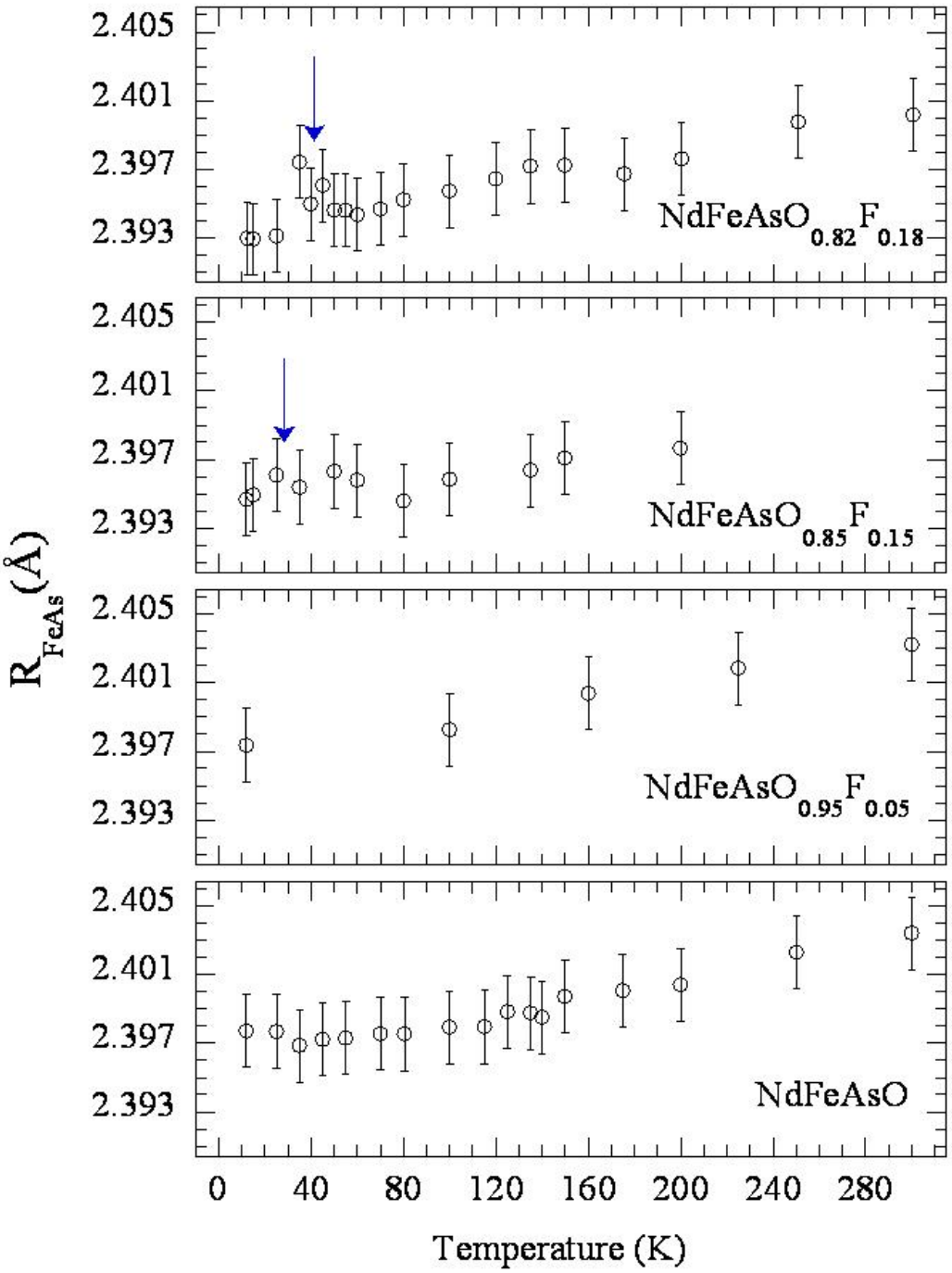

Fig. 3.2.1.3 *Temperature dependence of the Fe-As bond distance for the $NdFeAsO_{1-x}F_x$ system. The Fe-As bond length shows only weak doping and temperature dependence, indicating the covalent nature of the bond. However, there appears a small anomaly (arrow marks in the upper panels) in the superconducting samples close to the transition temperature, with no such*

changes evident in the non-superconducting compounds.

Figure 3.2.1.4 shows mean square relative displacements (σ^2) of the Fe-As pair, describing the distance-distance correlation function (correlated DW factors). The MSRD is a sum of temperature-independent (σ_0^2) and temperature-dependent terms [15], i.e.

$$\sigma^2_{Fe-As} = \sigma_0^2 + \sigma^2_{Fe-As}(T)$$

In several cases, the temperature-dependent term can be described by the correlated Einstein model [15]:

$$\sigma^2_{Fe-As}(T) = \frac{\hbar}{2\mu_{Fe-As}\omega_E} coth(\frac{\hbar\omega_E}{2k_BT})$$

where μ_{Fe-As} is the reduced mass of the Fe-As bond and ω_E is the Einstein frequency. The related Einstein temperature can be obtained from the expression $\Theta_E = h\omega_E/k_B$. In the present case, temperature dependence of σ^2_{Fe-As} is found to follow the correlated Einstein model. The description of σ^2_{Fe-As} using this model yields Θ_E values to be $348 \pm 12K$ and $326 \pm 12K$, respectively, for the x=0.18 and 0.0 samples. Notice that the uncertainty in Θ_E given above is obtained from the least-squares fit considering the error bars on the data points. The obtained Einstein frequencies are in the range of phonon frequencies observed in Raman studies for the modes involving arsenic and iron atoms [161, 162]. In addition, different Einstein frequencies (ω_E) indicate different local force constants ($k = \mu_{Fe-As}\omega_E^2$, where k is the effective force constant) for the Fe-As bonds in the superconducting and non-superconducting samples. The calculated local force constants for the Fe-As bonds are $\sim 6.65eV\text{Å}^{-2}$ and $\sim 5.85eV\text{Å}^{-2}$, respectively, for the superconducting and nonsuperconducting samples. Thus the Fe-As bond length seems to get harder in the superconducting regime. This observation is an indication of the non-negligible role of the lattice modes in the superconductivity of these materials.

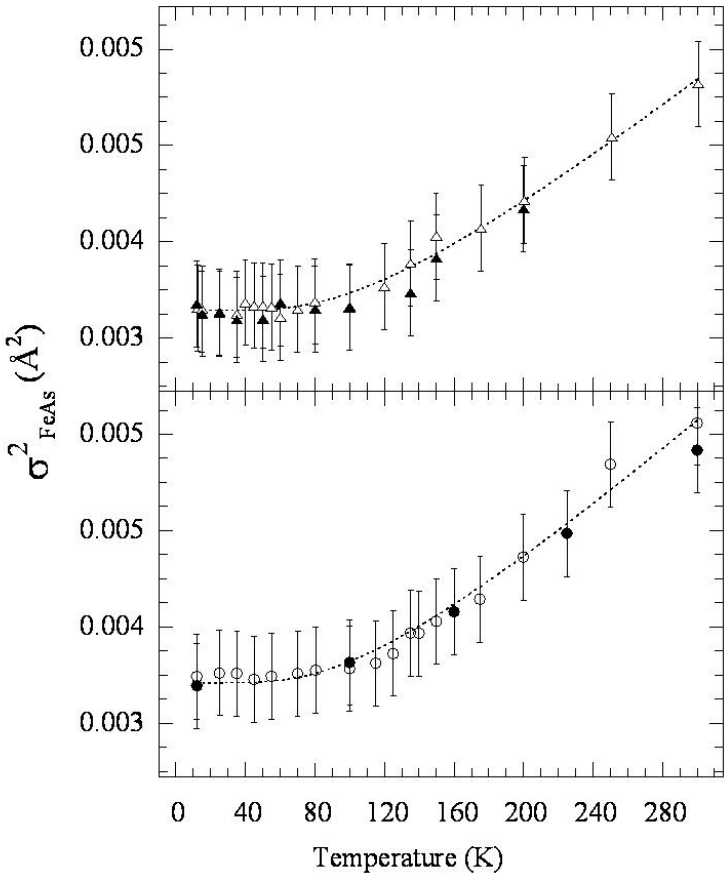

Fig. 3.2.1.4 *Temperature dependence of the Fe-As MSRD (symbols) for the* $NdFeAsO_{1-x}F_x$ *(x = 0.0, 0.05, 0.15 and 0.18) system. The upper panel shows the data on the superconducting samples (open and filled symbols correspond to x=0.18 and 0.15 samples, respectively), while the lower panel shows the data on the non-superconducting samples (open and filled symbols correspond to x = 0.0 and 0.05 samples, respectively). The dotted lines represent the correlated Einstein model fit to the data. The Einstein temperatures,*Θ_E*, are* $348 \pm 12K$ *and* $326 \pm 12K$*, respectively, for the superconducting (x=0.18) and non-superconducting (x=0.0) samples. The temperature-independent* σ_0^2 *is found to have a similar value (*~ 0.00073*) in both cases.*

Comparing the already available local structural data on different oxypnictides [16, 18, 128, 156, 157] one can see that the Fe-As bond in these systems shows only small changes with doping and temperature. An EXAFS study on a series of oxypnictides [16] has shown that the Fe-As bond length and the related MSRDs hardly show any change with the varying rare-earth

size, consistent with the strong covalent nature of the Fe-As bonds. On the other hand, earlier studies on F-doped La-1111 and Sm-1111 [156] compounds have shown the presence of an anomaly in the temperature dependence of the Fe-As MSRDs. But these anomalies were seen to be very weak compared to those observed for the cuprates [12]. Indeed another study on the superconducting La-1111 system [128] did not indicate any such anomaly. Such anomalies were also not seen in the K-doped Ba-122 system [157] and F-doped Ce-1111 system [163]. From the results presented in figure 3.2.1.4, for the F-doped Nd-1111 system, there is no evidence for a significant anomaly in the MSRD of Fe-As bonds associated with the superconducting transition. Here, we make an explicit comparison of the Fe-As MSRDs of the superconducting Sm-1111 and Nd-1111 samples to underline that the Fe-As MSRDs tend to change around the superconducting transition temperature, albeit the anomalies are indeed weak compared to what has been seen in the copper oxide superconductors [12]. Figure 3.2.1.5 shows the temperature dependence of the MSRDs of the Fe-As bond for the NdFeAsO, compared with that of the LaFeAsO [128], SmFeAsO [156] and $BaFe_2As_2$ [157].

In all cases, the MSRD data are extracted from the arsenic K-edge EXAFS. The correlated Einstein model fit to the data is also indicated in the figure (as dotted lines). From Figure 3.2.1.5, it can be seen that the Fe-As MSRDs show almost identical temperature dependence for these different oxypnictide systems. Although the temperature dependence looks very similar, there seems to be a systematic change in the Einstein temperature.The Θ_E values are, respectively, $316 \pm 5K$, $318 \pm 10K$, $326 \pm 12K$ and $328 \pm 12K$ for LaFeAsO, $BaFe_2As_2$, NdFeAsO and SmFeAsO. There is a clear increase in the force constant of the Fe-As bonds, with increasing rare-earth size in the '1111' series. Optical studies using single crystals of the '1111' series reveal that the Fe-As stretching mode in these oxypnictides shows substantial hardening with the rare-earth size, being harder for the NdFeAsO and SmFeAsO showing higher T_C in comparison to the LaFeAsO [164]. The Eu mode frequency for the $BaFe_2As_2$ [160] is also found to be similar to that of the '1111' series [164]. In the '1111' family, the changing rare-earth ionic size leads to a change in the pnictogen height above the Fe plane [153] and thus a different interlayer atomic correlation [18, 19]. Local structural studies using atomic pair distribution function analysis on $Ba_{1-x}K_xFe_2As_2$ show that, although the changes in the Fe-As bonds are minimum, the $FeAs_4$ tetrahedra show a systematic evolution with K doping [165]. Indeed a small change in the pnictogen height is known to have a significant effect on the electronic properties of the

system through changing degeneracy between different Fe *3d* bands (in particular between the $d_{x^2-y^2}$ and d_{xz}/d_{yz}), with a direct implication on the magnetic structure and superconductivity [111, 115].

Very recent photoemission studies have shown this pnictogen-height-dependent change in the electronic structure [166], confirming the importance of even very small local structural changes in determining the properties of the FeSCs. To further enlighten the possible anomaly around the superconducting transition temperature, we have made an explicit comparison between the temperature-dependent Fe-As MSRDs for the F-doped highest T_C Nd-1111 and Sm- 1111 [156] superconductors (see, e.g., Fig. 3.2.1.5(d)). The inset in Figure 3.2.1.5(d) is a zoomed view around T_C. The error bars given here are identical to those given in reference [156]. For the $NdFeAsO_{0.82}F_{0.18}$ sample, there is a weak anomaly in the temperature dependence of the Fe-As MSRDs similar to that observed in the superconducting $SmFeAsO_{0.931}F_{0.069}$ [156]. However, the anomaly is well within the experimental uncertainties. This situation is different from that of cuprates [12] where several measurements showed clear lattice anomalies associated with the superconducting transition. Although more experiments are needed, the weakness of the anomalies does not imply that lattice fluctuations have a minor role in the Fe-based superconductors. Indeed, the empirical relationship between the superconducting transition temperature and the $FeAs_4$ tetrahedra in FeSCs [11, 68] clearly establishes the role of the local lattice in the superconducting properties. Local structural studies also underline the same point [16, 165]. The increased force constant of the Fe-As bonds in the superconducting sample compared to the parent compound in the Nd-1111 system indicate the importance of lattice dynamics in determining the properties. Systematic changes in the Fe-As force constant within the different ironpnictide compounds, as revealed by the present study, further support this.

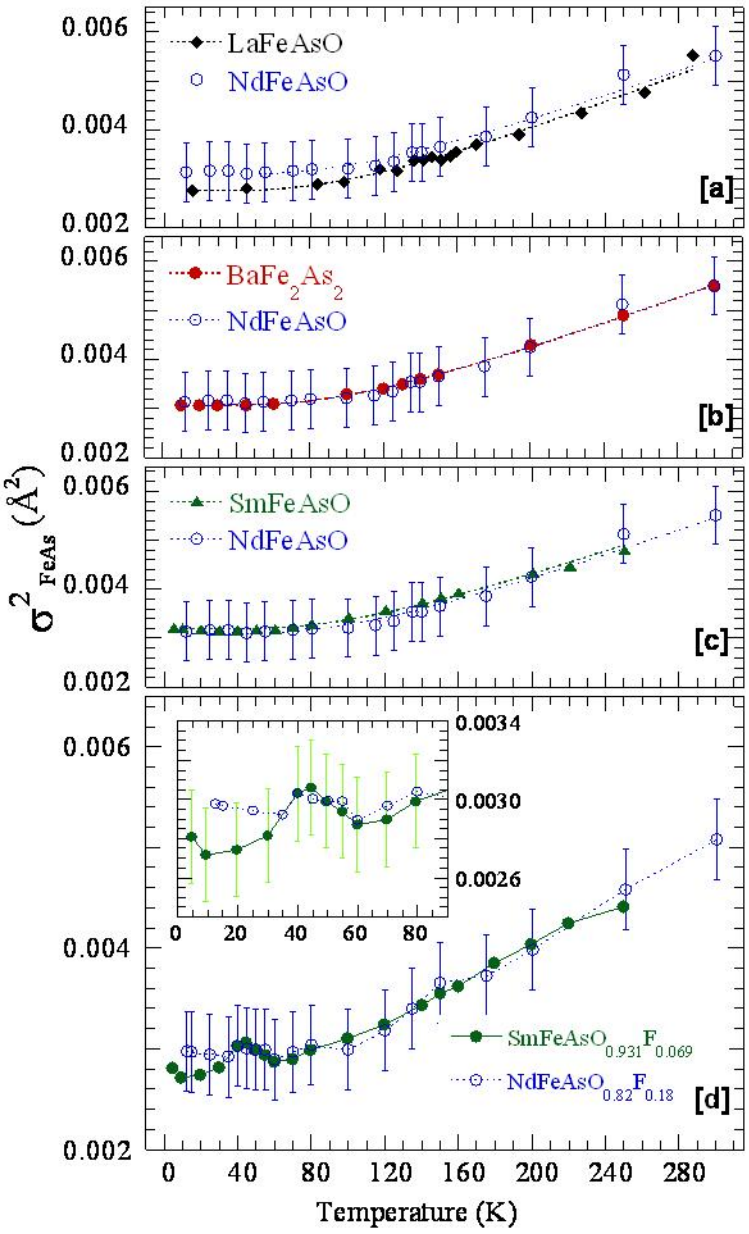

Fig. 3.2.1.5 *Temperature dependence of the Fe-As MSRDs for the NdFeAsO system (open circles in all panels) is compared with that of the LaFeAsO [128] (filled diamonds (a)), the $BaFe_2As_2$ [157] (filled circles, (c)) and SmFeAsO [156] (filled triangles, (b)). For facilitating a better comparison, the LaFeAsO [128], $BaFe_2As_2$ [157] and SmFeAsO [156] data are scaled by 0.0004, 0.0008 and 0.0017, respectively. Panel (d) presents the temperature dependence of the Fe-As MSRD for the F-doped superconducting Nd-1111 and Sm-1111 [156] (with the latter scaled*

by 0.0012). Overall temperature dependences of the two superconducting systems are identical. The inset in panel (d) shows a zoom around the superconducting transition temperature. The error bars in the inset are identical to those given in reference [156].

3.2.2 Nd L_3-XANES study

Let us turn to the effect of doping on the L_3-XANES. To explore this, we have used NdFeAsO as a representative and measured Nd L_3-XANES on the undoped and F-substituted system (x=0.06) [12]. Figure 3.2.2.1 shows the measured Nd L_3-XANES at room temperature on the NdFeAsO and the superconducting $NdFeAsO_{1-x}F_x$ system ($T_C \sim 49K$).

Both samples are in their tetragonal phase and hence the differences reflect the effect of F-substitution. The L_3-edge WL intensity shows a significant increase with F-doping, suggesting an increase of the localization of the RE empty d density of states [146]. In addition, a substantial change in peaks B1 and B2 can be seen (inset of Fig. 3.2.2.1). Recently Sun et al [167] have studied $CeO_{1-x}F_xFeAs$ by the Ce L_3-XANES system as a function of external pressure, revealing a drastic decrease of the WL intensity while the Tc decreases with increasing hydrostatic pressure. Incidentally, the results reported here show a more intense Nd L_3 WL for the superconducting system, and hence the increased intensity (more atomic like character) of the L_3 WL may be somehow related to the superconductivity.

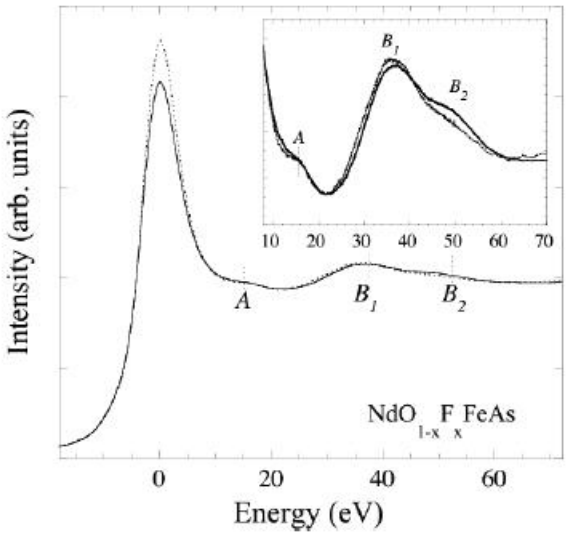

Fig. 3.2.2.1 *Nd L_3-edge for the undoped (solid) and F-substituted (dotted) superconducting systems at room temperature. Both the samples are in their tetragonal phase and hence the*

differences are merely due to the F-insertion. The inset shows a zoom into the features A, peak B1 and peak B2 [18].

It is possible that the F-substitution in the NdFeAsO causes reduced hybridization between the Nd *5d* and admixed *4f* orbitals, similar to the *4f*-superconductors [168], in which the superconductivity gets suppressed with increased hybridization. On the other hand, the peak B1 seems to show a different effect of F-doping. Indeed, peaks B1 and B2 tend to merge (peak B1 hardly shows any shift while peak B2 appears at a lower energy). The doping of F induces an increase of Nd-O/F distance; hence the shift of the peak B2 towards lower energy is reasonable. On the other hand, the diffraction data reveal a shrinkage of the RE-As bonds; hence a shift of the peak B1 towards higher energy should be expected, inconsistent with the present results. This may be due to the fact that diffraction tends to average local distortions and is thus less sensitive to localized structural distortions and possible nanoscale inhomogeneities [156].

3.2.3 Summary and conclusions

In conclusion, we have carried out a systematic temperature dependent local structural studies of the $NdFeAsO_{1-x}F_x$ (x = 0.0, 0.05, 0.15 and 0.18) high temperature pnictide superconductor using arsenic K-edge EXAFS. In all the samples, the temperature dependence of the MSRDs of the Fe-As bonds are found to follow the correlated Einstein model. However, the Einstein frequency for the superconducting sample is higher than that of the parent compound, indicating a hardening of the Fe-As bond in the former compared to the latter. The overall temperature dependence of the MSRDs of the Fe-As bond seems to be similar in NdFeAsO, SmFeAsO, LaFeAsO and $BaFe_2As_2$, but with a systematic variation of the corresponding force constants. The changes occurring in the $FeAs_4$ tetrahedra, together with the coupling between the active layer and the spacer layer, may account for the changes in properties of different iron oxypnictide superconductors.

Supplementary informations about the local structure in F-doped NdFeAsO compounds have been obtained by RE L_3-XANES measurements, as previously made for RE-substituted REFeAsO systems. Both the samples are in their tetragonal phase, therefore the differences in the spectra for x=0 and x= 0.06 reflect directly the effect of F-substitution. The increasing in the L_3-edge WL intensity with F-doping, suggesting an increase of the localization of the RE empty d density of states. In addition, a substantial change in the resonances peaks B1 and B2 seems to reflect a different effect of F-doping. The doping of F induces an increase of Nd-O/F distance; hence the shift of the peak B2 towards lower energy is reasonable. On the other hand, a shift of the peak B1 towards higher energy should be expected, inconsistent with the present results. However, this incongruity can be easily solved, beacuse the diffraction tends to average local distortions and is thus less sensitive to localized structural distortions and possible nanoscale inhomogeneities, such in our case.

Chapter 4

Local structure of Fe-based 11 type chalcogenide

Among others, an important development in the field of Fe-based superconductors has been the discovery of superconductivity in the FeSe(Te) chalcogenides with the maximum $T_C \sim 15K$ [41]. Indeed, the PbO-type tetragonal phase of FeSe(Te) has an Fe-based planar sublattice, similar to the layered FeAs-based pnictide structures with stacking of edge-sharing $Fe(Se,Te)_4$ tetrahedra layer by layer. Apart from the similar structural topology of active layers, the chalcogenides show structural transition from tetragonal to orthorhombic phase [61, 67, 53, 169] analogous to that observed in the FeAs-based pnictides [41, 61, 67, 53, 169]. Also, the interplay between the superconductivity and itinerant magnetism, observed in FeAs based pnictides [41], is well extended to the chalcogenides [85, 170, 171]. One of the particularly interesting aspects of chalcogenides is the strong relationship between the superconducting state and the defect chemistry [61, 67, 53, 169]. In addition, the superconducting state can be manipulated by the pressure either chemical [81] or hydrostatic [44, 67, 170]. Over the above, fundamental electronic and magnetic properties are found to show extreme sensitivity to the atomic positions [14, 114] as in the pnictides [115, 114]. On the other hand, the missing spacer layer in $FeSe_{1-x}Te_x$ might be causing a structural symmetry breaking at a local scale in the ternary system [85], characterized by distinct site occupation of Se and Te atoms.

Although the electronic states near the Fermi level in the $FeSe_{1-x}Te_x$ chalcogenides are given by the five Fe d orbitals, it is also true that the fundamental properties have strong

sensitivity toward the chalcogen height [170, 171] as well as the defect chemistry, suggesting a key role for the interaction between Fe *3d* states and chalcogen *p* orbitals near the Fermi level. Therefore, the FeSe(Te) system provides a unique opportunity to study the interplay of the structure, magnetism, and superconductivity in the Fe-based families because of the relative chemical simplicity with added advantage of the absence of any spacer layers that may affect the electronic and structural properties within the active Fe-Fe layers. It is known that a mere knowledge of the long-range ordered structure is generally insufficient to describe electronic functions of a system with interplaying electronic degrees of freedom. Indeed, this has been shown for transition metal oxides in which the electronic functions like superconductivity, colossal magneto-resistance and metal insulator transitions are related with interplaying charge, spin and lattice degrees of freedom [125]. Therefore, a detailed knowledge of the atomic structure for the $FeSe_{1-x}Te_x$ oxypnictides could be a timely feedback to the theoretical models for correlating structure, magnetism and superconductivity in these materials.

In this chapter we present the local structural studies on the $FeSe_{1-x}Te_x$ compounds as a function of Te content and temperature by X-ray spectrosocpy. X-ray absorption is a fast ($\sim 10^{-15}s$) and site selective method, that investigate the short/medium range order and electronic structure of materials [139]. Extended X-ray absorption fine structure (EXAFS) provides information on the local atomic distribution around a selected absorbing atom through photoelectron scattering [15]; on the other hand, X-ray absorption near-edge structure (XANES) spectroscopy probes the distribution of the valence electrons in the final states and the local geometry around the selected atom.

In the first section we present the systematic study of the local structure of the $Fe(Se,S)_{1-x}Te_x$ system as a function of temperature. Polarized and unpolarized measurements are performed on $FeSe_{0.25}Te_{0.75}$ single crystal [24] and $Fe(Se,S)_{1-x}Te_x$ [23, 25] powder samples respectively, using a combination of Fe K-edge and Se K-edge EXAFS. We have found that the Fe-(Se,S) and Fe-Te bond lengths in the ternary system are very different from the average crystallographic Fe-(Se,S)/Te distance, and almost identical to the Fe-(Se,S) and Fe-Te distances for the binary Fe(Se,S) and FeTe systems. The mean square relative displacements (MSRDs) show a systematic chnage with Te content, consistent with bond relaxation in the inhomogeneous ternary phases. While the local structure of the $FeSe_{1-x}$ system is consistent with the crystallographic structure, the Se/S and Te atoms do not occupy the same atomic site in the $Fe(Se,S)_{1-x}Te_x$, breaking the

average crystal symmetry. Moreover, the results obtained by polarized EXAFS have revealed anisotropic atomic fluctuations and force constant of the Fe-Se bonds. The observed features are characteristic of ternary random alloys, suggesting a proper consideration should be given to the atomic distribution for describing complex electronic structure of these multi-band Fe-based chalcogenide.

In the second section we present the electronic structural studies of $FeSe_{1-x}Te_x$ systems as a function of Te content. Polarized and unpolarized XANES measurements are performed on $FeSe_{0.25}Te_{0.75}$ single crystal and $FeSe_{1-x}Te_x$ powder samples respectively [27]. An intense Fe K-edge pre-edge peak due to Fe $1s \rightarrow 3d$ (and admixed Se/Te p states) is observed, showing substantial change with Te substitution and x-ray polarization. The main white line peak in the Se K-edge XANES due to Se $1s \rightarrow 4p$ transition appears similar to the one expected for Se^{2-} systems and changes with Te substitution. Polarization dependence reveals that unoccupied Se orbitals near the Fermi level have predominant $p_{x,y}$ character. Fe $L_{2,3}$-edge x-ray absorption spectroscopy has been used to study the electronic structure of $FeSe_{1-x}Te_x$ chalcogenides. The spectra are quite similar to those for the metallic Fe and Fe-based pnictides, consistent with weak correlation effects in the chalcogenides. A systematic change in the experimental spectra with Te substitution is observed and well reproduced by cluster calculations [26]. A combined experimental and theoretical analysis reveals decreased hybridization of Fe *3d* and chalcogen p states with increasing Te concentration, which could be important for the superconductivity and magnetism of the chalcogenides.

The chapter is organized as follow: for each section we report first the experimental details, then we present the obtained results and finally we discuss their implicaction.

4.1 Effect of Te substitution on the local structure of FeSe system

In this section we have used extended x-ray absorption fine structure EXAFS to probe the local structure of $Fe(Se,S)_{1-x}Te_x$ system. For this purpose, we have combined Se and Fe K-edge EXAFS as a function of temperature. X-ray absorption measurements were performed on powder samples of $FeSe_{1-x}Te_x$ (x=0, 0.50, 0.75 and 1.0) and $FeSe_{0.2}Te_{0.8}$. Polarized EXAFS spectra are acquired on $FeSe_{0.25}Te_{0.75}$ single crystal. The superconducting, structural and transport properties of the samples are well characterized [81]. The X-ray absorption measurements were made at different beamlines:

- *Se K-edge EXAFS measurements:* **BM29** beamline of the European Synchrotron Radiation Facility ESRF, Grenoble, using a double crystal Si(311) monochromator; the EXAFS measurements are performed on $FeSe_{0.88}$ and $FeSe_{0.5}Te_{0.5}$ powder samples and $FeSe_{0.25}Te_{0.75}$ single crystal. A continuous flow He cryostat was used to cool the samples with a temperature control within an accuracy of $\pm 1K$.

- *Fe K-edge EXAFS measurements:* **BM29** beamline of the European Synchrotron Radiation Facility ESRF, Grenoble, using a double crystal Si(311) monochromator; the EXAFS measurements are performed on $FeSe_{0.88}$ and $FeSe_{0.5}Te_{0.5}$ powder samples and $FeSe_{0.25}Te_{0.75}$ single crystal. A continuous flow He cryostat was used to cool the samples with a temperature control within an accuracy of $\pm 1K$. **BM30B** beamline of the European Synchrotron Radiation Facility ESRF, Grenoble, using a double crystal Si(220) monochromator; the polarized EXAFS measurements are performed on $FeSe_{0.25}Te_{0.75}$ single crystal, while on $FeSe_{1-x}Te_x$ (with x=0, 0.25, 0.5 and 1) and $FeSe_{0.2}Te_{0.8}$ powder samples we have acquired unpolarized EXAFS spectra. A continuous flow He cryostat was used to cool the samples with a temperature control within an accuracy of $\pm 1K$.

The Se K-edge absorption spectra were recorded by detecting the Se Kα fluorescence photons, while Fe Kα fluorescence photons were collected over a large solid angle using multi-element Ge-detector for measuring the Fe K-edge absorption. As a routine experimental approach, several absorption scans were collected to ensure the reproducibility of the spectra, in addition to the high signal to noise ratio [131, 132]. Standard procedure was used to extract the EXAFS from the absorption spectrum.

4.1.1 Evidence of local structural inhomogeneity in $FeSe_{1-x}Te_x$

The information obtained by diffraction techniques on the average ordered structure of $FeSe_{1-x}Te_x$ is not enough to explain the basic electronic properties and the knowledge of the local structure gets prime importance. For this reason, temperature-dependent x-ray absorption measurements were performed in transmission mode on powder samples of $FeSe_{0.88}$ and $FeSe_{0.5}Te_{0.5}$[23].

Figure 4.1.1.1 shows representatives of Fourier transform FT magnitudes of the Se K-edge (k range 3–18Å^{-1}) and Fe K-edge (k range 3–17Å^{-1}) EXAFS oscillations, measured on $FeSe_{0.88}$ and $FeSe_{0.5}Te_{0.5}$ samples, providing partial atomic distribution around the Se and Fe, respectively. The structure of $FeSe_{0.88}$ and $FeSe_{0.5}Te_{0.5}$ has tetragonal symmetry at room temperature. For the earlier, a structural transition to an orthorhombic phase appears below 100 K [61, 67, 53]. For the Se site probed by Se K-edge, there are four Fe near neighbors at a distance 2.4 Å main peak at 2 Å. The next-nearest neighbors of Se are eight Se(Te) and four Fe atoms. Contributions of these distant shells appear mixed, giving a multiple structured peak at 3.0–4.5 Å upper panel. On the other hand, for the Fe site probed by Fe K-edge the near neighbors are four Se(Te) at a distance 2.4 Å and four Fe atoms at a distance 2.6 Å, giving a two-peak structure at 1.5–3.0 Å (Fig. 4.1.1.1, lower panel, with peaks at longer distances corresponding to longer bond lengths). Differences in the local structure of two samples can be well appreciated in both Se K and Fe K-edge data with the FTs appearing very different for the two samples. We will start our discussion on the Se K-edge since first shell EXAFS due to Se-Fe bonds is well separated from the distant shells unlike the Fe K edge EXAFS in which the contribution of the Fe neighbors Se/Te and Fe appear mixed. From the FT itself one can appreciate that the Se-Fe bond lengths in the sample with and without Te are quite similar see, e.g., upper panel of Fig. 4.1.1.1. The Se-Fe EXAFS has been analyzed using a model with a single distance. On the other hand, following the diffraction results,[67, 44, 61, 53, 169] a three shells model was used for the Fe K-edge EXAFS due to Fe-Se(Te) bonds and Fe-Fe bonds. The three shells for the $FeSe_{0.88}$ are four Se at 2.4 Å, and four Fe two each at 2.6 Å and 2.7 Å, and the same for the $FeSe_{0.5}Te_{0.5}$ are two Se and two Te atoms at 2.48 Å and four Fe atoms at 2.52 Å. The number of independent data points: $N_{ind} \sim (2\Delta k \Delta R)/\pi$, where Δk and ΔR are, respectively, the ranges in k and R space over which the data are analyzed [15] were 19 ($\Delta k = 15$Å^{-1} and $\Delta R = 2$Å) and 17 ($\Delta k = 13$Å^{-1} and $\Delta R = 2$Å), respectively, for the Se K-edge single shell fit and the Fe K-edge three shells fit data. Except the radial distances R_i and related mean-square

relative displacements MSRDs, determined by the correlated Debye-Waller factor (σ_i^2), all other parameters were kept constant in the conventional least-squares modeling, using the phase and amplitude factors calculated by FEFF [154] and exploiting our experience on the studies of similar systems [12]. The representative model fits to the Se and Fe K-edge EXAFS in the real and k space are also included in Fig. 4.1.1.1.

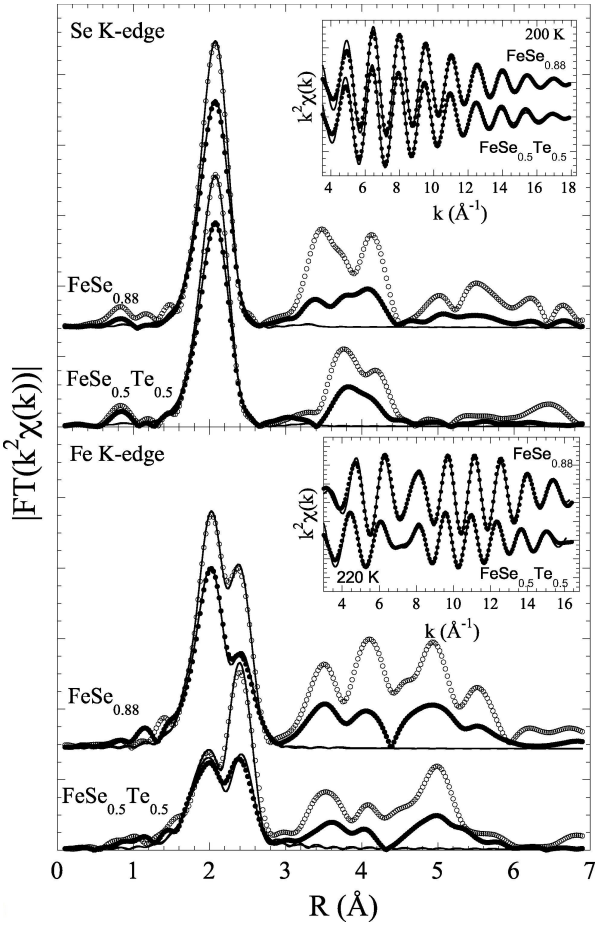

Fig. 4.1.1.1 *FT magnitudes of the Se K-edge upper and Fe K-edge lower EXAFS oscillations at two representative temperatures, measured symbols on $FeSe_{0.88}$ (35 and 200 K) and $FeSe_{0.5}Te_{0.5}$ (35 and 220 K). The model fits are shown as solid lines. The FTs are not corrected for the phase shifts and represent raw experimental data. The peaks amplitudes are lower at higher temperature filled symbols due to increased MSRD. The insets show representative filtered EXAFS symbols with k-space model fits solid line [23].*

Figure 4.1.1.2 shows temperature dependence of the Fe-Se distances determined from the Se and Fe K-edge EXAFS analysis. The Fe-Se distance in $FeSe_{0.5}Te_{0.5}$ is slightly longer, however, the temperature dependence appears similar for the two samples. Other interatomic distances in Fig. 4.1.1.2 inset are also shown with Fe-Fe distance for the $FeSe_{0.88}$, revealing a small splitting across the structural phase transition at 80 K. It was possible to model the data with a single Fe-Fe distance below the structural phase transition, however, inclusion of the two distances, consistent with the diffraction data [44, 61, 67, 53, 169], improved the fit index by about 30%. On the other hand, Fe-Te distance for the $FeSe_{0.5}Te_{0.5}$ appears only slightly shorter than Fe-Te distance for the binary FeTe [61]. It is interesting to note that, while the local Fe-Se distance for the $FeSe_{0.88}$ is consistent with the average diffraction distance [44, 67, 169] the one for the $FeSe_{0.5}Te_{0.5}$ is substantially shorter than the average Fe-Se/Te distance (Fig. 4.1.1.3).

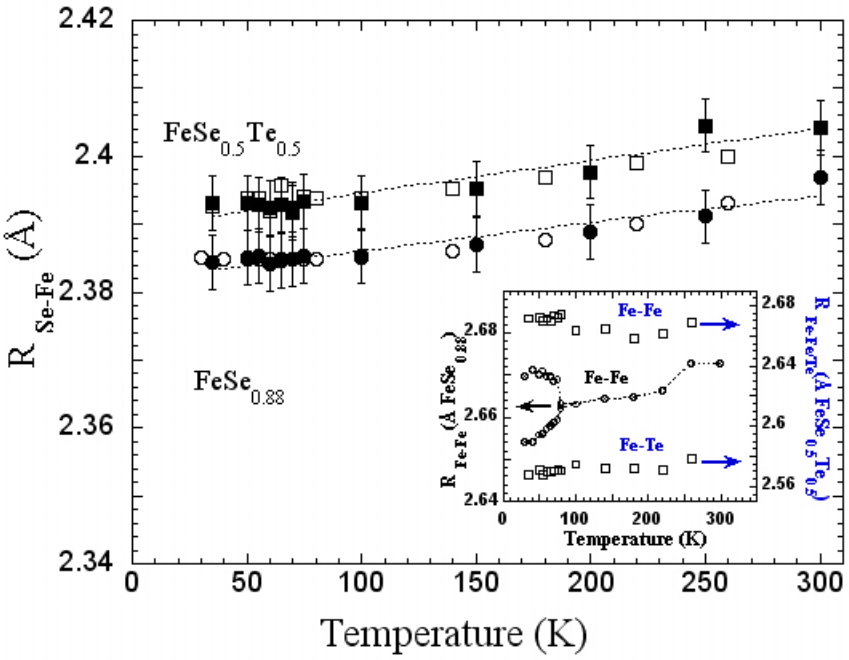

Fig. 4.1.1.2 *Temperature dependence of the local Fe-Se bond length upper panel, determined by Se K-edge open symbols and Fe K-edge filled symbols for the $FeSe_{0.88}$ circles and $FeSe_{0.5}Te_{0.5}$ squares. The inset shows Fe-Fe and Fe-Te distances for the two samples.*

Indeed, the local Fe-Se distance for the $FeSe_{0.5}Te_{0.5}$ is quite similar to the Fe-Se distance in the $FeSe_{0.88}$. Also, the local Fe-Te distance in the $FeSe_{0.5}Te_{0.5}$ is only slightly shorter than the average Fe-Te distance for the binary FeTe system [61, 67, 53]. The fact that the

local Fe-Se Fe-Te distance in the $FeSe_{0.5}Te_{0.5}$ is almost equal or only slightly longer shorter than the Fe-Se Fe-Te distance for the $FeSe_{0.88}$ FeTe system and much shorter longer than the average Fe-Se/Te crystallographic distance, implies that there should be a distribution of the Fe-chalcogen distances at the local scale with Se and Te atoms sitting at different distances from the Fe atoms.

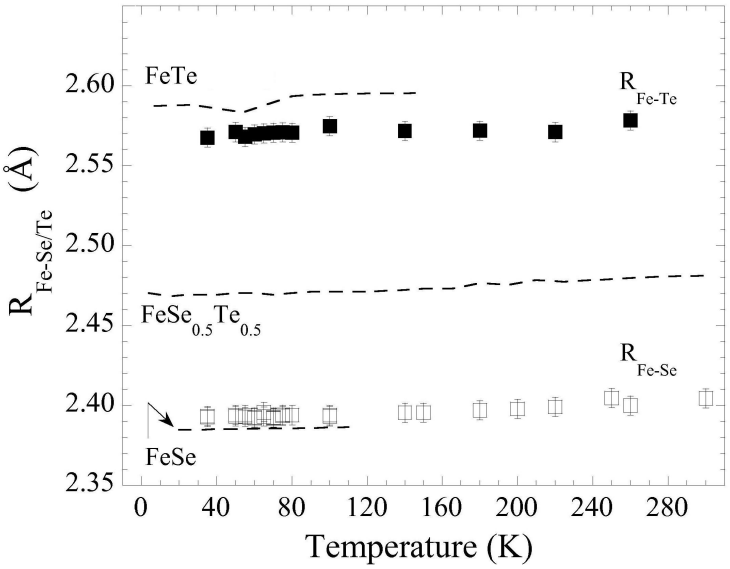

Fig. 4.1.1.3 *The local Fe-Se open squares and Fe-Te distances for the $FeSe_{0.5}Te_{0.5}$ are compared with the average diffraction distances dashed lines in the lower panel. The average Fe-Te distance in the FeTe system and Fe-Se distance in the FeSe system, are also included. The uncertainties represent average errors, estimated by the standard EXAFS method using correlation maps.*

This observation not only underlines diverging local structure from the average one for the Te substituted sample but also constructs a clear evidence for an inhomogeneous distribution of the Fe-Se and Fe-Te bonds and different active electronic components in the chalcogenides.

Figure 4.1.1.4 shows the MSRD σ_i^2 of the Fe-Se pair, describing distance-distance correlation function correlated Debye- Waller factors. The EXAFS Debye-Waller factors distance broadening are different from those measured by diffraction mean-square displacements, i.e., σ_{Fe}^2 and σ_{Se}^2 . The MSRD is sum of temperature independent σ_0^2 and temperature-dependent terms [15], i.e.,

$$\sigma_{Fe-Se}^2 = \sigma_0^2 + \sigma_{Fe-Se}^2(T)$$

The MSRD of the Fe-Se pair are well described by the correlated Einstein model [15, 12] with the Einstein temperature $\Theta_E = 300 \pm 20K$, similar for the two samples within the uncertainties, suggesting similar force constant for the Fe-Se bonds in the two samples. The MSRD for the $FeSe_{0.5}Te_{0.5}$ appears to have slightly higher static component indicating higher disorder, consistent with local structural inhomogeneities [12]. It is worth mentioning that, within the experimental uncertainties, consideration of higher order cumulants in the analysis hardly had any influence on the observed MSRD, consistent with negligible deviation from the Gaussian distributions. From the measured Fe-Se/Te and Fe-Fe bond lengths, we can determine the local chalcogen height from the Fe plane h_z. Since the two chalcogen atoms Se and Te occupy two distinct sites in the $FeSe_{0.5}Te_{0.5}$, there are two corresponding h_z, as shown in Fig. 4.1.1.4 inset. The coexisting Fe-chalcogen heights in the ternary system, showing hardly any temperature dependence, are 1.47 ± 0.01Å and 1.75 ± 0.01Å, respectively, for the Se and Te atoms in the crystallographically homogeneous system.

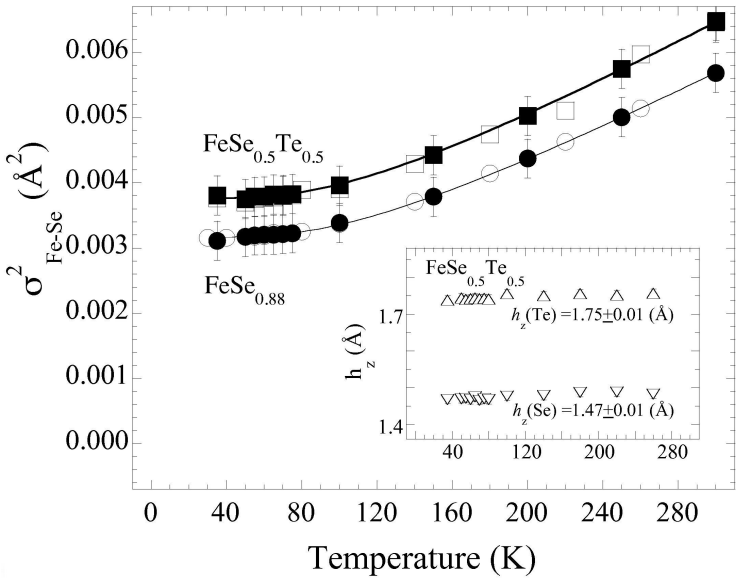

Fig. 4.1.1.4 *Temperature dependence of the Fe-Se MSRD for the $FeSe_{0.88}$ circles and $FeSe_{0.5}Te_{0.5}$ squares, well described by the correlated Einstein model with the Einstein temperature $\Theta_E = 300 \pm 20K$ solid lines. The inset shows local Fe-chalcogen heights h_z in the $FeSe_{0.5}Te_{0.5}$ triangles.*

	Local structure (EXAFS)			Average structure (diffraction)	
	R_{Fe-Se} (Å)	R_{Fe-Te} (Å)	h_z (Å)	$R_{Fe-Se/Te}$ (Å)	h_z (Å)
$FeSe_{0.88}$	2.38		1.47	2.387	1.46
$FeSe_{0.5}Te_{0.5}$	2.39	2.57	1.47(1.75)	2.471	1.60

Table II *Comparison between local and average near-neighbor distances (and chalcogen height) in the* $FeSe_{0.88}$ *and* $FeSe_{0.5}Te_{0.5}$.

The local near-neighbor distances and the Fe-chalcogen heights at a representative temperature T=100 K are shown in Table II for a quantitative comparison with the diffraction data. Since the Fermisurface topology strongly depends on the chalcogen height [14, 114], the results constructs a direct evidence of local electronic inhomogeneity in the ternary $FeSe_{1-x}Te_x$ system, characterized by distribution of Fe-Se/Te bonds and hence Fe-chalcogen heights, consistent with the indications of low-symmetry structure in the Te substituted FeSe by electron [53] and x-ray diffraction [70]. In conclusion, we have studied temperature-dependent local structure of the $FeSe_{1-x}Te_x$ by combined analysis of Se and Fe K edge EXAFS. The Fe-Se Fe-Te bond length for the $FeSe_{0.5}Te_{0.5}$ is found to be much shorter longer than the average Fe-Se/Te, indicating distinct site occupation by the Se and Te atoms and inhomogeneous distribution of the Fe-Se/Te bonds and hence bond angles in a crystallographically homogeneous system.

4.1.2 Determination of the local structure in $FeSe_{0.25}Te_{0.75}$ single crystal by polarized EXAFS

We have used temperature-dependent Se K-edge EXAFS to probe the nearest-neighbour Fe-Se bonds and the related mean square relative displacements (MSRD) using polarization of the X-ray beam parallel and perpendicular to the ab-plane on $FeSe_{0.25}Te_{0.75}$ single crystal [24].

Figure 4.1.2.1 shows the magnitude of Fourier transforms of the Se K-edge EXAFS oscillations (weighted by k^2) measured on the $FeSe_{0.25}Te_{0.75}$ crystal in $E||ab$ and $E||c$ experimental geometries. The first nearest neighbours of the Se are the 4 Fe atoms siting at ~ 2.4Å (peak at ~ 2Å). The next nearest neighbours are the Se atoms, Te atoms and the next Fe atoms and their contributions appear mixed giving a multiple structured peak at $\sim 3.5 - 4.5$Å. There is a clear increase of the Se-Fe peak intensity with decreasing temperature in both polarizations,

however, the Se-Se(Te,Fe) peaks around $\sim 3.5 - 4.5$Å do not show a systematic temperature dependence due to interfering contributions. The local structures in the parallel ($E||ab$) and perpendicular ($E||c$) polarizations appear different, e.g., the $E||ab$ shows a redistribution of the longer distances with clear doubling of the peak $\sim 3.5 - 4.5$Å at lower temperature, unlike the $E||c$ in which the redistribution of these atoms gets narrower by cooling. These observations are a clear indicator of anisotropic and inhomogeneous distribution of the local atomic sites. Here we take a simpler approach to quantify the local structural features and focus only on the nearest-neighbour Se-Fe distribution in the two polarizations.

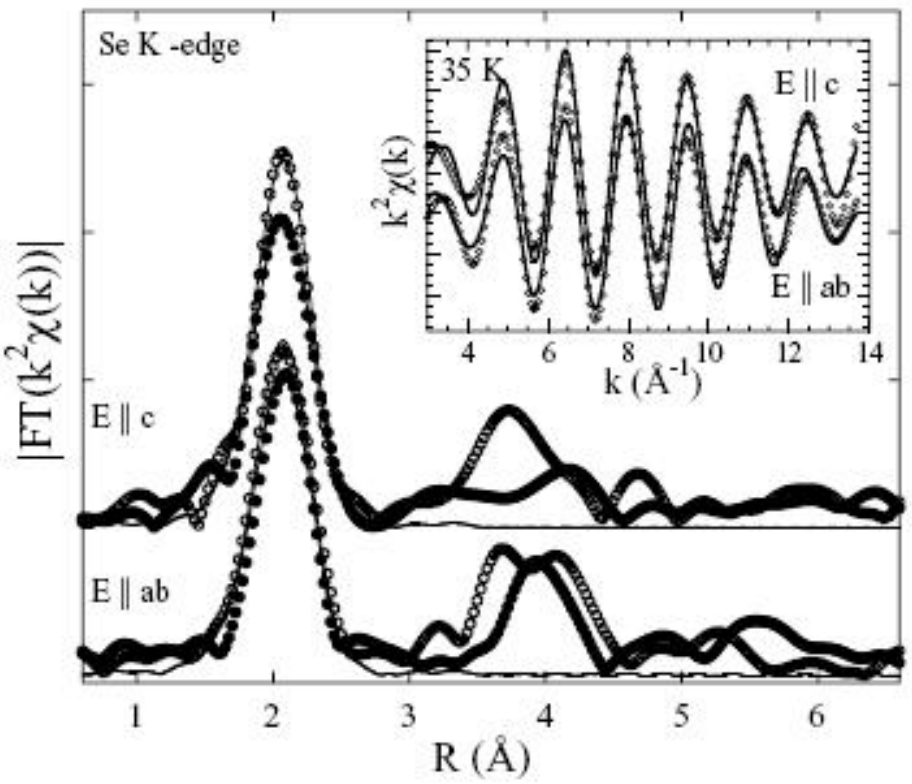

Fig. 4.1.2.1 *Magnitude of the Fourier transforms (FTs) of the Se K-edge polarized EXAFS oscillations measured at 35K (open circles) and 200K (closed circles) in the Eab and Ec polarizations, showing partial and directional atomic distribution around the Se-site in the* $FeSe_{0.25}Te_{0.75}$ *system. The peak at* ~ 2*Å is due to the Fe-Se bonds, while the multiple peaks structure around* $\sim 3.5-4.5$*Å contains contributions of the Se- Se, Se-Te and Se-Fe bonds. Filtered Se-Fe EXAFS with a model fit (solid line) is shown as inset. The model fit is also included in the R-space (solid line) [24].*

We have analyzed the EXAFS data considering a single Fe-Se bond distance for the first coordination shell (well separated from the longer bond contributions). The number of independent data points, $N_{ind} \sim (2\Delta k \Delta R)/\pi$, where Δk and ΔR are, respectively, the ranges in k and R space over which the data are analyzed [15] was 15 ($\Delta k = 12\text{Å}^{-1}$ and $\Delta R = 2\text{Å}$) for the Se K-edge single shell fit. Except the radial distances R_i and related mean-square relative displacements MSRDs, determined by the correlated Debye-Waller factor (σ_i^2), all other parameters were kept constant in the conventional least-squares modeling, using the phase and amplitude factors calculated by FEFF [154] and exploiting our experience on the studies of similar systems [12]. Starting parameters were taken from diffraction studies [81]. The representative model fits in the k- and R-space are included in Fig. 4.1.2.1. The uncertainties in the derived parameters were estimated by the method in which the quality of the fit parameter, proportional to the statistical χ^2, is determined as a function of the concerned parameter (R and the σ^2). Furthermore, correlation maps were used to establish fractional increase of χ^2above its minimum value to estimate the average uncertainties. Figure 4.1.2.2 shows the local Fe-Se distances as a function of temperature, determined by EXAFS of Se-Fe measured in the E||ab and E||c polarization geometries. The Fe-Se distances were found to be equal in the two polarizations and show similar temperature dependance within the experimental uncertainties. The Se-Fe distance, which is less covalent than the Fe-As bonds in the pnictides [16, 81, 114], appears to show a small increase due to thermal expansion of the unit cell. It is interesting to note that the Fe-Se distance ($\sim$ 2.39Å) is substantially shorter than the Fe-Se(Te) distance ($\sim$ 2.52Å) determined by diffraction experiments (see, e.g., the lower panel). Indeed, the Se-Fe distance measured by EXAFS is quite similar to the Fe- Se distance for the binary FeSe system rather than for a Te-substituted $FeSe_{0.25}Te_{0.75}$ system. To ascertain the observed results, we decided to measure the local structure around the iron site using Fe K-edge EXAFS. Figure 4.1.2.3 shows magnitude of Fourier transforms of the Fe K-edge EXAFS oscillations, measured at 15K in the two polarizations representing the E||ab and E||c geometries of the $FeSe_{0.25}Te_{0.75}$ crystal.

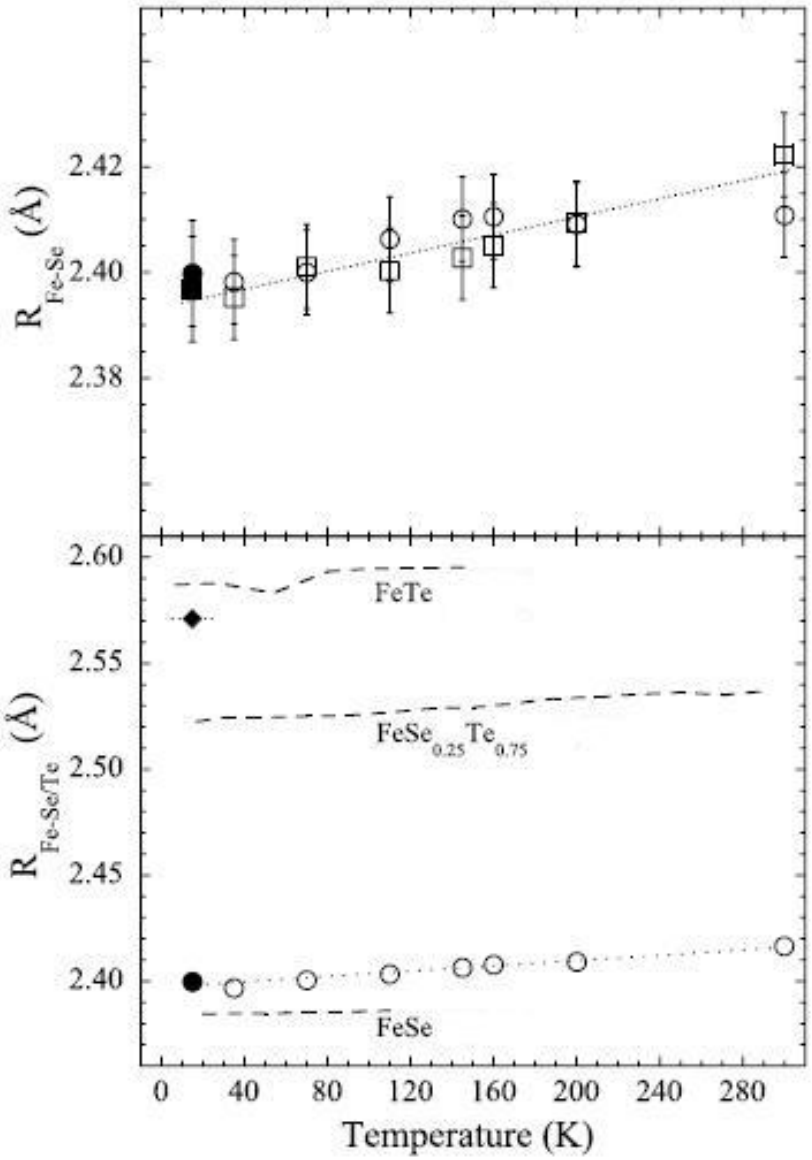

Fig. 4.1.2.2 *Temperature dependence of the local Se-Fe bond length determined by the polarized EXAFS for the $FeSe_{0.25}Te_{0.75}$ single crystal (upper panel). The distances determined in the E//ab polarization (circles) and E//c polarization (squares) are shown. The lower panel shows a comparison between the local Fe-Se distance (circles) in the measured sample with the average crystallographic Fe-Se/Te distances (dashed lines) different samples. The empty symbols correspond to the results of Se K-edge EXAFS while the filled symbols represent the results of Fe K-edge EXAFS analyses. The Fe-Te distance measured by the Fe K-edge is also included (filled diamond).*

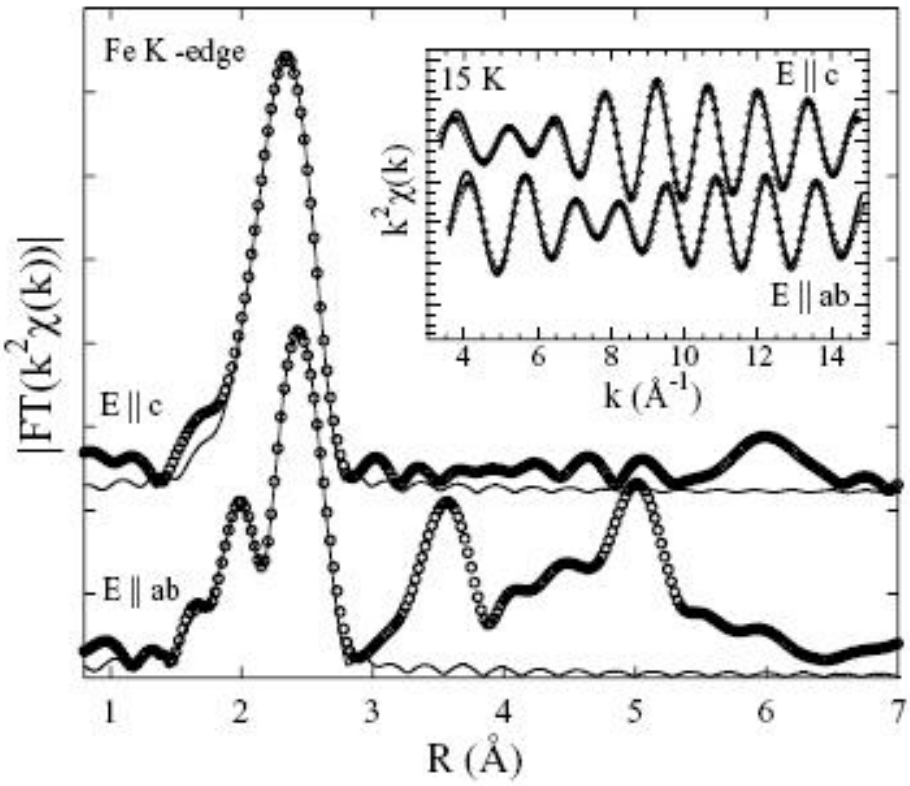

Fig. 4.1.2.3 *Magnitude of the Fourier transforms ($k_{min} = 3\AA^{-1}$ and $k_{max} = 15\AA^{-1}$) of the Fe K-edge polarized EXAFS oscillations measured at 15K (open circles) on the $FeSe_{0.25}Te_{0.75}$ representing the E//ab and E//c polarizations. The model fit in the R-space is also shown (solid line). Filtered EXAFS ($R_{min} = 1.1\AA$ and $k_{max} = 3.1\AA^{-1}$) and model fits in the k-space are shown as inset.*

Unlike the Se site structure, the crystallographic Fe site in the $FeSe_{0.25}Te_{0.75}$ has four nearest-neighbours Se(Te) atoms at ~ 2.5Å and the next four Fe atoms at ~ 2.7Å in the E||ab polarization with the Fe-Fe contribution being masked in the E||c geometry. Therefore, while the the contributions of Fe-Se, Fe-Te and Fe-Fe appear mixed in the E||ab polarization, the contributions of Fe-Se and Fe-Te contribute to the E||c main peak in the Fourier transform. Following the similar procedure as of Se K-edge EXAFS, the Fe K-edge was modelled by three distances (Fe-Se, Fe-Te and Fe-Fe) in the E||ab geometry and by two distances (Fe-Se and Fe-Te) in the E||c polarization. The model fits in the k- and R-space are included in Fig. 4.1.2.3. The Fe-Se distance (~ 2.4Å), determined by the Fe K-edge in the two polarizations are consistent with

what has been found by the Se K-edge EXAFS (see, e.g., Fig. 4.1.2.2). In addition, the Fe-Te distance, determined by the Fe K-edge EXAFS, is found to be ~ 2.56Å, slightly lower than the crystallographic Fe-Te distance in a binary FeTe system. It should be recalled that the Fe-Te distance (~ 2.6Å) in a binary FeTe system is much longer than the Fe-Se distance (~ 2.4Å) in a binary FeSe system. The fact that the Fe-Se distance in the $FeSe_{0.25}Te_{0.75}$ is almost equal to the Fe-Se distance for a binary FeSe system (however, much shorter than the Fe-Se(Te) crystallographic distance), and Fe-Te distance is only slightly lower than the one for a binary FeTe system, there should be a distribution of the Fe-Se(Te) distances at a local scale with Se and Te atoms sitting at different distances from the Fe atoms (i.e., the Se and Te occupy distinctly different sites). This observation not only underlines diverging local structure from the average one, but also constructs a clear and compelling evidence for inhomogeneous distribution of the iron-chalcogen bonds in the $FeSe_{1-x}Te_x$ system.

Figure 4.1.2.4 shows the temperature dependence of the Fe-Se mean square relative displacements (MSRD), determined by the correlated Debye-Waller factor (σ^2) in the two polarizations using Se and Fe K-edge EXAFS. In both polarizations the temperature dependence of the σ^2 can be described by the correlated Einstein model [12, 15]. The σ^2 of the Fe-Se in the E||ab appears slightly higher than the one in the E||c, and the two Einstein temperatures are slightly different (the Einstein temperatures were found to be $\sim 280 \pm 20K$ and $260 \pm 30K$, respectively, in the ab and c directions). The difference between the σ^2 along the two crystallographic directions (albeit small) appears real and consistently observed in the local structure measured by Se and Fe K-edges (data obtained on BM29 and BM30B), revealing anisotropic atomic fluctuations and force constant of the Fe-Se bonds.

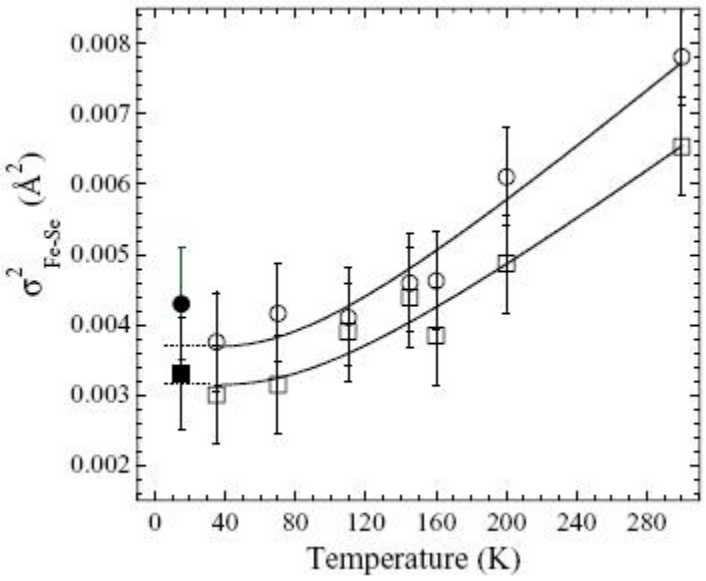

Fig. 4.1.2.4 *Temperature dependence of the mean square relative displacement (MSRD) of the Fe-Se pair in the $FeSe_{0.25}Te_{0.75}$ single crystal, measured with the polarization parallel to the ab-plane (circles) and the c-axis (squares). The solid lines represent correlated Einstein model fits with Einstein temperature $280 \pm 20K$ and $260 \pm 30K$, respectively, in the ab and c polarizations. The error bars correspond to the average uncertainties estimated using correlation maps. Empty and filled symbols correspond to the results of Se and Fe K-edge EXAFS, respectively.*

Although, the anisotropic distribution of Fe-Se displacements is consistent with local inhomogeneities, however, more work is needed to establish such an anisotropy. Having established that the local structure of the ternary $FeSe_{0.25}Te_{0.75}$ system is different from its average crystallographic structure, let us discuss possible implications of this observed local inhomogeneity characterized by distinct Se and Te sites occupation. From the measured local bond lengths, we have determined the Se and the Te heights from the Fe-plane (h_z), found to be 1.47 ± 0.01Å and 1.75 ± 0.01Å, respectively, for the two atoms at 15 K [23]. Recently, electron diffraction data have indicated domain structures in the FeSe(Te) system [53] followed by two crystallographic studies [70, 174] revealing different site occupation for the Se and Te. Also pump and probe experiments [173] have suggested possibility of inhomogeneous electronic components in iron pnictides as in the cuprates. Therefore the present findings are consistent with locally inhomogeneous structure and our earlier work revealing inhomogeneous charge distribution characterized by different local structural configurations [12] in the cuprates. Thus the local structural inho-

mogeneity should have important role in the superconducting and magnetic properties of the new Fe-based materials as of the cuprates. In summary, we have determined local structure of the $FeSe_{0.25}Te_{0.75}$ single crystal by polarized EXAFS measurements. The local Fe-Se bond is found to be anomalously shorter than the average one, indicating distinct site occupation for the Se and Te. This is a direct evidence of broken crystal symmetry due to inhomogeneous local atomic distribution. The results are consistent with local structural inhomogeneity and different electronic components in the chalcogenides, having direct implication on their fundamental electronic states near the Fermi level [105, 114, 115, 116, 14].

4.1.3 Random alloy-like local structure of $Fe(Se,S)_{1-x}Te_x$ superconductors revealed by EXAFS

In order to make a systematic and consistent comparison between different samples treated equally, we have used Fe K-edge EXAFS on a series of $FeSe_{1-x}Te_x$ (x=0, 0.50, 0.75 and 1) and $FeS_{0.2}Te_{0.8}$ chalcogenides [25].

Figure 4.1.3.1 shows Fourier Transforms (FTs) of the EXAFS signals (at representative temperatures) providing real space partial pair distribution function (PDF) around the Fe atom. The FTs are performed in the k-range of $3.5 - 17.5\text{Å}^{-1}$ using a Gaussian window and corrected for the phase shifts.

The main FT peak at 2-3Å contains contribution from the Fe-Ch (Ch=Se, S, Te) distances (~ 2.4Å) and Fe-Fe distance (~ 2.7Å). The next neighbours appear at longer distances and their contributions are well separated from the contributions of the Fe-Ch and Fe-Fe. The feature between 3-4Å is due to Fe-Fe distances (~ 3.8Å), while the peak features appearing in the range of 4-5.5Å contain contributions from longer Fe-Ch bonds, Fe-Fe bonds and the multiple scatterings involving different near neighbours of the Fe atoms. The longer distance FT peaks ($R \geq 3$Å) for the ternary systems are much weaker than the ones for the binary FeSe due to more interfering contributions in the earlier. Also, the difference between the Fe-Se and Fe-Fe bonds (in the FeSe) is much larger than the difference between Fe- Te and Fe-Fe (in the FeTe), and hence the stronger damping of the signal due to longer distances for the FeTe is likely. In addition,an apparent shift of the main peak towards longer distance is merely due to increased average Fe-Ch distance with increasing Te concentration.

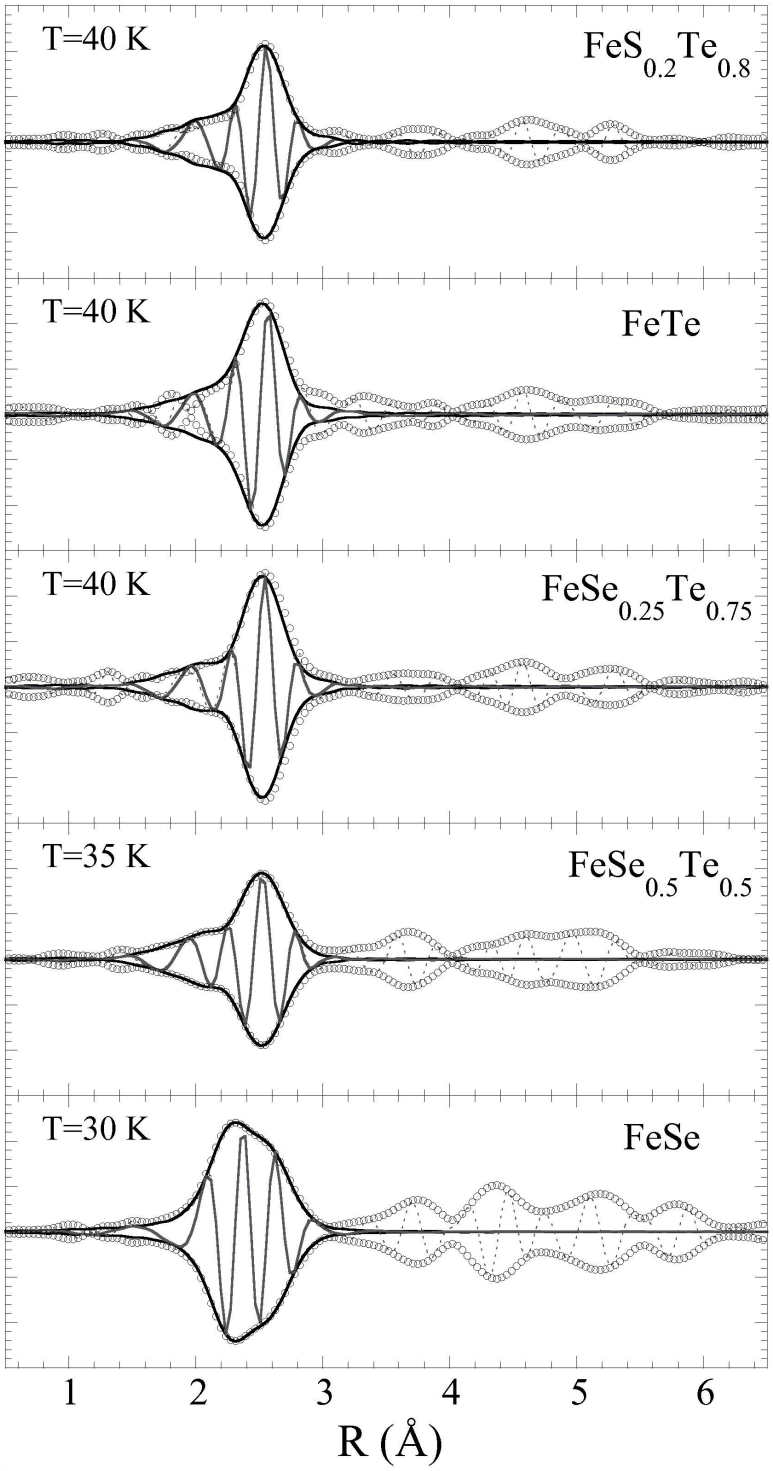

Fig. 4.1.3.1 *Experimental Fourier transform magnitudes including real parts (weighted by k^2) are shown at a representative temperatures with the model fits (solid lines) on $FeSe_{1-x}Te_x$ (x=0, 0.50, 0.75 and 1) and $FeS_{0.2}Te_{0.8}$ powder samples [25].*

In this work we focus only on the Fe-Ch and Fe-Fe near neighbour bondlengths and the related mean square relative displacements (MSRDs). The structure of the FeTe and FeSe binary systems is tetragonal at room temperature, becoming monoclinic and orthorombic respectively at lower temperatures [61, 67]. However, in order to limit the number of parameters we do not consider split Fe-Fe distances arising from the breaking of the tetragonal symmetry, as the splitting is too small to be appreciated, and the effect of the splitting should appear in the MSRDs. In the $FeSe_{1-x}Te_x$ and $FeS_{0.2}Te_{0.8}$ ternary systems, the structural transitions are suppressed. Therefore, while a two shells (Fe-Se and Fe-Fe for the FeSe, Fe-Te and Fe-Fe for the FeTe) model is used for the binary systems, a three shells (Fe-Se/Fe-S, Fe-Te and Fe-Fe) model was necessary to describe the near neighbour local structure around the Fe atom in the ternary systems. For the EXAFS model fits, we have used EXCURVE 9.275 code [126] with calculated backscattering amplitudes and phase shift functions. Similar results were obtained when WINXAS package [153] was used with backscattering amplitudes and phase shifts calculated using FEFF [154]. Only the radial distances Ri and the corresponding MSRDs σ_i^2, were allowed to vary in the least squares model fits, while all other parameters (E_0, N_i and S_0^2) were kept fixed for the study as a function of temperature. The input for the structural model was taken from diffraction studies [67, 61, 81]. The number of independent data points, $N_{ind} \sim (2\Delta k \Delta R)/\pi$ [15] were about 22 ($\Delta k = 14\text{Å}^{-1}$ and $\Delta R = 2.6\text{Å}$), in the four parameters (six parameters) fits for the binary (ternary) systems. The model fits are also included in Fig. 4.1.3.1. The uncertainties were determined by creating correlation maps with appropriate contour level being established by modeling different scans.

Figure 4.1.3.2 shows temperature dependence of the near neighbour local bondlengths determined by the Fe K-edge EXAFS. The Fe-Se and Fe-Te distances in the ternary $FeSe_{1-x}Te_x$ system are quite similar to the Fe-Se and Fe-Te distances in the FeSe and FeTe respectively, showing hardly any change with temperature. Also, the Fe-S and Fe-Te bond lengths in $FeS_{0.2}Te_{0.8}$ are close to the respective binaries (the Fe-S bond turns out to be almost 0.4Å shorter than the Fe-Te). In fact, the Fe-S distance is $\sim$ 2.22Å, close to the known distance ($\sim$ 2.23Å) in the FeS binary system [188]. The results are also consistent with recent high resolution neutron diffraction results on a series of $FeSe_{1-x}Te_x$ compounds [189].

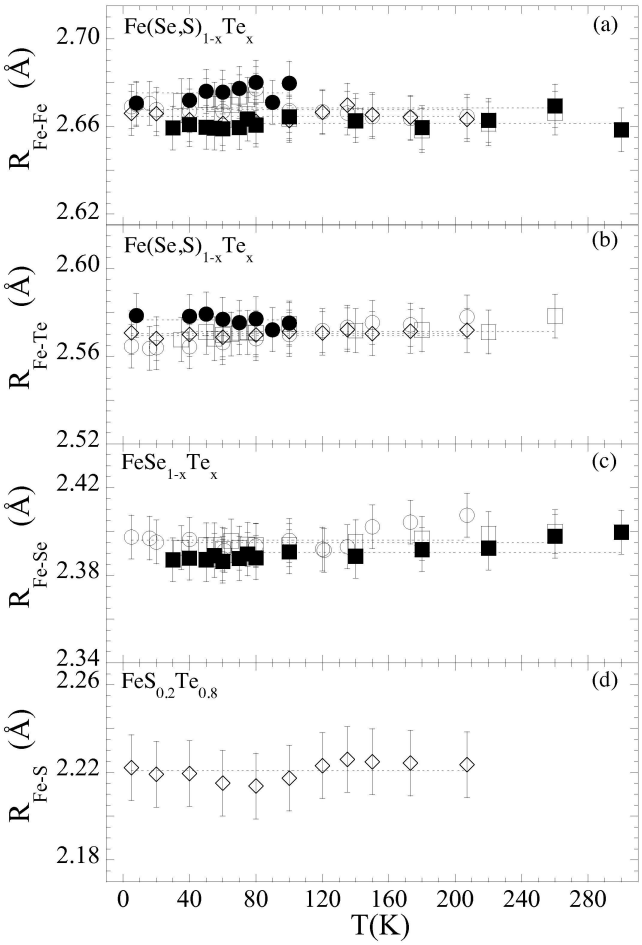

Fig. 4.1.3.2 *Near neighbour distances from the Fe for the $FeSe_{1-x}Te_x$ ($0 \leq x \leq 1$) and $FeS_{0.2}Te_{0.8}$ samples as a function of temperature. The open symbols correspond to the ternary systems and the filled symbols are due to binary FeSe (filled squares) and FeTe (filled circles). The open squares represent the data on the $FeSe_{0.5}Te_{0.5}$ while open circles correspond to the ternary $FeSe_{0.25}Te_{0.75}$. The Fe-Fe distance (panel a) remains temperature independent, however, it shows a small change with changing Te concentration. The Fe-Te (panel b) and Fe-Se (panel c) bondlengths in the $FeSe_{1-x}Te_x$ ternary are quite similar to the one in respective binary FeSe and FeTe. Also, the Fe-Te (panel b) and Fe-S (panel d) distances in the $FeS_{0.2}Te_{0.8}$ (open diamonds) are different, consistent with local structural inhomogeneity. The error bars represent maximum uncertainty, determined using correlation maps between different parameters.*

Nevertheless, what appears to be clear is that the chalcogen atom locations in the ternary systems are significantly displaced from the average crystallographic sites, i.e., the crystal

is composed of a mixture of well defined long and short Fe-Ch bonds. Therefore, the local symmetry is broken in the crystallographically homogeneous system. This is different from the average structure measurements, showing a continuous evolution of the mean Fe-Ch distance as a function of the Te substitution. The mean Fe-Ch distances (weighted average) measured by the EXAFS are consistent with the average bondlengths measured by diffraction (Fig. 4.1.3.3), however, the local and average structures are different for the ternary chalcogenides. On the other hand, the Fe-Fe distance (see e.g.,Fig. 4.1.3.2a), describing the in-plane lattice parameter, appears to show a small variation (increase with increasing Te concentration), however, the change is smaller than what has been seen by diffraction [81].

Figure 4.1.3.4 compares near neighbour local Fe-Se and Fe-Te distances in the $FeSe_{1-x}Te_x$ ternary as a function of Te concentration. Within the experimental uncertainties the bond lengths appear to remain unchanged, albeit tending to increase with Te concentration, this is likely due to strain relaxation atomic distribution in the inhomogeneous phase [190].

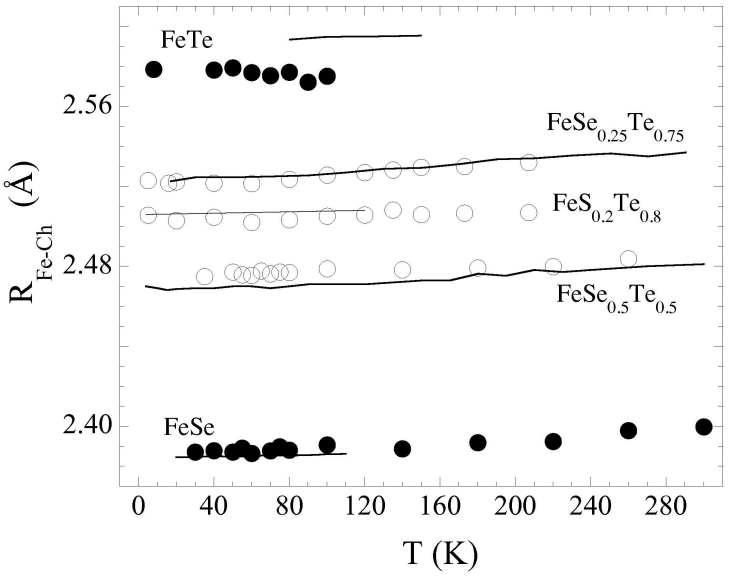

Fig. 4.1.3.3 *Mean Fe-Ch distances (weighted average) determined by EXAFS (symbols) and average distances known from the diffraction (solid lines) are compared. The distances measured by two techniques are found to be consistent with each other.*

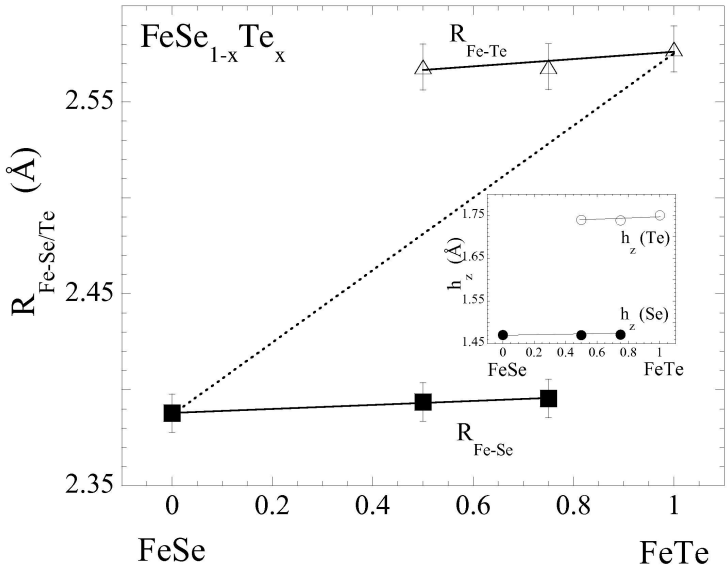

Fig. 4.1.3.4 *Near neighbour distances Fe-Se (lower) and Fe-Te (upper) as a function of Te concentration in the $FeSe_{1-x}Te_x$ at low temperature ($T \leq 80K$). The dashed line is the average Fe-Ch distance, consistent with the diffraction measurements. The inset shows chalcogen heights from the Fe square plane.*

Figure 4.1.3.5 shows the MSRDs (σ^2) of the Fe-Ch (Fe-Se and Fe-Te) pairs as a function of temperature for the $FeSe_{1-x}Te_x$ ternary system. The EXAFS Debye Waller factors (distance broadening) is sum of temperature independent (σ_0^2) and temperature dependent terms, i.e.

$$\sigma^2_{Fe-Ch} = \sigma_0^2 + \sigma^2_{Fe-Ch}(T)$$

Generally a correlated Einstein (or Debye) model is used to describe the temperature dependent MSRDs ($\sigma^2(T)$) extracted by EXAFS experiments [15]. While the Einstein model uses local optical modes with a well-defined frequency, one has to integrate over the vibrational density of states (VDOS) including acoustic modes in the Debye model. However, In the harmonic and single scattering approximation the simplest model to describe the temperature dependence of MSRDs is the correlated Einstein model, and the difference between the two models is generally smaller than the experimental and theoretical uncertainties in the low temperature regime [191, 192].

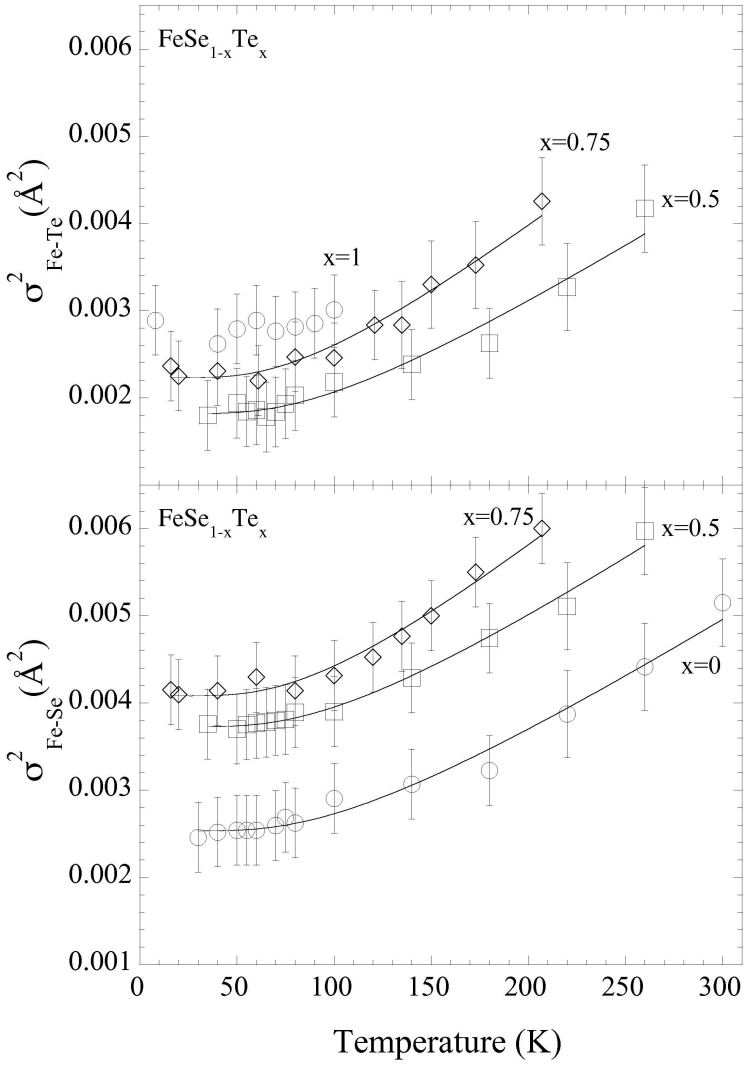

Fig. 4.1.3.5 *Temperature dependence of the Fe-Se (lower) and Fe-Te (upper) MSRDs for the $FeSe_{1-x}Te_x$ system. The solid lines represent the correlated Einstein model fits to the data. The Einstein-temperatures, Θ_E, for the Fe-Se bonds are about 320 K, 310 K and 280 K respectively for the FeSe, $FeSe_{0.5}Te_{0.5}$ and $FeSe_{0.25}Te_{0.75}$ samples. The σ_0^2 for the FeSe sample is small ($\sim 0.0002\mathring{A}^2$) while that for the ternary ($FeSe_{0.5}Te_{0.5}$ and $FeSe_{0.25}Te_{0.75}$) systems are almost similar, albeit much higher ($\sim 0.0014\mathring{A}^2$), consistent with a significant static disorder due to local inhomogeneity in the ternary system. On the other hand, the Einstein-temperatures, Θ_E, for the Fe-Te bonds are about 290 K and 260 K respectively for the $FeSe_{0.5}Te_{0.5}$ and $FeSe_{0.25}Te_{0.75}$ samples (the maximum uncertainty is about $\pm 20K$). The data on the FeTe sample are not sufficient for Einstein model fits and to extract the Θ_E.*

Here, the temperature dependence is well described by the correlated Einstein model [15, 191, 192], an appropriate approximation considering the temperature range studied here.

The Einstein equation to describe the temperature dependence of the$\sigma^2_{Fe-Se}(T)$ is given as:

$$\sigma^2(T) = \frac{\hbar^2}{2\mu k_B \Theta_E} coth(\frac{\Theta_E}{2T})$$

The Einstein temperature (Θ_E, i.e., the Einstein frequency $\omega_E = k_B\Theta_E/\hbar$) for the Fe-Se pairs tend to decrease with increasing Te concentration, indicating a decreased local force constants ($k = \mu\omega_E^2$, where k is the effective force constant and μ is reduced mass of the Fe-Ch pair) for the Fe-Ch bonds in the ternary systems. Indeed, the estimated Einstein temperatures for the Fe-Se bonds in the FeSe, $FeSe_{0.5}Te_{0.5}$ and $FeSe_{0.25}Te_{0.75}$ were found to be $\sim 320K$, $\sim 310K$ and $\sim 280K$. This is consistent with earlier EXAFS study using Se K-edge, giving an estimation of $\Theta_E = 300K \pm 20K$ for the FeSe and $FeSe_{0.5}Te_{0.5}$ powder samples [23], and $\Theta_E = 280K \pm 20K$ and $260 \pm 20K$ for $FeSe_{0.25}Te_{0.75}$ single crystal samples in two high symmetry directions (ab and c respectively) [24]. On the other hand, the estimated Einstein temperatures for the Fe-Te bonds in the $FeSe_{0.5}Te_{0.5}$ and $FeSe_{0.25}Te_{0.75}$ were found to be$\sim$ $290K$ and $\sim$ $260K$ respectively. Therefore, it appears that the Fe-Ch bond lengths are relatively relaxed in the ternary systems due to coexisting random distribution of the chalcogen atoms.

4.1.4 Summary and conclusions

In this section, we have used extended X-ray absorption fine structure (EXAFS), a fast and site-specific experimental tool [15], to probe the local structure of $Fe(Se,S)_{1-x}Te_x$ system. For this purpose, we have combined Se and Fe K-edge EXAFS as a function of temperature on powder samples of $FeSe_{1-x}Te_x$ (x=0, 0.50, 0.75 and 1.0) and $FeS_{0.2}Te_{0.8}$ and single crystal of $FeSe_{0.25}Te_{0.75}$, to quantify the local interatomic distances and their mean-square relative displacements.

We have found that the Fe-(Se,S) and Fe-Te bond lengths in the ternary system are very different from the average crystallographic Fe-(Se,S)/Te distance, and almost identical to the Fe-(Se,S) and Fe-Te distances for the binary Fe(Se,S) and FeTe systems. While the local structure of the $FeSe_{1-x}$ system is consistent with the crystallographic structure, the Se and Te atoms do not occupy the same atomic site in the $Fe(Se,S)_{1-x}Te_x$, breaking the average crystal symmetry. Moreover, the results obtained by polarized EXAFS have revealed anisotropic atomic fluctuations and force constant of the Fe-Se bonds.

The observed diverging local structure from the average structure in the $Fe(Se,S)_{1-x}Te_x$ ternary systems recalls the case of random alloys. Indeed, the situation is similar to the random alloys of the type $AB_{1-x}C_x$ in which local structure around the A site is not homogeneous although the end members AB and AC are possessing a perfect crystallographic symmetry [193, 194, 195, 196, 197]. Indeed, the bond lengths A-B and A-C are non-equivalent and hence the bond angles are also. These local distortions in the random alloys generally do not lead to new diffraction peaks, and could be explained by random distribution, reflecting lower symmetry of the crystal associated with strain relaxation arrangements of atomic sites. It is clear that the local Fe-Se and Fe-Te bondlengths are closer to those in the binary end members (FeSe and FeTe) than what one expects from the prediction of Vegard's law [190]. Within the experimental uncertainties the bond lengths appear to remain unchanged, albeit tending to increase with Te concentration, this is likely due to strain relaxation atomic distribution in the inhomogeneous phase [190]. Various models have been discussed to describe the atomic-scale structure of the $AB_{1-x}C_x$ random alloys [198, 199, 200, 201]. These studies have predicted the first near neighbor distance between the A and C atoms (d_{AC}) in the dilute limit of an impurity atom C in a crystal AB ($d_{AC}^{AB:C}$). The dimensionless relaxation parameter is defined as the difference between $d_{AC}^{AB:C}$ and the (unperturbed) first near neighbor distance of the host d_{AB}^{0} relative to the difference in

first near neighbor distances of the two binaries, i.e., $\epsilon = (d_{AC}^{AB:C} - d_{AB}^0/d_{AC}^0 - d_{AB}^0)$. In the Pauling limit [190], in which the atomic radii are approximately conserved in different environments, the two bonds will be composition independent and equal to their ideal values d_{AB}^0 and d_{AC}^0, and hence $\epsilon = 1$ (full relaxation). On the other hand, the Vegard's limit [190] corresponds to $\epsilon = 0$ (no relaxation) in which the alloy is thought of sustaining a single (average) chemical bond (i.e., no bond alteration). In the present case of $FeSe_{1-x}Te_x$, the is ~ 0.95, indicating large average bond relaxation, unlike large part of pseudobinary semiconductor alloys in which the relaxation parameter is ~ 0.8 [193, 194, 195, 196, 197]. This could be due to i) stronger Fe d-Ch p hybridization and ii) larger order in the $FeSe_{1-x}Te_x$ chalcogenides in compare to the pseudobinary semiconductor alloys [199, 200].

Let us discuss possible implications of the present study on the fundamental electronic structure of the title system. Low-energy electronic states in the Fe-based superconductors are derived by the five Fe d orbitals with their relative positions modulated by the anion pnictogen or chalcogen height [114, 115, 14]. The anion height controls the Fermi-surface topology which has strong k_z dispersion, through changing degeneracy between different bands in particular, between the $d_{x^2-y^2}$ and d_{xz}/d_{yz}, with a direct implication on the magnetic structure and superconductivity of the Fe-based materials [105, 116]. For example, it has been clearly shown [14] that a , like single stripe magnetic order similar to the Fe pnictides is more favorable in the $FeSe_{1-x}Te_x$, with small Fe-chalcogen height, unlike a $(\pi, 0)$ type double stripe pattern for the FeTe with relatively high Fe-chalcogen height. Therefore, the Fe-chalcogen height seems to control the lowenergy states, correlation effects Coloumb screening through hybridizations, and magnetic order, however, this alone is not able to describe the underlying physics. In the light of the above, the observed local inhomogeneity has strong implication on the physics of the chalcogenides, and in general on the Fe-based superconductors. Indeed, the local inhomogeneity, characterized by coexisting structural configurations with low and high chalcogen heights, can easily reconcile not only the changing magnetic order but also the photoemission experiments on the $FeSe_{1-x}Te_x$ systems [172, 173], debating on surprisingly large effective electron mass and local correlation effects. In addition, the coexisting components can easily modify the Fermi-surface topology and hence the interband scattering and the nesting properties, putting strong constraints on the interpretation of Fermi surface topological effects and theoretical models describing superconductivity in these materials. Earlier, we have widely studied the copper oxide perovskites providing clear evidence

of inhomogeneous charge distribution characterized by different local structural configurations [12]. The fact that, $FeSe_{1-x}Te_x$ system manifest local structural inhomogeneity while the superconducting Tc is higher, provides further indication that the local inhomogeneity should have important role in the new Fe-based materials as well, consistent with recent experiments in favor of mesoscopic phase separation in the Fe-based superconductors [85, 171, 173].

4.2 Effect of Te substitution on the electronic structure of FeSe system

In this section we have used X-ray absorption spectroscopy to probe the electronic structure of unoccupied state in $FeSe_{1-x}Te_x$ chalcogenide. For this purpose, X-ray absorption measurements were performed on powder samples of $FeSe_{1-x}Te_x$ and single crystal of $FeSe_{0.25}Te_{0.75}$. The superconducting, structural and transport properties of the samples are well characterized[81]. The X-ray absorption measurements were made at different beamlines:

- *Se K-edge XANES measurements:* **BM29** beamline of the European Synchrotron Radiation Facility ESRF, Grenoble, using a double crystal Si(311) monochromator; the EXAFS measurements are performed on $FeSe_{0.88}$ and $FeSe_{0.5}Te_{0.5}$ powder samples and $FeSe_{0.25}Te_{0.75}$ single crystal. The Se K-edge absorption spectra were recorded by detecting the Se Kα fluorescence photons.

- *Fe K-edge XANES measurements:* **BM29** beamline of the European Synchrotron Radiation Facility ESRF, Grenoble, using a double crystal Si(311) monochromator; the EXAFS measurements are performed on $FeSe_{0.88}$, $FeSe_{0.5}Te_{0.5}$ and $Fe_{1.08}Te$ powder samples and $FeSe_{0.25}Te_{0.75}$ single crystal. Fe Kα fluorescence photons were collected over a large solid angle using multi-element Ge-detector for measuring the Fe K-edge absorption.

- *Fe $L_{2,3}$-edge XAS measurements:* **BACH** beamline of the Elettra Synchrotron Radiation Facility, Trieste, using total electron yied (TEY) mode. The measurements were performed at room temperature on $FeSe_{0.88}$, $FeSe_{0.5}Te_{0.5}$ and $Fe_{1.08}Te$ polycristalline samples. The samples were cleaned in situ by hard scraping in a pressure better than 5×10^{-10} mbar after being fractured. The energy resolution was about 250 meV for the Fe L-edge measurements.

A continuous flow He cryostat was used to cool the samples with a temperature control within an accuracy of 1 K. As a routine experimental approach, several absorption scans were collected to ensure the reproducibility of the spectra, in addition to the high signal to noise ratio [131, 132]. Standard procedure was used to extract the EXAFS from the absorption spectrum.

4.2.1 Fe and Se K-edge XANES measurements

A combined analysis of Fe and Se K-edge XANES has permitted us to uncover important features of the unoccupied states near the Fermi level. The results underline the importance of the *p–d* hybridization in the Fe-based chalcogenide superconductors [27].

Figure 4.2.1.1 shows normalized Fe K-edge XANES spectra of $FeSe_{1-x}Te_x$ (x = 0.0, 0.5, 1.0) measured at $T = 30K$. The spectra are close to the one for a reference Fe^{2+} standard [135, 138], consistent with the Fe^{2+} state. The general features of the Fe K-edge are similar to those reported for the Fe-based pnictides [135, 138, 175]. The near edge features are marked with A, B, C, D and E.

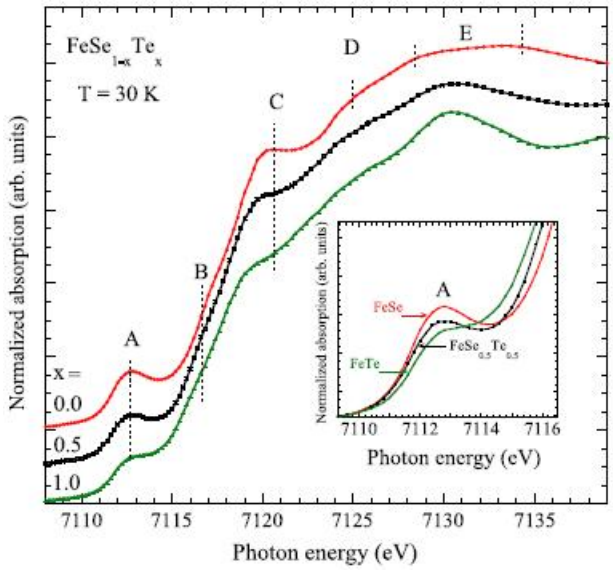

Fig. 4.2.1.1 *Fe K-edge XANES spectra of $FeSe_{1-x}Te_x$ (x=0, 0.5 and 1) measured at 30 K. The inset zooms in over the near edge features A [27].*

The K-edge absorption process is mainly governed by the $1s \rightarrow \epsilon p$ dipole transition and hence continuum states with *p* symmetries (and admixed states) can be reached in the final state. In addition to the dipole transition, a direct quadrupole transition in the unoccupied *3d* states is seen as pre-peak A, mixed with the dipole contribution (mixing with the *4p* states due to local distortions). Therefore, apart from the density of the unoccupied electronic states, a changing pre-edge intensity can be an indicator of a changing local geometry or distortion around the Fe atom. Here, the pre-peak A ($\sim 7111eV$) is due to the $1s \rightarrow 3d$ quadrupole transition, with

some dipole contribution due to the admixed p states. The feature B (shoulder structure of the main absorption jump at $\sim 7117eV$) appears due to the $1s \rightarrow 4p$ transition. The peak like structure C ($\sim 7120eV$) should be driven by the $1s \rightarrow 4p$ states admixed with the d states of the chalcogen atoms. A significant change in the pre-peak A intensity can be seen as a function of Te substitution with the one for the FeSe appearing more intense (see e.g. the inset showing a zoom over the peak A). Similarly, the feature C looks more intense for the FeSe sample due to larger mixing of Fe *4p/chalcogen d* states. The features at higher energies are mainly due to the photoelectron multiple scattering with the nearest neighbours.

For a further clarification on the Fe K-edge spectral features, we have studied the polarization dependence of the XANES measured on a single crystal of a representative $FeSe_{0.25}Te_{0.75}$ sample. Figure 4.2.1.2 shows the Fe K-edge XANES spectra with varying polarization. A significant polarization dependence of Fe K-edge features can be seen. In particular, the pre-peak shows a significant increase from parallel to the almost perpendicular polarization ($E||75^{\circ}$). This indicates an increased density of unoccupied Fe *3d* states admixed with the p states originating from the chalcogen atoms. The polarization dependence appears similar to the one found for the oxypnictides [175].

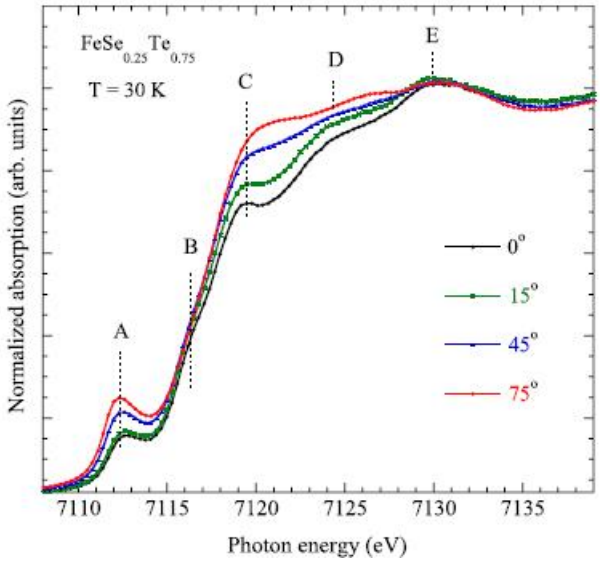

Fig. 4.2.1.2 *Polarized Fe K-edge XANES spectra of $FeSe_{0.25}Te_{0.75}$ measured at 30 K. The 0° correspond to the E||ab while the 75° represent almost the E||c case. A strong polarization effect is evident on the pre-peak A and the peak C.*

The results also appear consistent with the local-density approximation (LDA) calculations for these materials [114]. Similarly, the peak C gets more intense for the perpendicular geometry, mainly due to a higher density of states for *Fe 4p/chalcogen d* hybrid bands along the c-axis. On the other hand, the peak B appears hardly affected by the polarization. The polarization dependence can be understood also in terms of different local geometries of the system in the two directions. Indeed, with the E||ab plane, the Fe– Fe planar orbitals are available for the transition while with E||c, the mixing of the chalcogen p (peak A) and chalcogen d (peak C) is expected to be more prominent. Coming back to the substitution effect (Fig. 4.2.1.1), a clear energy shift can be seen for the features B and the peak C. Indeed, the peak C is shifted by almost 0.8 eV lower energy for the FeTe with respect to the FeSe. Since this peak is derived by the Fe–chalcogen orbitals mixing, any change in the Fe–chalcogen bond length is expected to influence the peak position, related by the $E \propto d^{-2}$ relation for a XANES resonance [134]. The Fe–chalcogen bond length in the FeTe is ≈ 2.6Å, larger than the Fe–chalcogen bond length in the FeSe (≈ 2.4Å). A gradual and substantial decrease of the prepeak (Fig. 4.2.1.1) derived by a $1s \rightarrow 3d$ quadrupole transition and a dipole transition due to admixed chalcogen p states is consistent with the longer Fe–Te distance. On the other hand, an apparent broadening and the shift of the peak C for the $FeSe_{0.5}Te_{0.5}$ should be due to the local inhomogeneity of the ternary system, characterized by coexisting Fe–chalcogen bond lengths [23, 24, 70, 174, 176]. Similarly, the peak B is shifted towards lower energy for the FeTe with respect to the FeSe, merely due to the fact that the Fe–Fe bond length for the FeSe (≈ 2.66Å) is lower than the one for the FeTe (≈ 2.69Å). Following the above arguments we can state that the higher intensity of the pre-peak should be due to higher mixing of the chalcogen p orbitals with the Fe *3d* states consistent with the shorter Fe–chalcogen bond length, and hence the dipole contribution appears to be changing, with a higher number of available unoccupied states for the transition from the Fe *1s* states. It should be mentioned that a sophisticated theoretical model is required for a quantitative estimation of the dipole and quadrupole contribution in the present system with Fe in a tetrahedral geometry.

Figure 4.2.1.3 compares Se K-edge XANES spectra of FeSe and $FeSe_{0.5}Te_{0.5}$ samples measured at T = 30 K. There are two main features, (i) a sharp peak A ($\sim 12658eV$), which is mainly due to a direct $1s \rightarrow 4p$ dipole transition and, (ii) the broad hump B (about 7 eV above the peak A), should be a multiple scattering of the photoelectron with the near neighbours.

The spectra are typical of Se^{2-} systems [177] with the position of the peak A in all the samples being consistent with earlier studies on similar systems.

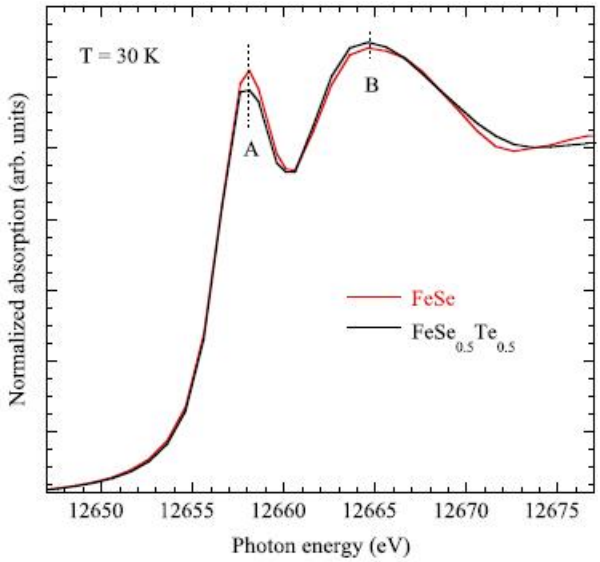

Fig. 4.2.1.3 *Se K-edge XANES spectra of $FeSe_{1-x}Te_x$ (x=0 and 0.5) measured at T=30 K.*

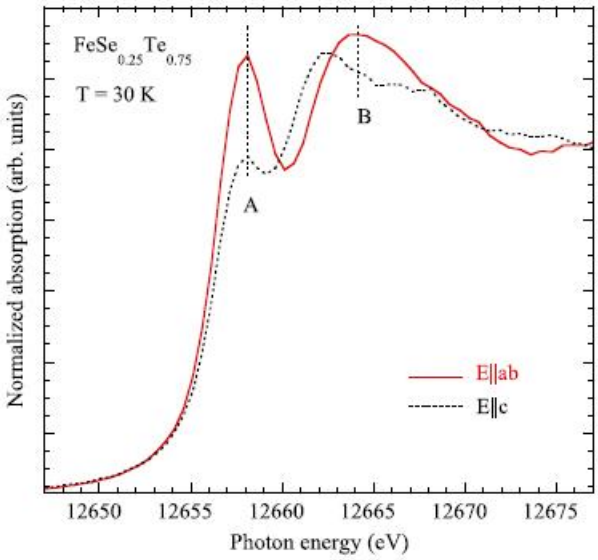

Fig. 4.2.1.4 *Polarized Se K-edge XANES spectra of the $FeSe_{0.25}Te_{0.75}$ crystal measured at T=30 K with polarization of the beam along the two high symmetry crystal axes.*

The peak A appears to have lower intensity for the Te substituted samples, suggesting a decreased number of unoccupied Se *4p* states near the Fermi level with Te substitution. In addition,

the multiple scattering hump B shows some evident changes with the Te substitution, mainly due to changing local geometry around the Se atoms. Indeed, this hump appears to be getting broader for the Te substituted samples with an overall shift towards lower energy. This should be related to local inhomogeneity of the ternary system, seen by EXAFS measurements [23, 24] To obtain further details of the unoccupied Se electronic states, we have measured the Se K-edge XANES in different polarizations on the $FeSe_{0.25}Te_{0.75}$ single crystal sample.

Figure 4.2.1.4 shows normalized Se K-edge XANES measured with the polarization parallel and nearly perpendicular to the ab-plane of the single crystal sample. There is a large polarization dependence, with the peak A due to the $1s \rightarrow 4p$ dipole transition appearing extremely damped in the spectrum obtained using perpendicular polarization. This merely brings the conclusion that unoccupied Se *4p* states near the Fermi level in these systems are mainly derived by the $p_{x,y}$ symmetry. Incidentally, the hump B also shows a strong polarization effect. Indeed, the hump has a very different spectral shape in the two geometries, appearing with apparently two broad features in the E||c geometry unlike a single broad feature in the E||ab geometry. The lower energy feature of the hump in the E||c geometry shows an overall shift with respect to the hump in the E||ab geometry. Since the hump is due to multiple scattering including Se–Fe, Se–Se and Se–Te shells, different spectral shapes are likely to be due to different contributions from these scattering paths in the two polarization geometries. The fact is that, while Se–Fe paths are equally seen in the two geometries, the Se–Se/Te paths are different with some of the scattering paths missing in the E||c geometry and hence an apparent two peak spectral shape appears in the E||c geometry unlike the broader hump B for the E||ab polarization. However, shell by shell full multiple scattering calculations need to be performed to study the details of these local geometrical variations, which are beyond the scope of the present paper's focus on the electronic structure.

4.2.2 Fe $L_{2,3}$-edge x-ray absorption spectroscopy study

Combining the experimental XAS spectra with an appropriate theoretical description, we provide valuable information on the electronic structure such as the correlation energy U, the charge transfer energy, and the electronic hybridization parameters in the $FeSe_{1-x}Te_x$ system. We find a substantial change in the hybridization between the Fe *3d* and chalcogen *p* states, which is redistributed substantially with the Te substitution. The results are consistent with weak

correlations in the chalcogenides, as in the case of Fe-pnictide superconductors [26].

We find that the Fe $L_{2,3}$ spectra of the chalcogenides are apparently similar to those observed for Fe metal without any multiplet peak structures in characteristic Fe-based materials with strong correlations such as iron oxides [178]. In addition, we have made cluster calculations of the Fe $L_{2,3}$-edge XAS. We have employed cluster-model calculations (a tetrahedral FeY_4 cluster model with Y = Se or Te) to analyze the Fe $L_{2,3}$-edge XAS [179]. In the cluster-model analysis, the wave function of the ground state is given by linear combinations of the $d^6, d^7\underline{L}, d^8\underline{L}^2, d^5C, d^6\underline{L}C$ and $d^7\underline{L}^2C$ configurations. Here, $\underline{\mathrm{L}}$ and C denote a hole in a ligand p orbital and an electron in a conduction band for the cluster model [180, 181]. The wave functions of the final states are given by linear combinations of the $cd^7, cd^8\underline{L}, cd^9\underline{L}^2, cd^6C, cd^7\underline{L}C$, and $cd^8\underline{L}^2C$ configurations, where c denotes a Fe *2p* core hole. The ligand-to-*3d* charge transfer energy is defined by $\Delta_{pd} \equiv E(d^7) - E(d^6)$ and the *3d*-*3d* Coulomb interaction energy by $U \equiv E(d^5) + E(d^7) - 2E(d^6)$, where $E(d^{n'}\underline{L}^{m'})$ is the center of gravity of the $d^{n'}\underline{L}^{m'}$ multiplet. These definitions make clear the chemical trends of the parameters. The hybridization terms between d^6 and $d^7\underline{L}$ are given by the Slater-Koster parameters (pdσ) and (pdπ) [182]. The ratio between (pdσ) and (pdπ) is fixed at -2.16. The hybridization terms for the T_2 and E symmetries are given by $T_{t2} \equiv \langle t2|H|L_{t2}\rangle = \sqrt{4/3(pd\sigma)^2 + 8/9(pd\pi)^2}$ and $T_e \equiv \langle e|H|L_e\rangle = 2\sqrt{6}/3(pd\pi)$ respectively, where L_{t2} and L_e are ligand orbitals of the T_d point group with T_2 and E symmetry, respectively[183]. In the present model, we have additional parameters: the *3d*–to–conduction band charge-transfer energy $\Delta_{dC} \equiv E(d^5C) - E(d^6)$ and the transfer integral T_{dC} between the *3d* and the conduction band orbitals. In the present calculation, Δ_{dC} and T_{dC} are fixed at 2.5 and -0.6 eV, respectively. The line spectra obtained by the cluster-model calculations are convoluted with the Doniach-Sunjic function, and the integrated backgrounds are added to be compared with the experimental results.

Figure 4.2.2.1 shows room-temperature Fe $L_{2,3}$-edge x-ray absorption spectra measured on polycrystalline samples of *FeSe*, $FeSe_{0.5}Te_{0.5}$, and *FeTe*.

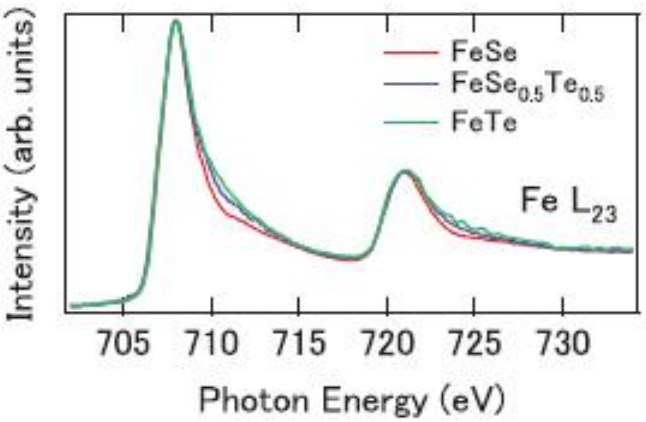

Fig. 4.2.2.1 *Fe $L_{2,3}$ x-ray absorption spectra measured on $FeSe$, $FeSe_{0.5}Te_{0.5}$, and $FeTe$ samples using TEY mode [26].*

The two white lines in the spectra result from $2p \rightarrow 3d$ dipole transitions ($2p^6 3d^6 \rightarrow 2p^5 3d^7$) with the well-separated spin-orbit-split *2*p states $2p_{1/2}(L_2)$ and $2p_{3/2}(L_3)$, appearing respectively at about 707 and 720 eV. In addition, some spectral weight can be seen in the energy range of 3–5 eV above the white lines. There is no sign of multiplet structures, making the absorption lines shapes very different from those of Fe oxides, but more similar to those of Fe metal, consistent with itinerant *3d* states albeit with higher shoulder spectral weight. Also, the Fe $L_{2,3}$ XAS of the chalcogenides appear very similar to those reported for the Fe-based pnictides [163, 184, 185, 186]. In the spectra with Te substitution, an evident effect appears in the energy range of 3–5 eV above the white lines. Indeed, the spectral weight around 710 eV increases systematically with Te substitution. This is an indication of interaction of the chalcogen atom with the Fe *3d* states. To gain further insight into the Fe $L_{2,3}$ XAS and the effect of Te substitution, we have performed cluster-model calculations.

Figure 4.2.2.2 shows a comparison of experimental and calculated spectra for *FeSe* and *FeTe*. An excellent agreement was obtained between the experimental and the calculated $L_{2,3}$ spectra with a set of parameters describing the correlation energy $U = 1.5$ eV, the charge-transfer energy $\Delta = 1\,eV$, and the *d-to-p* transfer integral $pd\sigma = -1.5$ and -1.0 eV for *FeSe* and *FeTe*, respectively. Therefore, it can be safely stated that the main effect of Te substitution is the changing interaction between the Fe *3d* and the chalcogen *p* states. It is worth recalling that a similar shoulder spectral weight is seen in the Fe $L_{2,3}$ XAS of Fe-X silicides [187], described to

be due to strong Fe *3d*-X *p* hybridization and covalent Fe-X bonds. For a further quantification of the electronic structure, a systematic analysis of the Fe $L_{2,3}$ XAS has been done by studying the effect of the correlation energy U, charge-transfer energy Δ, and transfer integral pdσ.

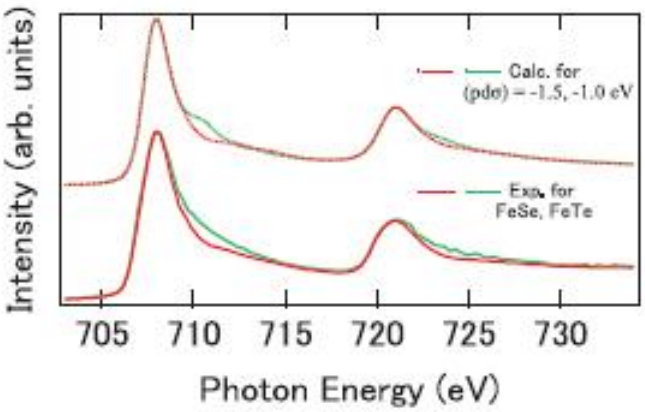

Fig. 4.2.2.2 *Experimental (solid lines) and calculated (dots) Fe $L_{2,3}$ XAS spectra of FeSe and FeTe.*

Figure 4.2.2.3 shows the calculated Fe $L_{2,3}$ XAS spectra for FeSe, showing the effect of U (top), (middle), and pdσ (bottom). From the calculated spectra we can clearly see that the effect of the correlation energy U is nothing but a modulation of the spectral weight around 5–8 eV above the white line, with the spectral weight increasing with increasing U. On the other hand, the charge transfer energy Δ seems to have hardly any effect on the Fe $L_{2,3}$ XAS.

What appears to be clear is that U and may not be relevant to describe the Te substition effect. Indeed, unlike the effect of U and Δ, the experimental data shown here (Fig. 4.2.2.1) reveal the main effect of Te substitution to be concentrated around 3 eV above the white line, i.e., to be similar to the effect of pdσ. Therefore, pdσ should be the main parameter used to describe the electronic structure of the ternary $FeSe_{1-x}Te_x$ chalcogenides. The results also appear to be consistent with the local density approximation calculations for these materials [114]. Also, the Fe-chalcogen bond length in *FeTe* is $\approx$ 2.6Å, higher than the Fe-chalcogen bond length in *FeSe* ($\approx$ 2.4Å), consistent with higher hybridization of the Fe *3d* with the chalcogen *p* states in *FeSe*.

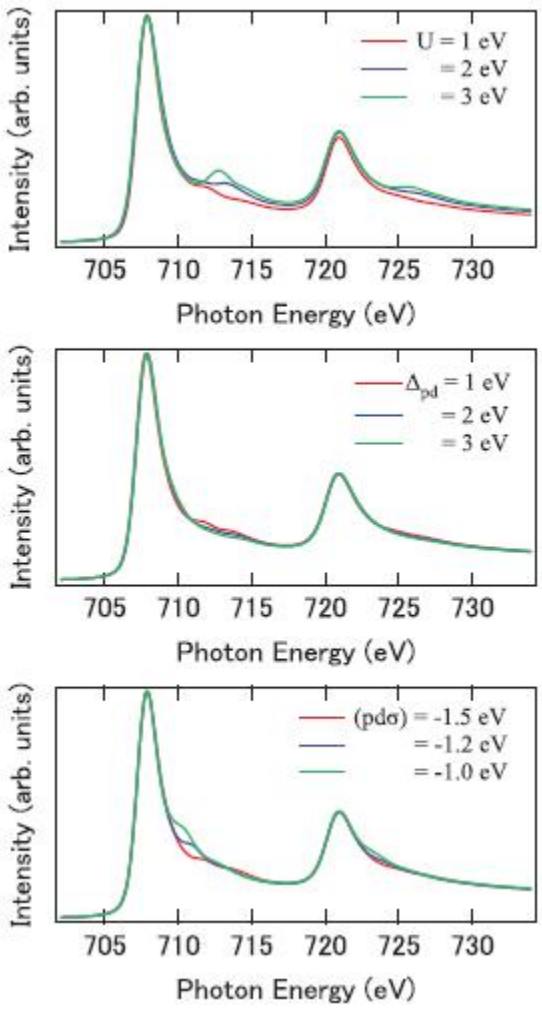

Fig. 4.2.2.3 *Fe $L_{2,3}$-edge XAS spectra obtained from cluster calculations for FeSe, showing the effect of different parameters U, Δ, and the p-d transfer.*

These results are also consistent with the higher Fe K-edge x-ray absorption near-edge spectra pre-peak intensity for *FeSe* than in *FeTe* [27] described as due to higher mixing of the chalcogen *p* orbitals with the Fe *3d* states.

4.2.3 Summary and conclusions

In this section, we have used X-ray absorption spectroscopy, a powerful high-energy site-selective probe, to investigate the electronic structure of $FeSe_{1-x}Te_x$ system. Indeed, dipole allowed direct transitions permit fingerprint of unoccupied electronic states near the Fermi level to be obtained. Combined with an appropriate theoretical description, the experimental XAS spectra can provide valuable information on the electronic structure.

We have studied the electronic structure of $FeSe_{1-x}Te_x$ chalcogenides by a combination of Fe and Se Kedge x-ray absorption near edge structure spectroscopy. From the Fe K-edge data we find a gradual and substantial decrease of the pre-peak derived by $1s \rightarrow 3d$ quadrupole transition and a dipole transition due to admixed chalcogen p states. The damping seems to be due to lower mixing of chalcogen p states in the Te containing systems, consistent with the longer Fe-Te distance. Again, the Se K-edge XANES spectra reveal a damping of unoccupied *4p* states, consistent with the Fe Kedge XANES, suggesting lower admixing of the Fe *3d* with the chalcogen p states in the Te containing systems. Furthermore, the polarized Se K-edge XANES reveals the predominant $p_{x,y}$ character of the chalcogen p states that should be involved in admixing with the unoccupied Fe *3d* states near the Fermi level. The results are consistent with strong chalcogen height sensitivity of the fundamental electronic structure, which seems to be related to the redistribution of the admixed Fe *3d* chalcogen p states and underline the importance of the *p–d* hybridization in the Fe-based chalcogenide superconductors.

Fe $L_{2,3}$-edge x-ray absorption spectroscopy combined with cluster-model calculation also have been used to study the electronic structure of $FeSe_{1-x}Te_x$ chalcogenides. The XAS spectra are quite similar to those for the metallic Fe and Fe-based pnictides, consistent with weak correlation effects in the chalcogenides. A systematic change in the experimental spectra with Te substitution is observed and well reproduced by cluster calculations. We have found that the hybridization term between the Fe *3d*–chalcogen p is the most relevant parameter to describe differences in the electronic structure of *FeSe* and *FeTe*, characterized by different superconducting and magnetic properties. In fact, a combined experimental and theoretical analysis reveals decreased hybridization of Fe *3d* and chalcogen p states with increasing Te concentration, which could be important for the superconductivity and magnetism of the chalcogenides.

Conclusion

The discovery of superconductivity at relatively high temperatures in a non-cuprate system, $REFeAsO_{1-x}F_x$ has created tremendous activity among the reseachers in this field. So far, five different structural classes of FeSCs have been found. These structures all share a common layered structure based on a planar layer of iron atoms joined by tetrahedrally coordinated pnictogen (P, As) or chalcogen (S, Se, Te) anions arranged in a stacked sequence separated by alkali, alkaline-earth or rare-earth and oxygen/fluorine 'blocking layers'. It is now widely thought that the interaction that leads to the high-Tc superconductivity originates within these common iron layers. In particular, experiemental evidences combined with theoretical calculations suggest that the height of pnictogen/chalcogen anions above and below the planar iron layer could be the switch between the superconducting and magnetic properties [11, 47, 68, 116].

This is also an important indication of the fact that local structure rather than the average crystallographic structure should be the one which requires a careful look in these materials as the case of copper oxide superconductors. In the particular case of Fe-based superconductors the knowledge of the local atomic structure should be even more important due to several Fe d-bands (interacting with the Pn/Ch anions) contributing to the Fermi level, which could be easily changed by small displacements, and hence changing the Fermi surface topology.

Indeed this has been the main theme of the present thesis.
We have presented studies on the local structure of oxypnictides and binary chalcogenide compounds exploiting X-ray absorption spectroscopy (EXAFS and XANES)[15]. The approch was taken due to the fact that X-ray absorption is a fast ($\sim 10^{-15}s$) and site selective method, providing direct information on the short/medium range order structure of materials [139]. Extended X-ray absorption fine structure (EXAFS) provides information on the local atomic distribution around a selected absorbing atom through photoelectron scattering [15]. On the other hand,

X-ray absorption near-edge structure (XANES) spectroscopy probes the distribution of the valence electrons in the final states and the local geometry around the selected atom, through multiple scattering of the photoelectron exciting from the absorbing site. The added advantage of this technique lies in the fact that, unlike photoemission experiments, there are negligible surface effects (and multiplet effects), making it a very useful finger print probe of unoccupied valence states and the local chemistry of the absorbing atom.

In this thesis, we have reported results of the studies on the local structure of oxypnictides $REFeAsO_{1-x}F_x$ (as a function of rare-earth size, doping and temperature) and 11-type chalcogenides.

REFeAsO (RE = La, Pr, Nd and Sm) system has been studied as a function of chemical pressure varied due to different rare-earth size. We have found that the Fe-As bond length and the corresponding MSRD hardly show any change, suggesting the strongly covalent nature of this bond (consistent with the theoretical prediction), while the Fe-Fe and Fe-Re bond lengths decrease with decreasing rare-earth size [16]. Moreover, the As height on the Fe-Fe plane increases with decreasing rare-earth size, and consequently also the Fe-As-Fe angle ϑ_3 decreases, revealing perfect $FeAs_4$ tetrahedron [11, 17] for the SmFeAsO. Since the vertical position of the As atom changes systematically with the rare earth size, this has a direct influence on the local geometry of the REO slabs. The interlayer disordering seems significant in the SmFeAsO system due to a higher interlayer coupling (higher vertical position of the As atoms) and a smaller misfit strain [21]. Once doped by substitution in the REO layer, the SmFeAsO with higher interlayer disorder albeit relative order within the layers shows higher T_C. The present results reveal an intimate relation between the superconductivity and the order/disorder in the spacer layers, recalling the out-of-plane disorder-controlled superconductivity already addressed in the cuprate superconductors [133]. The results appear to confirm that the interlayer coupling and oxygen order/disorder in the REO spacers have an important role in the superconductivity and itinerant magnetism of the oxypnictides [18, 19, 20].

Because superconductivity emerges when oxygen is partially substituted by fluorine, we have carried out a systematic temperature dependent local structural studies on a model oxypnictide system $NdFeAsO_{1-x}F_x$ (x = 0.0, 0.05, 0.15 and 0.18). In all the samples, the temperature dependence of the MSRDs of the Fe-As bonds is found to follow the correlated Einstein model. However, the Einstein frequency for the superconducting samples is higher than that of the

parent compound, indicating a hardening of the Fe-As bond in the former compared to the latter. The overall temperature dependence of the MSRDs of the Fe-As bond has found to be similar in NdFeAsO, SmFeAsO, LaFeAsO and $BaFe_2As_2$, but with a systematic variation of the corresponding force constants [22].

From detailed studies using EXAFS and XANES on different atomic edges, supported by multiple scattering calculations, we have concluded that different local structure of the active layers should be important for different superconducting properties with RE. Moreover, the order/disorder in the REO spacer layers, due to oxygen arrangements, is an additional parameter that we have considered to describe the functional properties in the 1111-type Fe-based systems.

Apart from the 1111-type oxypnictides, we have made a detailed study of the local structure of $FeSe_{1-x}Te_x$ systems as a function of temperature and Te content. This system represent a model system to explore possible role of atomic displacements in the correlating superconducting function in the Fe-based pnictide superconductors, due to the absence of the spacer layers.

We have investigated the local structure of $Fe(Se,S)_{1-x}Te_x$ systems, to quantify the local interatomic distances and their mean-square relative displacements as a function of temperature and chalcogen atom concentration. Different absorption edge are used to explore the local structure around different sites. We found that Fe-Se and Fe-Te distances in the ternary $FeSe_{1-x}Te_x$ are closer to the respective distances in the binary systems, revealing significant divergence of the local structure from the average one. The Se and Te atoms do not occupy the same atomic site in the $FeSe_{1-x}Te_x$, breaking the average crystal symmetry [23], as also confirmed by polarized EXAFS on single crystal [24]. The mean square relative displacements (MSRDs) show a systematic change with Te contents, consistent with bond relaxation in the inhomogeneous ternary phases. Also, the Fe-Te and Fe-S distances in the $FeS_{0.2}Te_{0.8}$ ternary system are found to be different in the crystallographically homogeneous structure. The observed features are characteristic of ternary random alloys, suggesting that a proper consideration should be given to the atomic distribution for describing complex electronic structure of these multi-band Fe-based chalcogenides [25]. We have discussed that the inhomogeneous structure of the ternaty chalcogenides have strong importance on the electronic properties of these materials. The fact that, $FeSe_{1-x}Te_x$ system manifest local structural inhomogeneity while the superconducting T_C is higher, provides further indication that the local inhomogeneity should have important role in the new Fe-based materials as well, consistent with recent experiments in favor of mesoscopic

phase separation in the Fe-based superconductors [85, 171, 173].

In order to provide valuable information on the electronic structure of $FeSe_{1-x}Te_x$ compounds, we have combined the experimental XANES spectra, that reproduce the unoccupied electronic states near the Fermi level, with an appropriate theoretical description. The XANES spectra suggest lower admixing of the Fe *3d* with the chalcogen *p* states in the Te containing systems. Furthermore, the polarized Se K-edge XANES have revealed predominant $p_{x,y}$ character of the chalcogen *p* states that should be involved in admixing with the unoccupied Fe *3d* states near the Fermi level [27]. The systematic change in the experimental spectra with Te substitution was well reproduced by cluster calculations [26]. In fact, we have found that the hybridization of Fe *3d* and chalcogen *p* states decreases with increasing Te concentration and this is the cause of the strong chalcogen height sensitivity of the fundamental properties of the Fe-based chalcogenides.

In summary, the work described in this thesis reveals important information on the local structure of Fe-based superconductors. Indeed, the local structure appears different from the crystallographic structure in the Fe-based superconductors, and in particular in the FeSe chalcogenide. While the presence of spacer layer in the Fe-based superconductors seems important to the properties of the active Fe-Arsenic block through atomic order/disorder, absence of spacer layer introduces inhomogeneities through breaking the local structural symmetry.

Although more studies are needed for clarifying quantitative role of the findings, the results reported in this thesis provide important feedback for the models describing the correlating superconductivity and magnetism in the Fe-based superconducting materials.

Appendix

In the appendix we report the preliminary results obtained by As K-edge EXAFS measurements on isoelectronic Ru-substituted $SmFe_{1-x}Ru_xAsO_{0.85}F_{0.15}$.

In the Fe-based systems the different interplaying degrees make it difficult to separate out issues. Study of such complex phase diagrams, by varying a single tuning parameter is of utmost importance to obtain experimental inputs. The $SmFe_{1-x}Ru_xAsO_{0.85}F_{0.15}$ is one of the highest T_C compounds in FeSC [202]. The layered structure of these compounds (and other related 1111 compounds), particularly the alternating active and buffer layers, is of special interest. In such systems, the interlayer coupling [18, 19], the effect of disorder induced by the changing strain effects between the layers [20, 149, 158], the localized impurity effects [203, 204], *etc* are important to understand the complex magnetic and superconducting properties. To this effect a systematic local structural study concentrating on the active layer to bring out the isovalent Ru doping induced disorder effects in the $SmFe_{1-x}Ru_xAsO_{0.85}F_{0.15}$ is of importance. Such a study can bring out correlations with the changes in the electronic density of states to the subtle structural changes. Scattering induced by substitutions is expected to affect superconductivity in a very different ways in cases of conventional or unconventional coupling [203, 204, 205]. The choice of Ru as isoelectronic substitution at Fe site of F-doped compounds allows to better clarify the role of structural disorder in modifying the normal and superconducting properties of these multiband superconductors.

Present systematic EXAFS study on the $SmFe_{1-x}Ru_xAsO_{0.85}F_{0.15}$ (x=0.0, 0.25, 0.5 and 1) is aimed at clarifying some of these issues.

High quality powder samples of $SmFe_{1-x}Ru_xAsO_{0.85}F_{0.15}$ (x=0.0, 0.25, 0.5 and 1) were used for the present study. The sample preparation and magnetic and superconducting properties are given in Ref. [203]. As K-edge EXAFS on these were carried out in transmission mode at

the beamline, BM23 of the European synchrotron radiation facility, Grenoble (France). Measurements were carried out at 60 K using a continuous flow liquid He cryostat with a temperature accuracy ±1K. A minimum of 5 scans were taken on each samples and the average of the different scans were used for the analysis. From the absorption spectra, EXAFS data were extracted following the standard procedures [15]. In case of the As K-edge EXAFS in 1111 FeSC system, the first shell contribution involves only the As-Fe bonds, and is well separated from other contributions [128, 156]. This make a single shell modelling is very effective in extracting the quantitative Fe-As bond distributions.

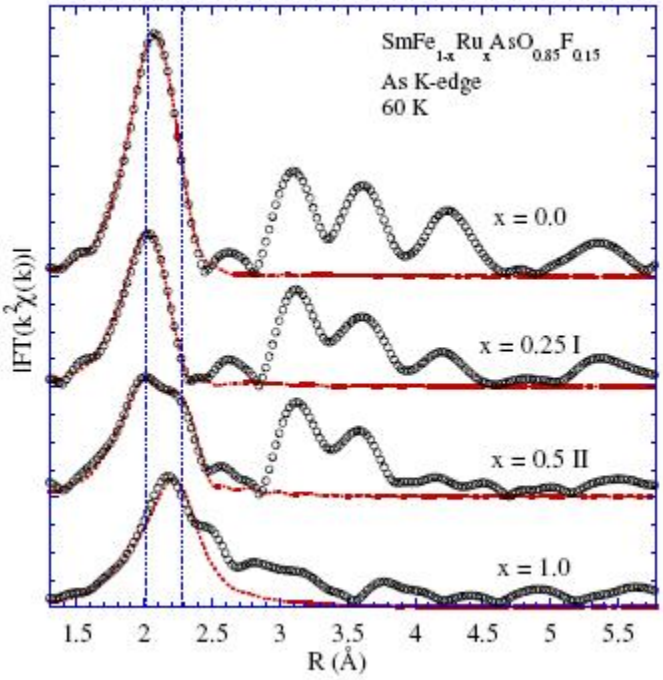

Fig. A *Fourier transform (FT) magnitudes of the As K-edge EXAFS oscillations for the* $SmFe_{1-x}Ru_xAsO_{0.85}F_{0.15}$ *(x=0.0, 0.25, 0.5 and 1) at 60 K (open circles), together with model fits (solid lines) cosidering the near neighbors of As atom. FTs are not corrected for the phase shifts, and represent raw experimental data.*

The Fourier transform (FT) magnitudes of the arsenic K-edge (k range 2.5-18 $\AA^{-1}$) EXAFS oscillations, measured on $SmFe_{1-x}Ru_xAsO_{0.85}F_{0.15}$ (x=0.0, 0.25, 0.5 and 1) at 60 K, providing partial atomic distribution around the arsenic atom are shown in Fig. A. The structure of $SmFe_{1-x}Ru_xAsO_{0.85}F_{0.15}$ has a tetragonal symmetry at room temperature. The parent

compound, SmFeAsO undergoes a structural transition from tetragonal to orthrombic phase at around 135 K. This transition is suppressed by the F-doping [202]. In $SmFe_{1-x}Ru_xAsO_{0.85}F_{0.15}$, the x=0.0 sample is having a superconducting transition temperature 50 K [203]. With Ru doping the superconducting transition temperature dropes, the detailed changes are reported in ref . For the As site (probed by the As K-edge), there are four Fe(Ru) near neighbours at a distance $2.4\mathring{A}$ (main peak at $2\mathring{A}$ in Fig. A). The next nearest neighbours of As are Sm and O atoms (4 Sm atoms at a distance ∼3.3 Å and 4 O atoms at a distance ∼3.6 Å). Contributions of these distant shells appear mixed, giving a multiple structured peak at $2.6 - 4.0\,\mathring{A}$. However, the contribution of the Fe- As/Ru-As bonds are well separated from other contributions and can be analysed using a single shell fit to extract the quantiative information on bond correlations. From the first look one can see local structural differences with variable Ru content. The amplitude of Fourier transform appears to decrease with increasing the Ru-substituted content. As a possible explanation, Ru could introduce a large disorder in the Fe-As layers, that affects the superconducting state [18, 19]. These preliminary results have to be confirmed by an appropriate analysis.

Bibliography

[1] Kamihara Y et al, *J. Am. Chem. Soc.* 130, 3296 (2008).

[2] Bednorz J G and Muller K A, *Z. Phys. B* 64, 189 (1986).

[3] Hebard A F et al, *Nature* 350, 600 (1991).

[4] Nagamatsu J et al, *Nature* 410, 63 (2001).

[5] Lee P A et al, *Rev. Mod. Phys.* 78, 17 (2006).

[6] Paglione J and Greene R L, *Nature Physics* 6, 645 (2010).

[7] Mazin I I and Schmalian J, *Physica C* 469, 614 (2009).

[8] Lumsden M D and Christianson A D, *J. Phys.: Condens. Matter* 22, 203203 (2010).

[9] Singh D J and Du M H, *Phys. Rev. Lett.* 100, 237003 (2008).

[10] Singh D J, *Physica C* 469, 418 (2009).

[11] Lee C-H et al, *J. Phys. Soc. Jpn.* 77, 083704 (2008).

[12] Bianconi A et al, *Phys. Rev. Lett.* 76, 3412 (1996); Saini N L et al, *Phys. Rev. B* 55, 12759 (1997); Saini N L et al, *J. Phys. Soc. Jpn.* 70, 2092 (2001); Saini N L et al, *Phys. Rev. B* 64, 132510 (2001); Oyanagi H et al, *Phys. Rev. B* 75, 024511 (2007).

[13] Ren Z-A et al, *Europhys. Lett.* 82, 57002 (2008) .

[14] Moon C-Y and Choi H J, *Phys. Rev. Lett.* 104, 057003 (2010).

[15] Prinz R. and Koningsberger D. (Editors), *X-ray Absorption: Principles, Applications, Techniques of EXAFS, SEXAFS, XANES* (Wiley, New York) 1988.

[16] Iadecola A et al, *Europhys. Lett.* 87, 26005 (2009).

[17] Zhao J et al, *Nature Mater.* 7, 953 (2008).

[18] Joseph et al, *J. Phys.: Condens. Matter* 21, 432201 (2009).

[19] Xu W et al, *J. Phys.: Condens. Matter* 22, 125701 (2010).

[20] Xu W et al, *Europhys. Lett.* 90, 57001 (2010).

[21] Fratini M et al, *Supercond. Sci. Technol.* 21, 092002 (2008).

[22] Joseph B et al, *J. Phys.: Condens. Matter* 23, 265701 (2011).

[23] Joseph B et al, *Phys. Rev. B* 82, 020502(R) (2010).

[24] Iadecola et al, *Europhys. Lett.* 90, 67008 (2010).

[25] Iadecola A et al, *J. Phys.: Condens. Matter* 23, 425701 (2011).

[26] Saini N L et al, *Phys. Rev. B* 83, 052502 (2011).

[27] Joseph B et al, *J. Phys.: Condens. Matter* 22, 485702 (2010).

[28] Kamihara Y et al, *J. Am. Chem. Soc.* 128, 10012 (2006).

[29] Shimizu K et al, *Nature* 412, 316–318 (2001).

[30] Stewart G R, *arXiv:*1106.1618.

[31] Wang C et al, *Europhys. Lett.* 83, 67006 (2008).

[32] Wu G et al, *J. Phys.: Condensed Matter* 21, 142203 (2009).

[33] Cheng P et al, *Europhys. Lett.* 85, 67003 (2009).

[34] Chu C W et al, *Science* 235, 567 (1987).

[35] Wu M K et al, *Phys. Rev. Lett.* 58, 908 (1987).

[36] Takahashi H et al, *Nature* 453, 376 (2008).

[37] Chen X H et al, *Nature* 453, 761 (2008).

[38] Ren Z-A et al, *Europhys. Lett.* 83, 17002 (2008).

[39] Rotter M et al, *Phys. Rev. Lett.* 101, 107006 (2008).

[40] Wang X C et al, *Solide State Commun.* 148, 538 (2008).

[41] Hsu F-C et al, *Proc. Natl. Acad. Sci.*(USA) 105,14262 (2008).

[42] Ogino H et al, *Supercond. Sci. Technol.* 22, 075008 (2009).

[43] Zhu X et al, *Phys. Rev. B* 79, 220512(R) (2009).

[44] Margadonna S et al, *Phys. Rev. B* 80, 064506 (2009).

[45] Yeh K-W et al, *Europhys. Lett.* 84, 37002 (2008).

[46] Sanna S et al, *Phys. Rev. B* 80, 052503 (2009); Sanna S et al, *Phys. Rev. B* 82, 060508 (2010).

[47] Cano A, *Phys. Rev. B* 82, 020408(R) (2010).

[48] Onari S et al, *Phys. Rev. B* 81, 060504(R) (2010).

[49] Yang W–L et al, *Phys. Rev. B* 80, 014508 (2009).

[50] Wang K et al, *Phys. Rev. B* 83, 174503 (2011).

[51] Pourret A et al, *Phys. Rev. B* 83, 020504(R) (2011).

[52] Sefat A S et al, *arXiv:*1009.4911.

[53] McQueen T M et al., *Phys. Rev. B* 79, 014522 (2009); McQueen T M et al, *Phys. Rev. Lett.* 103, 057002 (2009).

[54] Kitagawa K et al, *J. Phys. Soc. Jpn.* 77, 114709 (2008).

[55] Lynn W L and Dai P, *Physica C* 469, 469 (2009).

[56] de la Cruz C et al, *Nature* 453, 899 (2008).

[57] Rotter M et al, *Phys. Rev. B* 78, 020503 (2008).

[58] Jesche A et al, *Phys. Rev. B* 78, 180504 (2008).

[59] Ni N et al, *Phys. Rev. B* 78, 014523 (2008).

[60] Tegel M et al, *J. Phys.: Condens. Matter* 20 452201 (2008).

[61] Bao W et al., *Phys. Rev. Lett.* 102, 247001 (2009).

[62] Li S L et al., *Phys. Rev. B* 79, 054503 (2009).

[63] Fang M H et al. , *Phys. Rev. B* 78, 224503 (2008).

[64] Kimber S A J et al, *Nature Mater.* 8, 471 (2009).

[65] Mikuda H et al, *J. Phys. Soc. Jpn.* 77, 093704 (2008).

[66] Mikuda H et al, *Physica C* 469, 559 (2009).

[67] Horigane K et al, *J. Phys. Soc. Jpn.* 78, 074718 (2009).

[68] Mizuguchi Y et al, *Supercond. Sci. Technol.* 23, 054013 (2010).

[69] Okabe H et al, *Phys. Rev. B* 81, 205119 (2010).

[70] Tegel M et al, *Solid State Commun.* 150, 383 (2010).

[71] Stewart G R, *Rev. Mod. Phys.* 73, 797 (2001).

[72] Stewart G R, *Rev. Mod. Phys.* 78, 743 (2006).

[73] Yang W–L et al, *Phys. Rev. B* 80, 014508 (2009).

[74] McGuire M A et al, *Phys. Rev. B* 78, 094517 (2008).

[75] Rotter M et al, *Phys. Rev. Lett.* 101, 107006 (2008).

[76] Saha S R et al, *Phys. Rev. Lett.* 103, 037005 (2009).

[77] Wang X F et al, *Phys. Rev. Lett.* 102, 117005 (2009).

[78] Chen G F et al, *Phys. Rev. B* 78, 224512 (2008).

[79] Ronning F et al, *J. Phys.:Condens. Matter* 20, 322201 (2008).

[80] Wu D et al, *Phys. Rev. B* 79, 155103 (2009).

[81] Mizuguchi Y et al, *J. Phys. Soc. Jpn.* 78, 074712 (2009); Mizuguchi Y et Takano Y, *J. Phys. Soc. Jpn.* 79, 102001 (2010).

[82] Braithwaite D et al, *J. Phys.: Condens. Matter* 21, 232202 (2009).

[83] Masaki S et al, *J. Phys. Soc. Jpn.* 78, 063704 (2009).

[84] Iikubo S et al, *J. Phys. Soc. Jpn.* 78, 103704 (2009).

[85] Hu R et al, *Phys. Rev. B* 80, 214514 (2009).

[86] Sales B C et al, *Phys. Rev. B* 79, 094521 (2009).

[87] Klingeler R et al, *Phys. Rev. B* 81, 024506 (2010).

[88] Wang X F et al, *Phys. Rev. Lett.* 102, 117005 (2009).

[89] Qureshi N et al, *Phys. Rev. B* 82, 184521 (2010).

[90] Zhang G M et al, *Europhys. Lett.* 86, 37006 (2009).

[91] Dong J et al, *Europhys. Lett.* 83, 27006 (2008).

[92] Mazin I I et al, *Phys. Rev. Lett.* 101, 057003 (2008).

[93] Yildirim T, *Phys. Rev. Lett.* 101 057010 (2008).

[94] Ma F J et al, *Phys. Rev. B* 79, 224517 (2009).

[95] Si Q M and Abrahams E, *Phys. Rev. Lett.* 101 076401 (2008).

[96] Lee C-C et al, *Phys. Rev. Lett.* 103 267001 (2009).

[97] Huang Q et al, *Phys. Rev. Lett.* 101, 257003 (2008).

[98] Zhao J et al, *Phys. Rev. B* 78, 140504 (2008).

[99] Goldman A I et al, *Phys. Rev. B* 78, 100506 (2008).

[100] Su Y et al, *Phys. Rev. B* 79, 064504 (2009).

[101] Li H F et al, *Phys. Rev. B* 80, 054407 (2009).

[102] Laplace Y et al, *Phys. Rev. B* 80, 140501 (2009).

[103] Bonville P et al, *arXiv:*1002.0931.

[104] Wen J et al, *Phys. Rev. B* 80, 104506 (2009).

[105] Subedi A et al, *Phys. Rev. B* 78, 134514 (2008).

[106] Zhang L J et al, *Phys. Rev. B* 79 012506 (2009).

[107] Zhang C et al, *Phys. Rev. B* 80, 144519 (2009).

[108] Xia Y et al, *Phys. Rev. Lett.* 103, 037002 (2009).

[109] Ma F J et al, *Phys. Rev. Lett.* 102, 177003 (2009).

[110] Fang C et al, *Europhys. Lett.* 86, 67005 (2009).

[111] Mazin I I and Johannes M D, *Nature Phys.* 5, 141 (2009).

[112] Lebegue S, *Phys. Rev. B* 75, 035110 (2007).

[113] Koitzsch A et al, *Phys. Rev. B* 78, 180506 (2008).

[114] Miyake T et al, *J. Phys. Soc. Jpn.* 79, 044705 (2010).

[115] Vildosola V et al, *Phys. Rev. B* 78, 064518 (2008).

[116] Kuroki K et al, *Phys. Rev. B* 79, 224511 (2009).

[117] Boeri L et al, *Phys. Rev. Lett.* 101, 0246403 (2008).

[118] Cvetkovic V et al, *Europhys. Lett.* 85, 37002 (2009).

[119] Hanaguri T et al, *Science* 323, 923 (2009).

[120] Hanaguri T et al, *Science* 328, 474 (2010).

[121] See e.g., Fukuyama H et al (Editors), Proceedings of the International Symposium on Fe-Pnictide Superconductors, in *J. Phys. Soc. Jpn. Suppl. C*, Vol. 77 (2008).

[122] See, e.g., the focus issue on iron based superconductors Hosono H et al, *New J. Phys.* 11, 025003 (2009) .

[123] See, e.g., a short review by Izyumov Yu A and Kurmaev E Z, *Phys. Usp.* 51, 1261 (2008) .

[124] Huang Q et al, *Phys. Rev. B* 78, 054529 (2008).

[125] See, e.g., a review by Bianconi A and Saini N L, *Struct. Bond.* 114, 287 (2005).

[126] Gurman S J, *J. Synchrotron Radiat.* 2, 56 (1995).

[127] Ozawa Tadashi C. and Kauzlarich Susan M., *Sci. Technol. Adv. Mater.* 9, 033003 (2008) .

[128] Tyson T A et al, *J. Appl. Phys.* 108, 123715 (2010).

[129] McMillan W L et al, *Phys. Rev.* 167, 331 (1968) ; Allen P B and Dynes R C, *Phys. Rev. B* 12, 905 (1975).

[130] Santi G, Dugdale S B and Jarlborg T, *Phys. Rev. Lett.* 87, 247004 (2001).

[131] Journel L et al, *Phys. Rev. B* 66, 045106 (2002) and references therein.

[132] Bianconi A et al, *Phys. Rev. B* 35, 806 (1987); Chaboy J et al, *J. Magn. Magn. Mater.* 166, 149 (1997).

[133] Eisaki H et al, *Phys. Rev. B* 69, 064512 (2004).

[134] Bianconi A et al, *Phys. Rev. B* 32, 4292 (1985); Bianconi A, Dell'Ariccia M, Gargano A and Natoli C R, *EXAFS and Near Edge Structure*, (ed . Springer) (1987).

[135] Ignatov A et al, *arXiv:*0808.2134.

[136] Tan Z et al, *Phys. Rev. Lett.* 64, 2715 (1990); Tan Z et al, *Phys. Rev. B* 42 4808 (1990); Tan Z et al, *Phys. Rev. B* 44, 7008 (1991).

[137] Wu Z Y et al, *Phys. Rev. B* 45, 531 (1992); Wu Z Y et al, *Phys. Rev. B* 57, 10336 (1998).

[138] Mustre de Leon J et al, *J. Supercond. Nov. Mag.* 22, 579–83 (2009).

[139] Bianconi A et al, *J. Phys.: Condens. Matter* 12, 10655 (200); Bianconi A et al, *J. Alloys Compounds* 317, 537 (2001); Agrestini S et al, *J. Phys. A: Math. Gen.* 36, 9133 (2003).

[140] Ankudinov A L et al, *Phys. Rev. B* 58, 7565 (1998).

[141] Ankudinov A L et al, *Phys. Rev. B* 67, 115120 (2003); Moreno M S et al, *Micron* 38, 1 (2007).

[142] Hedin L and Lundqvist S, *Solid State Physics* vol 23 (1970), ed. D T Frederick Seiz and E Henry (New York: Academic).

[143] Soldatov A V et al, *Phys. Rev. B* 50, 5074 (1994).

[144] Acosta-Alejandro M et al, *Phys. Rev. B* 77, 085107 (2008).

[145] Di Cicco A and Sperandini F, *Physica C* 258, 349 (1996).

[146] Chaboy J et al, *Phys. Rev. B* 49, 11652 (1994); Chaboy J et al, *Japan. J. Appl. Phys.* 32, 61 (1993); Chaboy J et al, *Chem. Phys. Lett.* 174, 389 (1990).

[147] Rodgers J A et al, *Phys. Rev. B* 80, 052508 (2009).

[148] Billinge S J L and Duxbury P M, *Phys. Rev. B* 66, 064529 (2002).

[149] Ricci A et al, *J. Supercond. Nov. Magn.* 22, 589 (2009).

[150] Iadecola et al, unpublished.

[151] Malavasi L et al, *J. Am. Chem. Soc.* 132, 2417 (2010).

[152] Di Gioacchino D et al, *J. Supercond. Nov. Mag.* 22, 549 (2009).

[153] Ressler T, *J. Synchrotron Radiat.* 5, 118 (1998).

[154] Mustre de Leon J et al, *Phys. Rev. B* 44, 4146 (1991).

[155] Calamiotou M et al, *Europhys. Lett.* 91, 57005 (2010).

[156] Zhang C J et al, *Phys. Rev. B* 81, 094516 (2010).

[157] Cheng J et al, *J. Synchrotron Radiat.* 17, 730 (2010).

[158] Ricci A et al, *Phys. Rev. B* 82, 144507 (2010).

[159] Tian W et al, *Phys. Rev. B* 82, 060514 (2010).

[160] Akrap A et al, *Phys. Rev. B* 80, 180502(R) (2009).

[161] Zhang L et al, *Phys. Rev. B* 79, 052507 (2009).

[162] Gallais Y et al, *Phys. Rev. B* 78, 132509 (2008).

[163] Bondino F et al, *Phys. Rev. B* 82, 014529 (2010).

[164] Dong T et al, *Phys. Rev. B* 82, 054522 (2010); Marini C et al, *Europhys. Lett.* 84 67013 (2008).

[165] Joseph B et al, *J. Phys.: Condens. Matter* 23, 112202 (2011).

[166] Nishi I et al, *arXiv:*1102.4907v1.

[167] Sun L et al, *arXiv:*0907.4212v1.

[168] Onuki Y and Kitaoka Y (ed), *J. Phys. Soc. Jpn.* 76, 051001 (2007) special issue of Frontiers of Novel Superconductivity in Heavy Fermion Compounds; see also, a brief review by Steglich F, *J. Phys. Soc. Jpn.* 74, 167 (2005); Steglich F, *J. Phys. Soc. Jpn.* 74, 222 (2005).

[169] Pomjakushina E et al, *Phys. Rev. B* 80, 024517 (2009).

[170] Medvedev S et al., *Nature Mater.* 8, 630 (2009).

[171] Khasanov R et al., *Phys. Rev. B* 80, 140511 (2009).

[172] Xia Y et al, *Phys. Rev. Lett.* 103, 037002 (2009).

[173] Mertelj T et al, *Phys. Rev. Lett.* 102, 117002 (2009).

[174] Lehman M C et al, *arXiv:*0909.0480v1.

[175] Chang B C et al, *Phys. Rev. B* 80, 165108 (2009).

[176] Louca D et al, *Phys. Rev. B* 81, 134524 (2010).

[177] Chen C L et al, *Europhys. Lett.* 93, 47003 (2011).

[178] Regan T J et al, *Phys. Rev. B* 64, 214422 (2001).

[179] Fujimori A and Minami F, *Phys. Rev. B* 30, 957 (1984).

[180] Bocquet A E et al, *Phys. Rev. B* 46, 3771 (1992).

[181] Bocquet A E et al, *Phys. Rev. B* 52, 13838 (1995).

[182] Harrison W A et al, *Electronic Structure and the Properties of Solids* (Dover, New York, 1989).

[183] Mizokawa T and Fujimori A, *Phys. Rev. B* 48, 14150 (1993).

[184] Yang W L et al, *Phys. Rev. B* 80, 014508 (2009).

[185] Parks Cheney C et al, *Phys. Rev. B* 81, 104518 (2010).

[186] Bondino F et al, *Phys. Rev. Lett.* 101, 267001 (2008).

[187] Sirotti F et al, *Phys. Rev. B* 48, 8299 (1993).

[188] see, e.g. P.A.ODay, N. Rivera Jr., R. Root and S. A. Carroll, *American Mineralogist* 89, 572 (2004).

[189] Zajdel P et al, *J. Am. Chem. Soc.* 132, 13000 (2010).

[190] see, e.g. *Ternary and multinary compounds*, edited by S.K. Deb and A. Zunger (Materials Research Society, Pittsburg, 1987).

[191] Sevillano E et al, *Phys. Rev. B* 20, 4908 (1979).

[192] see, e.g. a review by J. J. Rehr and R. C. Albers, *Rev. Mod. Phys.* 72, 621 (2000).

[193] Mikkelsen J C Jr and Boyce J B, *Phys. Rev. Lett.* 49, 1412 (1982).

[194] Balzarotti A et al, *Phys. Rev. B* 30, 2295 (1984).

[195] Islam Q T and Bunker B A, *Phys. Rev. Lett.* 59, 2701 (1987).

[196] Happo N et al, *J. Phys.: Condens. Matter* 8 4315 (1996).

[197] Peterson P F et al, *Phys. Rev. B* 63, 165211 (2001).

[198] Martins J L and Zunger A, *Phys. Rev. B* 30, 6217 (1984).

[199] Zunger A, Appl. *Phys. Rev. Lett.* 50, 164 (1987).

[200] Srivastava G P et al, *Phys. Rev. B* 31, 2561 (1985).

[201] Duan H et al, *Phys. Rev. B* 76, 035209 (2007).

[202] Johnston D C, *Adv. Phys.* 59, 803–1061 (2010).

[203] Tropeano M et al, *Phys. Rev. B* 81, 184504 (2010).

[204] Kitagawa S et al, *Phys. Rev. B* 83, 180501 (2011).

[205] Onari S and Kontani H, *Phys. Rev. Lett.* 103, 177001 (2009).